

1
2
3
4
5
6
7
8
9
10
11
12
13
14
15
16
17
18
19
20
21
22
23
24
25
26
27
28
29
30
31
32
33
34
35
36
37
38
39
40
41
42
43
44
45
46
47
48
49

Mapping of the podocin proximity-dependent proteome reveals novel components of the kidney podocyte foot process

Gary F. Gerlach, Zachary H. Imseis, Shamus L. Cooper, Anabella N. Santos, and Lori L. O'Brien

Affiliations:

Department of Cell Biology and Physiology, University of North Carolina at Chapel Hill, Chapel Hill, NC 27599

Corresponding author:

Lori L. O'Brien

lori_obrien@med.unc.edu

50 **Abstract**

51 The unique architecture of glomerular podocytes is integral to kidney filtration. Interdigitating
52 foot processes extend from the podocyte cell body, wrap around fenestrated capillaries, and form
53 specialized junctional complexes termed slit diaphragms to create a molecular sieve. However, the
54 full complement of proteins which maintain foot process integrity, and how this localized proteome
55 changes with disease, remains to be elucidated. Proximity-dependent biotin identification (BioID)
56 enables the identification of spatially localized proteomes. To this end, we developed a novel *in*
57 *vivo* BioID knock-in mouse model. We utilized the slit diaphragm protein podocin (*Nphs2*) to create
58 a podocin-BioID fusion. Podocin-BioID localizes to the slit diaphragm and biotin injection leads to
59 podocyte-specific protein biotinylation. We isolated the biotinylated proteins and performed mass
60 spectrometry to identify proximal interactors. Gene ontology analysis of 54 proteins specifically
61 enriched in our podocin-BioID sample revealed ‘cell junctions’, ‘actin binding’, and ‘cytoskeleton
62 organization’ as top terms. Known foot process components were identified and we further
63 uncovered two novel proteins: the tricellular junctional protein *Ildr2* and the CDC42 and N-WASP
64 interactor *Fnbp1l*. We confirmed *Ildr2* and *Fnbp1l* are expressed by podocytes and partially
65 colocalize with podocin. Finally, we investigated how this proteome changes with age and
66 uncovered a significant increase in *Ildr2*. This was confirmed by immunofluorescence on human
67 kidney samples and suggests altered junctional composition may preserve podocyte integrity.
68 Together, these assays have led to new insights into podocyte biology and supports the efficacy of
69 utilizing BioID *in vivo* to interrogate spatially localized proteomes in health, aging, and disease.

70
71
72
73
74
75
76
77
78
79
80
81
82
83
84
85
86
87
88
89
90
91
92
93
94
95
96
97
98

99 Introduction

100 Kidneys perform vital functions as they filter waste and toxins from the blood and regulate
101 body fluid homeostasis. The simplest functional unit of the kidney is the nephron, composed of a
102 blood filter termed the glomerulus connected to a segmented tubule. The glomerulus operates as a
103 ‘molecular sieve’, filtering blood and inhibiting passage of large macromolecules and red blood
104 cells into the nephron tubule. The glomerulus relies on specialized epithelial cells called podocytes,
105 named for their unique cellular morphology with long extruding projections, termed foot processes.
106 Podocyte foot processes wrap around a tuft of fenestrated endothelial capillaries leaving small
107 gaps, or slits, between them. Podocytes undergo morphological changes to their junctional
108 architecture during development to form a specialized barrier between foot processes termed a slit
109 diaphragm.^{1–3} The slit diaphragm executes multiple functions including macromolecular filtering in
110 collaboration with the underlying glomerular basement membrane, connection to the actin
111 cytoskeleton to maintain foot process architecture, and signaling that regulates podocyte integrity.
112 The slit diaphragm is distinct from other junctional complexes as it integrates unique structural
113 components as well as components of adherens and tight junctions ^{4–8}. Nearly 50 years ago, a
114 zipper-like model for the slit diaphragm was proposed, wherein proteins from neighboring foot
115 processes partially cross the intervening intercellular space and overlap, forming the dense
116 protein-rich slit diaphragm structure eloquently visualized by electron microscopy (EM).^{9,10} More
117 recent block-face scanning electron microscopy has revealed a ‘ridge-like prominence’ architecture
118 to podocyte foot processes, formed on the basal surface of the primary foot process.^{2,11} These
119 investigations underscore the continued advancement in our understanding of podocyte structure
120 and function.

121 When podocytes undergo stress or injury above a threshold, they initiate a response that
122 leads to foot process effacement, loss of slit diaphragms, and proteinuria. Loss of podocyte
123 integrity, observed as effacement, is associated with proteinuric kidney disease^{12–14}. This
124 pathology has been described in both acquired and hereditary forms of glomerular disorders or
125 podocytopathies.¹⁵ Podocytopathies are a class of kidney diseases in which direct or indirect
126 podocyte injury drives proteinuria or nephrotic syndrome and can ultimately lead to end-stage renal
127 disease (ESRD). Genetic studies have previously identified mutations in numerous podocyte foot
128 process components such as Membrane associated guanylate kinase WW and PDZ Domain
129 Containing 2 (MAGI2)¹⁶, CD2-associated protein (CD2AP)^{17,18}, nephrin (NPHS1)^{6,19}, and podocin
130 (NPHS2)^{7,20} as causal for nephrotic disease. Additionally, diseases such as diabetes and
131 autoimmune disorders can lead to podocyte injury²¹. While the downstream result is effacement
132 and loss of slit diaphragms, we know little about the temporal changes occurring specifically within
133 the foot process and locally at the slit diaphragm.

134 The identification of slit diaphragm protein complexes with immunoprecipitation followed by
135 mass spectrometry (MS) has uncovered important localized interactions^{22,23}. However, the
136 efficiency of these immunoprecipitations is often hindered by harsh conditions required to extract
137 membrane proteins, which can eliminate weaker binding interactions, or by antibodies that may
138 disrupt interactions. Additionally, transient interactions may be missed in such experiments.
139 Podocin is known to localize to the slit diaphragm and interacts with both nephrin, Neph1, and
140 Cd2ap.^{24–27} Podocin is a member of the stomatin family, containing a central hinge region that
141 integrates into the membrane of the foot process with cytoplasmic N and C termini.²⁸ Previous
142 studies demonstrated podocin’s role in the development of the multiprotein-lipid super complex of
143 the slit diaphragm.²⁷ Podocin’s ability to oligomerize and act as a protein scaffold at slit diaphragms
144 ideally positions it for use as a bait protein in proteomic studies.

145 The discovery and engineering of a promiscuous prokaryotic biotin ligase by Roux and
146 colleagues and concomitant blossoming of –omics technologies in the last decade have laid the
147 groundwork to uncover spatially localized proteomes.^{29,30} Proximity-dependent biotin identification,

148 or BioID, utilizes a mutated prokaryotic biotin ligase fused to a bait protein of interest to covalently
149 attach biotin to proteins within the vicinity of a bait protein. The radius of biotinylation can range
150 from ~10nm to 25nm, dependent on the size of the linker between the bait and the biotin ligase,
151 allowing for the biotinylation of both direct and indirect interactors.^{29,30} The BioID system requires
152 exogenous addition of biotin for the ligase to covalently biotinylate a proximally located protein,
153 giving the BioID system spatiotemporal control of protein tagging. Additionally, the biotin labels are
154 stable and can withstand harsh isolation conditions, allowing the capture of transient interactors
155 and membrane proteins, respectively. The BioID system has provided plentiful *in vitro* reports from
156 cell culture models that highlight the power of the system and its ability to discover novel
157 components of even well-documented cellular machinery such as the centrosome and cilium.^{31,32}
158 There have been limited *in vivo* reports of BioID, but it has been used successfully in vertebrates
159 such as zebrafish and mice to identify endogenous interactomes.³²⁻³⁴ To the best of our
160 knowledge, this approach has not been employed in the mammalian kidney.

161 Here, we utilized gene editing to introduce a smaller, more efficient promiscuous biotin
162 ligase (BioID2) into the endogenous murine *Nphs2* locus to create a fusion protein, hereafter
163 referred to as podocin-BioID (*Nphs2^{BioID2}*). Our podocin-BioID model offers the capacity to uncover
164 proteins that localize to the region of the podocyte foot process within the vicinity of podocin in an
165 *in vivo* mammalian system. We were able to identify novel podocyte foot process proteins and
166 furthermore how this proteome changes with age, highlighting the utility of our model for
167 uncovering new interactors as well as disease-associated changes.

168

169 Results

170

171 Generation of the *Nphs2^{BioID2}* knock-in mouse model

172 To generate our mouse model, we utilized CRISPR/Cas9 gene editing in combination with
173 homology-directed repair to knock-in the HA-tagged, mutated *A. aeolicus* biotin ligase (BioID2) in
174 frame at the *Nphs2* locus³⁰. A single guide RNA (sgRNA) was used to target the stop codon within
175 the eighth exon of *Nphs2* to create the fusion. A 13x Glycine/Serine(G/S) flexible linker region was
176 included between *Nphs2* and the ligase to provide up to a 25nm reach (Figure 1A)³⁰. C57BL/6J
177 zygotes were injected and after screening the resulting animals for a single knock-in with the
178 correct sequence, several founders were identified. A single male founder was utilized for
179 subsequent breeding and expansion of the *Nphs2^{BioID2}* line. Genotyping E18.5-P0 pups from
180 incrosses of *Nphs2^{BioID2/+}* animals identified wildtype, heterozygous, and homozygous offspring at
181 approximately anticipated Mendelian ratios of 29%, 52%, and 19%, respectively (n=73, Figure
182 1B,C). However, we were typically unable to recover homozygous *Nphs2^{BioID2/BioID2}* pups after 1-
183 week of birth. Overall, the gross morphology of homozygous pups and kidneys appeared normal at
184 P0 and we were unable to determine the specific cause of their death. Due to the early
185 homozygous death, all subsequent experiments for proteomic profiling were performed on
186 heterozygous *Nphs2^{BioID2/+}* animals. To test the function of the podocin-ID fusion and determine if
187 the ligase was able to biotinylate podocyte proteins, we administered 5 mg/kg biotin for 7
188 consecutive days to 8-10 week old *Nphs2^{BioID2/+}* and wild type control mice, a dosage utilized in
189 previous protocols for *in vivo* BioID experiments.³⁴ Following 1 week of subcutaneous biotin
190 injections, kidneys harvested from *Nphs2^{BioID2/+}* mice displayed a pronounced streptavidin signal
191 within glomeruli and specifically podocytes marked by Wt1-positive nuclei (Figure 1D). We
192 occasionally detected streptavidin-positive signal within the tubules which either represents
193 background staining or uptake of free biotin, as controls also displayed this non-glomerular signal
194 pattern. Finally, probing for the HA tag contained within the podocin-BioID fusion shows that the
195 HA signal overlaps with the streptavidin signal, confirming the fusion protein is being specifically
196 translated in podocytes and that the biotin ligase is functional (Figure 1D).

197 **Podocin-BioID kidneys display normal nephron morphology and the fusion localizes to the** 198 **slit diaphragm**

199 We further wanted to confirm that the kidneys of animals expressing the podocin-BioID
200 fusion did not display any significant phenotypic differences, most specifically to the nephron. If the
201 fusion protein was not localizing or functioning properly, the animals may display phenotypes
202 associated with *Nphs2* knockout animals such as enlarged glomeruli, vacuolated podocytes, and
203 mesangial expansion.³⁵ Additionally, dilated tubules may indicate abnormal nephron function.
204 Immunostaining kidney sections of wild type, heterozygous, and homozygous animals at E18.5
205 revealed no qualitative differences in glomerular size or proximal tubule dilation (Figure 2A). This
206 further supports that mislocalization or abnormal function of podocin-ID in podocytes is not the
207 likely cause of death in the homozygous animals. Immunofluorescence staining showed a
208 significant overlap between the HA signal and signal from a podocin-specific antibody, supporting
209 that the fusion protein is localizing properly in heterozygous animals and that it is being expressed
210 at similar levels in the homozygous animals (Figure 2A). Importantly, we did not observe the HA
211 antibody signal anywhere else besides the glomerulus.

212 Additionally, we wanted to confirm that the podocin-BioID protein was localizing to the slit
213 diaphragm where podocin is known to interact with other slit diaphragm proteins and play a
214 functional role.^{24–27,35} We utilized immunogold labeling in combination with transmission electron
215 microscopy (TEM) to examine the subcellular localization of the podocin-BioID protein (Figure 2B,
216 B'). *Nphs2^{BioID2/+}* kidney sections were stained with an anti-HA antibody followed by a colloidal gold-
217 AffiniPure secondary. Punctate gold signals were observed near electron dense regions between
218 foot processes, the location of the slit diaphragm (Figure 2B, B' arrowheads). We observed
219 minimal gold signal outside of this region. To confirm that this is the site of normal podocin
220 localization in our control animals, wildtype littermates were probed with a podocin antibody and
221 also showed localization of punctate gold signal near the electron dense region of the slit
222 diaphragm (Figure 2 C, arrowheads).

223 **An enrichment of biotinylated proteins is detected in lysates from *Nphs2^{BioID2/+}* kidneys**

224 To enrich our podocin-BioID protein lysates for glomeruli, we surgically isolated the cortex
225 from each kidney of *Nphs2^{BioID2/+}* animals and wildtype controls at 8-10 weeks. Isolated cortex was
226 homogenized and lysed to obtain protein lysates from each animal. Protein lysates were applied to
227 magnetic streptavidin coated beads to isolate the biotinylated proteins and an aliquot was removed
228 and tested to validate the efficacy of the biotin ligase. By Western blot analysis, we identified an
229 increase in the number of biotinylated proteins in our *Nphs2^{BioID2/+}* sample versus wildtype along
230 the full spectrum of molecular weights (Figure 3A). In contrast, few streptavidin labeled,
231 biotinylated, proteins were visible in controls. The few biotinylated proteins observed in wildtype
232 littermates likely represent the endogenous metabolic CoA carboxylases³⁶. Due to podocin's ability
233 to oligomerize and the heterozygous nature of the mice, we would expect that endogenous, non-
234 tagged podocin would be biotinylated as well as podocin-BioID itself. When we probed the
235 Western blot for podocin, we observed two bands within the *Nphs2^{BioID2/+}* sample: one band at
236 approximately 50 kDa, the predicted endogenous podocin molecular weight without the BioID2 tag
237 (Figure 3C, denoted with an asterisk), and a second larger protein, podocin-BioID (Figure 3C,
238 denoted with arrowhead). No bands for podocin or podocin-BioID were detected in controls, as
239 expected. Additionally, the HA signal on the BioID2 protein was only detected in our *Nphs2^{BioID2/+}*
240 protein lysates confirming the purity and specificity of our results (Figure 3B). We went on to test if
241 biotin could cross the placental barrier to be delivered to embryonic pups *via* injection of the
242 pregnant dam. Pregnant dams were injected each day for one week, from E11.5-E18.5,
243 subcutaneously with 5 mg/kg biotin. Pups were then collected at P0. We analyzed the kidney
244 cortex and observed a strong streptavidin signal within the glomeruli of P0, *Nphs2^{BioID2/+}* mice (Fig
245 3D, arrowheads). Contrarily, we did not observe signal in wildtype control littermate mice.
246

247 Together, these data highlight the efficacy and specificity of our podocin-BioID model which can be
248 utilized across a spectrum of ages.

249

250 **Identification of the podocyte foot process proteome by mass spectrometry profiling**

251 Kidney cortices of three 8 to 10-week-old, sex matched mice were collected as one
252 biological replicate, after biotin administration for 1 week. All MS analyses were run in triplicate *i.e.*
253 9 mice per condition, totaling 18 mice (*Nphs2*^{BioID2/+} vs control littermates) per MS analysis. To
254 representatively capture the podocyte foot process proteome, we combined the results of three
255 separate MS analyses, representing 54 total mice (Figure 4). Significant sex differences were not
256 apparent in our studies (Supplemental Tables II-IV). From our proteomics analysis 11 proteins
257 were found across all three MS analyses to have an averaged Log₂ fold change ≥ 2.5 . Many of
258 these top proteins including podocin, Kirrel, Tjp1, Pard3, Magi2, Dnd, and Synpo are documented
259 to localize to the slit diaphragm.³⁷ Yet others including an Immunoglobulin like domain containing
260 receptor 2 (Ildr2) and a Formin binding protein 1 like (Fnbp1l, also known as Toca1) were, until
261 now, unreported components of the podocyte foot process/slit diaphragm. Additionally, 6 proteins
262 were identified across two MS analyses as significantly unregulated with an average Log₂ fold
263 change ≥ 1.75 . These include documented slit diaphragm components Tjp2 and Cd2ap (Figure
264 4A). All top 17 proteins had a stringent Log₂ fold change ≥ 1.75 . Tables listing the significant foot
265 process proteins identified from each MS analysis are reported in Supplemental Tables II – IV. To
266 add support to our relative Log₂ fold cut off, we assayed an immunoglobulin superfamily adhesion
267 molecule, Jam1/F11r,³⁸ with an observed Log₂ fold expression change of 0.7 (Supplemental Table
268 II). We identified Jam1 expression in cells of the proximal convoluted tubule, abutting the
269 glomerulus, (Supplemental Figure 1) but not within the glomerulus. Potentially, non-glomerular
270 cortex proteins that are biotinylated are also isolated although these appear minimal in our
271 findings. However, this helped establish a relative fold-cutoff for which we start to identify non-
272 podocyte proteins.

273 To surmount a complete list of podocyte foot process proteins we established a Log₂ fold
274 change cut off at 1.2 across all three mass spec analyses, and excluded histone, ribosome, and
275 mitochondrial proteins to arrive at a catalog of 54 proteins (Supplemental Table V). Graphically
276 depicting the compiled proteome in a volcano plot with the total ~1400 proteins identified and
277 cataloging proteins with a Log₂ fold change ≥ 1.75 and *p*-value ≤ 0.05 in green, proteins found to
278 have a *p*-value ≤ 0.05 in blue and proteins not found to be significant in grey (Figure 4B,
279 Supplemental Table V). The blue dotted line represents a $-\text{Log}_{10}(\textit{p}\text{-value} \leq 0.05)$ (Figure 4B). All
280 significantly identified proteins (*p* ≤ 0.05) had at least two unique peptides identified via MS
281 analysis. The most highly detected and significant proteins from our proteomic profiling, clustering
282 with documented slit diaphragm components, are found in the right scatter of the volcano plot,
283 depicted with green dots (Figure 4B, Supplemental Table V).

284 To interrogate our proteomic findings further, the top 54 podocyte foot process proteins
285 were utilized for *in silico* analyses. We input Supplemental Table V into *Qiagen Ingenuity Pathway*
286 *Analysis (IPA)* and performed a variant effect analysis to compute a proposed interactome based
287 on published literature (Figure 4C). The representative web of interactions from IPA was color
288 coded based on the number of MS analyses each protein appeared in, one (yellow), two (light
289 green), and three (dark green) (Figure 4C). Two novel foot process proteins were identified by IPA,
290 Ildr2 and Fnbp1l, to be involved in the interactome with connections to Afadin and actin,
291 respectively (Figure 4C). We added two dotted magenta lines for Ildr2 and Fnbp1l potential
292 interactions with podocin (Figure 4C). Unshaded proteins and dashed lines are predicted
293 interactors/interactions from IPA. Our IPA proposed network includes 26 of our 54 input foot
294 process proteins. The IPA interactome identifies three main nodes, *i.e.* junctions, cytoskeleton, and
295 signaling (Figure 4D). We highlighted the respective proteins that contribute to each node for

296 junctions (cyan), cytoskeleton (magenta), and signaling (orange) (Figure 4D). We next input these
297 54 proteins into the *Database for Annotation, Visualization, and Integrated Discovery (DAVID)* to
298 identify the gene ontology (GO) terms that are most highly enriched across our foot process
299 proteome. DAVID analysis identified cytoskeleton protein binding, cell-cell junctions, and actin
300 filament-based processes as the top molecular function, cellular component, and biological
301 processes GO terms, respectively (Figure 5A). Additionally, DAVID and IPA overlap in their
302 representation of junctional signaling and actin binding as top GO terms and canonical pathway
303 respectively. Taken together, these findings align with the major functional roles of podocin
304 and other foot process/slit diaphragm components.

305 To further decipher the contributions of our top 54 podocyte foot process proteins to
306 junctions and cell-cell contacts we cataloged the protein domains represented within each protein.
307 We utilized binary counting for the presence and absence of a domain. We did not account for the
308 number of same/similar domain(s), *i.e.* SH2/3, within a protein. We identified 7 top protein domains
309 within the catalog of the podocyte foot process proteome that included SH, PDZ, FERM and Ig-like
310 domains among others (Figure 5B). All of these top protein domains align with the nodes of the
311 podocyte foot process proteome, *i.e.* junctions, cytoskeleton, and signaling.

312 313 **Ildr2 and Fnbp11 are expressed by podocytes and co-localize with podocin**

314 Our proteomic analyses uncovered several proteins which have not been previously
315 described to localized to the podocyte foot process or have podocyte-specific functions. We
316 therefore wanted to validate their expression in podocytes and any colocalization with podocin. We
317 utilized immunofluorescence on kidney sections to visualize the location of three proteins in
318 particular: Myozap, Fnbp11, and Ildr2. First, a known slit diaphragm and foot process component
319 which was identified in our proteomics, Pard3, was assessed for its colocalization with podocin.
320 Pard3 both exhibited positive staining in the glomerulus and overlapped with the HA signal of
321 podocin-BioID (Figure 6A). Pard3 positive staining is also found in the adjacent tubule cells where
322 it helps maintain epithelial integrity (Figure 5A).³⁹ Myozap regulates cardiac function through Rho-
323 dependent activity and interacts with junctional proteins such as ZO-1⁴⁰. It was identified across
324 two of the three MS analyses (Figure 4A) and therefore we decided to investigate its localization.
325 Utilizing an antibody against a synthetic human MYOZAP peptide,⁴¹ we identified strong signal of
326 Myozap in the kidney endothelium, both in the glomerular capillaries and outside of glomerular
327 structures (Supplemental Figure 2). Myozap exhibits some degree of overlap with podocin,
328 however, the majority of Myozap protein detection does not colocalize with podocin, suggestive of
329 additional roles outside of podocytes (Supplemental Figure 2).

330 We identified Fnbp11, a documented junctional and actin organizing protein,^{42, 43} across all
331 three MS analyses with a Log₂ fold change > 4 (Figure 4). Fnbp11 has been identified in human
332 and mouse podocytes from single cell RNA-seq analysis and linked to podocyte cytoskeleton
333 dynamics *in vitro*, although it has not been documented to colocalize with the slit diaphragm or foot
334 process-associated proteins.^{44,45} We found that Fnbp11 co-localizes with podocin in continuous
335 stretches within glomeruli observed as a white signal from the Fnbp11 (magenta) and podocin
336 (green) overlap (Figure 6C). *In situ* hybridization confirms the glomerular expression of *Fnbp11*
337 (Figure 7C' arrowhead), similar to *Nphs2* (Figure 7A), in addition to a tubular expression pattern at
338 postnatal day 2 (P2).

339 Ildr2, a member of the B7 superfamily of immunoglobulins, is found highly enriched in the
340 podocyte foot process proteome across all MS profiles with an average Log₂ fold change of 4.9
341 (Figure 4). Ildr2 is a member of the angulin family and localizes to tricellular junctions of *in vitro*
342 cultured epithelial cells⁴⁶. In the kidney, Ildr2 exhibited a punctate staining pattern that colocalized
343 with podocin in adult mouse glomeruli, reminiscent of the punctate and restricted pattern of
344 tricellular junction staining observed *in vitro* (Figure 6B, 6D arrowheads)⁴⁶. In the z dimension we
345 observe overlap of Ildr2 (magenta) with podocin (green) as white punctate foci denoted by

346 arrowheads (Figure 6D). We further validated *Ildr2* expression within glomeruli via *in situ*
347 hybridization. *Ildr2* expression is found in glomeruli (Figure 7B' arrowhead) and tubule cells of the
348 kidney (Figure 7B' arrow) in P2 mice. We went on to verify *Ildr2* localization within early renal
349 vesicles, comma, and S-shaped bodies of developing nephrons at E15.5 (Figure 8B, Supplemental
350 Figure 3). *Ildr2* is more membranous and contiguous yet with some punctate detection in early
351 embryonic stages (E15.5) both within podocytes and cells of the developing nephron tubule
352 (Figure 8B). Collectively these studies provide evidence that *Ildr2* and *Fnbp1l* are novel podocyte
353 foot process and potentially slit diaphragm components that likely play roles in helping to maintain
354 podocyte architecture.

355

356 ***Ildr2* protein levels increase in both mouse and human glomeruli**

357 To determine whether our podocin-BioID model can detect changes to the localized
358 proteome in aging, we performed proteomics on 108-week-old male *Nphs2^{BioID2/+}* mice and
359 compared the results to our 8-10 week old *Nphs2^{BioID2/+}* male mice to assess any changes (Figure
360 8A). We identified significant increases in *Tjp2* and *Pkp4* and the largest change (2.76-fold) in *Ildr2*
361 (Figure 8A). We were unable to detect any significant decrease in proteins at $p \leq 0.05$, although
362 *Fnbp1l* and *Tns2* showed a decreasing trend. We observed minimal change in podocin when
363 comparing the two age groups (Figure 8A). To assess the human relevance of our findings, we
364 assayed ILDR2 immunofluorescent staining in young (age ~30 years) and aged (91-year-old)
365 human kidney sections. ILDR2 displayed a similar punctate staining pattern in young human
366 glomeruli. In correlation with our findings from the mouse, we found an increase in ILDR2 staining
367 in the aged glomeruli. Interestingly, the expression pattern no longer displays a punctate pattern
368 but rather a more diffuse membranous staining pattern (Figure 8C). We quantified the corrected
369 total glomerular florescence (CTGF) by selecting the glomerulus as a region of interest (gROI) then
370 quantifying total florescence intensity and subtracting out the mean background florescence for the
371 glomerular area, *i.e.* total gROI florescence – (glomerular area x mean background florescence) =
372 CTGF, (Figure 9A). We confirmed a significant ($p \leq 0.007$) increase in *Ildr2* in aged human
373 glomeruli compared to young human kidney tissue (Figure 9A).

374

375 **Discussion**

376 Podocytes are extraordinary epithelial cells of the kidney that intertwine their foot process
377 extensions to establish a cellular junction, the slit diaphragm, that is distinct from other cellular
378 junctions in the human body. The slit diaphragm was identified more than five decades ago as an
379 electron dense region between two podocyte foot processes, visualized beautifully by EM.^{47,48}
380 Many proteins that compose the slit diaphragm when mutated are associated with nephrotic
381 diseases, including nephrin, podocin, *Magi2*, and *Cd2ap*.⁴⁹ Loss of podocyte integrity is one of the
382 most common clinical observations in kidney disease. End stage renal disease being a top 10
383 cause of death in the US necessitates the need to identify novel components of the slit diaphragm,
384 and how the slit diaphragm changes with disease, for the development of new therapeutic options
385 and biomarkers of disease severity.

386 We utilized a new *in vivo* biochemical tool to interrogate the proteome of the podocyte foot
387 process *via* knock-in of a BioID moiety, generating our podocin-BioID model. The sensitivity and
388 advantage of BioID is that it allows for weak and transient interactions to be identified, in addition
389 to withstanding harsh isolation conditions.⁶ Further, the biotin-streptavidin bond is one of the
390 strongest known non-covalent interactions, enhancing the isolation of biotinylated proteins via
391 streptavidin-coated magnetic bead. We validated our model recapitulates normal podocin
392 localization by TEM and showing podocin-BioID localizes normally to the slit diaphragm. Activity of
393 the biotin ligase was confirmed through probing kidney sections and lysates with streptavidin and
394 finding an enrichment of biotinylated proteins. Our proteomics profiling identified more than 50

395 candidate molecules with significant enrichment in the podocyte foot process, $\text{Log}_2 \geq 1.2$. Within
396 this dataset we were able to identify novel candidates not found in previous investigations of the
397 slit diaphragm proteome^{22,23}. Additionally, we were able to identify changes to the localized
398 proteome that occur with aging. It would be interesting to compare the proteome across additional
399 stages such as during development. Podocytes begin as a columnar epithelium with only tight and
400 adherens junctions which remodel and later mature to form the specialized slit diaphragm
401 complex.¹⁶ With the ability of biotin to cross the placental barrier, the proteome could be compared
402 from development to maturity to identify changes that may help inform how these specialized
403 junctions are formed.

404 The proteomics analysis revealed potential nuances of the podocyte foot process that are
405 still under investigation. We identified 11 proteins that repeated over all three MS profiles.
406 However, there were more than 30 proteins that only surfaced in a single MS analysis and split
407 across the three MS analyses. While this may be due to experimental variability, such as in the
408 isolation of proteins, this may also highlight some differences in biological activity in the foot
409 process. The dynamics, variability, and protein turnover in the podocyte slit diaphragm is relatively
410 unknown. Pointing to the relative variability of one documented component, Synaptopodin (Synpo),
411 across the three MS analyses the respective Log_2 fold changes were observed at 1.0, 2.9, and 4.8
412 which indicates potential protein turn over, variability in the slit diaphragm components, or potential
413 variability from MS to MS. Further still, a second documented slit diaphragm protein, Cd2ap, was
414 only identified in two of the MS profiles. These confounding issues made a single MS analysis a
415 limited view, or snapshot, of the proteins present within the podocyte foot process. By combining
416 three separate MS analysis we have uncovered a more complete profile of the podocyte foot
417 process and slit diaphragm. Many of the top candidates identified in the podocyte foot process
418 proteome are well documented slit diaphragm components including Kirrel, Nphs2, Par3, Magi1/2,
419 Tjp1/2/3, Dnd, Synpo, and Cd2ap. Furthermore, our *in silico* analysis utilizing DAVID highlights
420 anticipated GO terms, including actin binding, cell-cell junctions, adherens junctions, and
421 cytoskeleton organization that align with podocyte function. We conclude the podocin-BioID model
422 provides a spatial specific approach to identify proteins that are notoriously difficult to isolate.

423 We cannot rule out biotin delivery and metabolism may limit some proteins from being
424 detected. One report depicts a time lapse of biotin administration *in vivo* with positive streptavidin
425 enrichment for as long as 18-hour after biotin administration.^{50,51} However, biotin requires an
426 accessible primary amine within a peptide to biotinylate. Proteins with little open structure or a
427 limited number of lysine residues could be missed by the labeling strategy. The possibility that
428 proteins were missed is brought to light by the inability to identify nephrin (*Nphs1*) across any of
429 the mass spec analyses run. One rational for the inability to identify nephrin, a known slit
430 diaphragm molecule that has been shown to interact with podocin, posits that its C-terminal
431 domain is only minimally assessable to podocin, while the remaining majority of the 180 kDa
432 protein is spanning the extracellular space of the slit diaphragm.²⁷ Therefore, while there are
433 significant advantages to the BioID system over traditional immunoprecipitations followed by MS, it
434 is also subject to missing important interactions.

435 One of the novel foot process candidates we identified, Fnbp11, has multiple roles in
436 microtubule binding, cell polarity, motility, actin organization, junctional localization and
437 signaling.^{42,43} Based on these roles, we hypothesize that Fnbp11 similarly helps maintain the slit
438 diaphragm and foot process integrity through associations with the actin cytoskeleton and links to
439 the slit diaphragm. Single cell RNA-seq analyses have previously found *Fnbp11* expression in
440 human⁴⁴ and mouse podocytes and tubule cells.⁴⁵ From the Kidney Interactive Transcriptomics
441 (KIT), *Fnbp11* is most highly expressed in podocytes compared to the tubule cells of the human
442 kidney.⁵² Further, *Fnbp11* is also expressed in the zebrafish pronephros⁵³ with a similar pattern to
443 other zebrafish tight junction proteins such as ZO-1/2⁵⁴, however the specific expression of *Fnbp11*

444 within the zebrafish podocytes remains unknown. With the conservation of *Fnbpl1* expression in
445 the renal system across vertebrates, it likely plays an important role in helping maintain epithelial
446 integrity in the various cells of the nephron, including podocytes.

447 *Ildr2* was identified in the podocyte foot process/slit diaphragm proteome across all three
448 MS profiles with a Log_2 fold change ≥ 4.5 and a p -value ≤ 0.007 . *Ildr2* belongs to the B7/CD28
449 family of proteins, encompassed by the Ig superfamily (IgSF), with pivotal roles in
450 immunomodulation and maintenance of peripheral self-tolerance.⁵⁵ *Ildr2* evinces
451 immunomodulatory activity, wherein administration of *Ildr2* as a fusion protein (ILDR2-Fc)
452 rebalances immune homeostasis, which leads to an amelioration of autoimmune disease states in
453 mouse models of rheumatoid arthritis, type I diabetes, and relapsing-remitting multiple sclerosis.⁵⁵⁻
454 ^{56,57} Recently, an *Ildr2* blocking antibody, BAY 1905254, was generated to block the
455 immunosuppressive activity of *Ildr2* for cancer immunotherapy.⁵⁷ BAY 1905254 promotes T-cell
456 activation *in vitro* and enhances antigen-specific T-cell proliferation and cytotoxicity *in vivo*, and is
457 currently in phase I clinical trials.⁵⁷ *Ildr2* presents an unexplored niche in podocyte biology centered
458 around the function of podocytes in immune cell modulation. Yet, the ability for immune cells such
459 as T-cells to interreact with podocytes is challenged by the podocyte cellular environment and the
460 GBM. Therefore, whether *Ildr2* could play an immune related role in podocytes remains tentative.

461 *Ildr2/ILDR2* is found to be specifically expressed in mouse and human podocytes from
462 publicly available databases including KIT.^{44,58} *Ildr2* was also identified as a *Wt1* transcriptional
463 target in podocytes by ChIP-seq.⁵⁹ In early embryonic and postnatal mouse kidneys, *Ildr2/Ildr2* is
464 expressed and localized to tubule cells and podocytes. However, in the adult kidney *Ildr2*
465 localization becomes restricted to podocytes. At the timepoints of podocyte development, we
466 observe a more membranous and contiguous pattern of *Ildr2* in comma and s-shaped bodies, with
467 some foci of heightened detection. In mature glomeruli, *Ildr2* is restricted to punctate foci that
468 colocalize with podocin. *Ildr2* has been identified at the site of tricellular tight junctions (tTJ) in
469 murine retinal pigment epithelium and *in vitro* within EpH4, a mouse mammary gland cell line.^{46,56}
470 Additionally, *Ildr2* has recently been identified to interact with Afadin in human embryonic kidney
471 cells (HEK293).⁶⁰ Afadin is also reported to localize to the site of specialized tricellular junctions
472 and mediate mechanotransduction.⁶¹ The role of mechanical strain present from the underlying
473 fluid flow shear stress on these specialized tTJs and recruitment of specific proteins to these
474 domains remains unresolved. Many proteins identified in the podocyte foot process proteome are
475 documented junctional proteins containing classified SH, PDZ, FERM, transmembrane, EF-Hand,
476 and Ig-like domains. Yet, Ig-like domain containing proteins were a considerably smaller
477 population. It is intriguing to speculate that Ig-like domains or a combination of PDZ, SH, and Ig-
478 like domain aids in the recruitment of specific proteins to specialized junctions such as tTJs and the
479 slit diaphragm. Further still, the requirement of these proteins for managing stress such as from
480 changes in fluid flow from the fenestrated endothelium and conversely the potential requirement of
481 mechanostress for recruitment of proteins to these tTJs and slit diaphragms remains an area in
482 need of further investigation.

483 In our aged podocin-BioID mice as well as our aged human kidney sample, we identified an
484 increase in *Ildr2* within podocytes. The pattern of *Ildr2* is more membranous with some punctate
485 foci in embryonic renal structures yet becomes detectable only as punctate foci as the mouse
486 matures. Proteomic profiling of 108-week-old, aged mice identify a significant increase in *Ildr2*
487 detection. We validated *Ildr2* significantly increases in aged (91 yo) human glomeruli via
488 quantifying the corrected total glomerular florescence of young and aged human glomeruli. We
489 further noted that in the aged human glomeruli *Ildr2* is detected higher in zones where podocin is
490 less detected and conversely where podocin is detected high *Ildr2* is less abundant. Aged human
491 glomeruli present an *Ildr2* pattern that more closely resembles the mouse embryonic stage with a
492 contiguous pattern rather than the punctate pattern of younger mice. We hypothesize that *Ildr2* is a

493 tight junction component and increasing Ildr2 protein in aged podocytes helps maintain podocyte
494 integrity with age. The additional increase of tight junction and desmosome associated proteins
495 Tjp2 and Pkp4, respectively, in our aged mouse proteome further supports this hypothesis.

496 In this study, we developed an innovative tool for the identification of novel proteins within
497 spatially restricted podocyte foot process/ slit diaphragm. Current efforts are now aimed at
498 uncovering proteins differentially regulated during slit diaphragm development, aging, and in renal
499 disease. It is crucial we uncover the changing composition of the podocyte slit diaphragm and foot
500 process as it holds potential for new therapeutic treatment targets to either preserve or prevent the
501 loss of podocyte integrity in kidney disease.

502

503 **Methods**

504 *Genetic CRISPR/Cas9 engineering of the Nphs2 locus to append a BioID2 moiety*
505 CRISPR/Cas9 targeting, and donor vector design were performed by UNC Chapel Hill Animal
506 Models Core. *Benchling* software was used to identify Cas9 short guide RNAs (sgRNA)
507 overlapping the podocin (*Nphs2*) stop codon. Guide RNAs were cloned into a T7 promoter vector
508 followed by *in vitro* transcription and spin column purification. Functional testing was performed by
509 transfecting a mouse embryonic fibroblast cell line with sgRNA and Cas9 protein (produced and
510 purified by the UNC Protein Expression Core). The sgRNA target region was amplified from
511 transfected cells and analyzed by T7 endo1 nuclease assay (New England Biolabs). sgRNA,
512 *Nphs2-g78B* (protospacer sequence 5'-gCCATTCGCCTATAACAT-3'; lower case g indicates
513 heterologous guanine added at 5' end of native sequence for efficient T7 *in vitro* transcription) was
514 selected for genome editing in embryos. *Nphs2* was amplified from adult mouse kidney cDNA and
515 cloned into the MCS-BioID2-HA plasmid (plasmid was a gift from Kyle Roux; Addgene plasmid #
516 74224 ; <http://n2t.net/addgene:74224> ; RRID:Addgene_74224).³⁰ A donor vector was subsequently
517 constructed from the *Nphs2*-BioID2-HA plasmid with the following features: (1) a 1018 bp 5'
518 homology arm encompassing sequence immediately 5' of the *Nphs2* stop codon including 276 bp
519 coding sequence from *Nphs2* exon 8, (2) a 267 bp in-frame Glycine/Serine-rich linker sequence,
520 (3) a 696 bp coding sequence for the humanized biotin ligase of *A. aeolicus* with a R40G mutation
521 in the catalytic domain (BioID2)³⁰, (4) HA Tag, (5) 2X Stop codon, (6) a FRT site, and (7) a 1019 bp
522 3' homology arm, beginning at the *Nphs2*-sgRNA cut site. The donor vector was designed to
523 produce a final knock-in allele which would produce a fusion protein of podocin C-terminally linked
524 to BioID2.

525

526 *Embryo microinjection*

527 C57BL/6J zygotes were microinjected with 400nM Cas9 protein, 25 ng/μl sgRNA and 20 ng/μl
528 supercoiled double-stranded donor plasmid (Mix1), or 200 nM Cas9 protein, 12.5 ng/μl sgRNA and
529 10 ng/μl donor plasmid (Mix2). Injected embryos were implanted in pseudopregnant B6D2F1
530 recipient females. Fourteen resulting pups (9 from Mix1 and 7 from Mix2) were screened by PCR
531 for the presence of the knock-in allele. One female (Founder #2) and one male (Founder #6) were
532 positive for the correct single-copy knock-in allele. Founders #2 and #6 were mated to wild-type
533 C57BL/6J animals for transmission of the knock-in allele. Both founders transmitted the correct
534 knock-in allele to offspring. Injections, genotyping of founders, and off-site targeting analysis was
535 performed by UNC Chapel Hill Animal Models Core.

536

537 *Genotyping*

538 A mouse tail or ear clip was taken and dissociated with Viagen DirectPCR Lysis Reagent
539 (Mouse Tail) containing 10 μg/mL proteinase K incubated at 55°C overnight and denatured at 95
540 °C for 10 min. PCR was run with ($T_{\text{annealing}} = 63.5^{\circ}\text{C}$), elongation for 40 sec, for 35 cycles. Primer
541 sequences utilized for genotyping are Common Forward: 5'-CTTTTGTCTCTCCCGCAA-3',

542 podocin WT Reverse 5'-TGCATGTAGCCATCTTGTGACT-3', *Nphs2*^{BioID2} Reverse 5'-
543 CTGCCCTTGGTCTGTCTGTC-3'.
544

545 *Kidney cortex isolation and lysis*

546 Mice were raised, housed, and handled in accordance with IACUC protocol number 19-
547 183.0/22-136.0. 8–10-week-old mice were injected subcutaneously with 5 mg/kg biotin every day
548 for one week. We surgically isolated the cortex of the kidney to enrich for the glomerular fraction,
549 using a scalpel in cold sterile phosphate buffered saline (PBS). A single biological sample was
550 composed of the isolated kidney cortex of three same sex mice for a total of six kidney cortexes
551 per sample (2 kidneys per animal x 3 mice). The sample was then homogenized via a glass
552 Dounce homogenizer. Samples were centrifuged at 4 °C, 5000 × g for 10 minutes. Supernatant
553 was decanted and the tissue pellets snap frozen in liquid nitrogen and stored at -80 °C. Care was
554 taken to utilize sterile Eppendorf tubes that had not been autoclaved as we identified a
555 polyethylene glycol contaminant in a preliminary MS analysis that may arise from autoclaving
556 plastic utilized. Samples were removed from the freezer and allowed to equilibrate on ice for 2
557 hours. Lysis buffer (8M urea, 50mM Tris-HCl pH 7.4, 500mM NaCl, 2.5mM EDTA, 2.5mM EGTA,
558 1.5mM MgCl₂, 1.5mM DTT, 0.25% NP-40, 1% SDS, 1x protease inhibitors (Roche cOmplete Mini
559 EDTA-free, Sigma)) were then added to resuspend the pellet and allowed to nutate at 4°C for one
560 hour. The protein homogenate was sonicated (3 pulses for 10 sec at 30% duty) and centrifuged
561 (4°C, 12000 rpm for 10 min). The supernatant was then removed for subsequent quantification and
562 analysis.
563

564 *Biotinylated protein capture*

565 Kidney cortex-isolated protein lysates were serial diluted and run-in triplicate on a 96-well
566 plate reader at 590nm wavelength (Synergy HT, BioTek). A standard curve of bovine serum
567 albumin (BSA) was utilized as a control. Protein concentrations of each lysate were calculated, and
568 10mg of crude protein lysate was loaded with 100µl of streptavidin-coated magnetic beads
569 (Dynabeads MyOne Streptavidin C1, Invitrogen). Samples containing beads and protein lysate
570 were rotated end over end at 4°C overnight. Supernatant was removed using a magnetic strip, and
571 the bead-captured fraction was washed once with lysis buffer. After the first wash with lysis buffer
572 containing 1% SDS and 0.25 % NP-40 diminishing amounts of detergents were utilized in
573 subsequent washes until there was no detergents remaining in the wash buffer (after 4 washes).
574 Beads were then washed 3 times in ABC solution (50mM ammonium bicarbonate, 8.0 pH) and
575 sent to UNC Chapel Hill Hooker Proteomics Core. All procedures were performed the same for our
576 aged murine cohort with the exception that 5mg of crude protein lysate was loaded onto beads.

577 After the last wash buffer step, 50µl of 50mM ammonium bicarbonate (pH 8) containing 1 µg
578 trypsin (Promega) was added to beads overnight at 37°C with shaking. The next day, 500ng of
579 trypsin was added then incubated for an additional 3h at 37°C with shaking. Supernatants from
580 pelleted beads were transferred, then beads were washed twice with 50ul LC/MS grade water.
581 These rinses were combined with original supernatant, then acidified to 2% formic acid. Peptides
582 were desalted with peptide desalting spin columns (Thermo Scientific) and dried via vacuum
583 centrifugation. Peptide samples were stored at -80°C until further analysis.
584

585 *LC/MS/MS analysis*

586 Each sample was analyzed by LC-MS/MS using an Easy nLC 1200 coupled to a QExactive
587 HF (Thermo Scientific). Samples were injected onto an Easy Spray PepMap C18 column (75µm id
588 × 25cm, 2µm particle size) (Thermo Scientific) and separated over a 120 min method. The gradient
589 for separation consisted of a step gradient from 5 to 36 to 48% mobile phase B at a 250 nl/min flow
590 rate, where mobile phase A was 0.1% formic acid in water and mobile phase B consisted of 0.1%
591 formic acid in ACN. The QExactive HF was operated in data-dependent mode where the 15 most

592 intense precursors were selected for subsequent HCD fragmentation. Resolution for the precursor
593 scan (m/z 350–1700) was set to 60,000 with a target value of 3×10^6 ions, 100ms inject time.
594 MS/MS scans resolution was set to 15,000 with a target value of 1×10^5 ions, 75ms inject time.
595 The normalized collision energy was set to 27% for HCD, with an isolation window of 1.6m/z.
596 Peptide match was set to preferred, and precursors with unknown charge or a charge state of 1
597 and ≥ 8 were excluded.

598

599 *Western blot*

600 Biotinylated proteins attached to streptavidin coated bead were eluted off with excess biotin
601 [200 mM] in 200 mM Tris HCl pH: 6.8, 40% glycerol, 8 % beta mercaptoethanol, 2 % SDS, 0.04 %
602 bromophenol blue at 95°C for 30 min). Bead slurry mix was placed on a magnet and isolated
603 biotinylated lysate was collected for subsequent analysis. Protein sample fractions were removed
604 and loaded into a Novex WedgeWell gel (4-20% Tris-Glycine gradient gel, Invitrogen, XP04202),
605 and run in 25mM Tris-HCl, 190mM Glycine, 0.1% SDS, pH 8.3. Proteins were transferred from gel
606 to nitrocellulose membrane in 25mM Tris-HCl, 190mM Glycine, and 20% methanol. The membrane
607 was blocked in 3% bovine serum albumin in 1x TBST (Tris base Saline Solution (25mM Tris-HCl
608 pH 7.5, 150mM NaCl) with 0.1% Tween-20, for 1 hour at room temperature. Primary antibodies
609 (Rabbit anti-HA tag (Cell Signaling, 3724S [1:500], mouse anti-NPHS2 (Proteintech, 20384-1-AP)
610 [1:500], Rabbit anti-podocin (Invitrogen, PA5-79757) [1:500], Streptavidin-HRP (Cell Signaling,
611 3999S) [1:1000] were applied in 3% BSA+ TBST. Membrane plus primary antibodies were allowed
612 to incubate overnight at 4°C with gentle nutation. Following 3x10 min washes with TBST,
613 membranes were probed with secondary antibodies conjugated to horseradish peroxidase (HRP)
614 (donkey and rabbit -HRP [1:500] or Goat anti mouse-HRP [1:500] and incubated for one hour at
615 room temperature Membranes were developed with enhanced chemiluminescence substrate
616 (ECL) and visualized on an iBright FL1000 (Invitrogen).

617

618 *Proteomics data analysis*

619 Raw data were processed using the MaxQuant software suite (version 1.6.12.0) for
620 identification and label-free quantitation.⁶² Data were searched against an Uniprot Reviewed
621 Mouse database (downloaded January 2021, containing 17,051 sequences) using the integrated
622 Andromeda search engine. A maximum of two missed tryptic cleavages was allowed. The variable
623 modification specified was oxidation of methionine, N-terminal acetylation, and phosphorylation of
624 Ser/Thr/Tyr. Label-free quantitation (LFQ) was enabled. Results were filtered to 1% FDR at the
625 unique peptide level and grouped into proteins within MaxQuant. Match between runs was
626 enabled. Data were filtered in Perseus, then imported into Argonaut for normalization, imputation
627 and statistical analysis.⁶³

628 We combined three separate MS analyses and averaged the Log_2 fold changes and respective p -
629 values of the top 17 proteins identified across all three MS profiles. QIAGEN Ingenuity Pathway
630 Analysis (IPA) was utilized to identify putative interactomes.

631

632 *Immunofluorescence*

633 Kidneys were harvested in cold filter sterilized PBS and fixed at 4°C for 1 hr in 4%
634 paraformaldehyde (PFA) in PBS. Samples were washed twice in 1x PBS, placed in 30% sucrose
635 overnight, and subsequently embedded in OCT. Kidneys were cut in 12 μm sections on a Leica
636 Cryostat CM 1850. Tissue sections were blocked in 3% donkey serum, 1% bovine serum albumin
637 (BSA), 1x PBS, 0.1 % TritonX-100 for 45 min at room temperature. Slides were incubated in
638 primary antibodies (see antibodies utilized below, Supplemental Table I) diluted in blocking buffer
639 for 1-2 hr. Slides were then rinsed 3x5 min in 1x PBST, after which they were incubated with Alexa
640 Fluor labeled secondary antibodies (Invitrogen) diluted (1:1000) in blocking buffer for 1 hr at room

541 temp. The slides were then rinsed 2 x 5 min with 1x PBST, 1x3–5 min with 1x PBS + 1ng/mL DAPI
542 and mounted in ProLong Gold antifade reagent (Invitrogen).

543 For double labeling tissue with two antibodies both raised in rabbit we utilized a Zenon
544 double labeling kit (Z25302, Invitrogen) with rabbit anti-Fnbp1l, rabbit anti-Ildr2, rabbit anti-podocin,
545 and rabbit anti-HA antibodies. The weaker of the two primary rabbit antibodies, typically Ildr2 and
546 Fnbp1l, was diluted in block solution then incubated for 90 min at room temperature. Slides were
547 washed 3-6x with 1xPBS +0.25% Triton-X 100 and subsequently incubated for 1hr at room
548 temperature with the appropriate Alexa Fluor-488 labeled secondary antibody diluted 1:1000 in
549 blocking buffer. The second primary rabbit antibody was mixed at a 1:2.5 ratio with the Zenon
550 fluorophore-647. Note the two fluorophores utilized are on opposite ends of the florescence
551 spectrum. The slides were then fixed in 4% PFA for 5 min at room temperature. And all
552 subsequent steps were carried out per normal immunofluorescence procedures as above. Images
553 were acquired utilizing a Zeiss 880 confocal microscope equipped with Airyscan super-resolution
554 and spectral imaging on Zen Microscopy Suite version 2.3 Sp1 that is part of the UNC Hooker
555 Imaging Core. Z-stack images were acquired in 1 μ m steps for Ildr2 and Fnbp1l.
556

557 *Immunogold electron microscopy*

558 Mouse kidneys were fixed for 1 hour at room temperature in 4% PFA in 0.15M sodium phosphate
559 buffer pH 7.4 (PB) or 2% PFA + 0.5% glutaraldehyde in 0.15M PB and immediately processed for
560 LR White resin embedding. Samples were washed in 0.15M PB, 3x10 minutes and dehydrated
561 using a Pelco BioWave Pro Microwave (Ted Pella, Inc.) as follows: at 40°C (750 watts): 30%
562 ethanol in water (ETOH) -1 min, 50% ETOH in water-1 min, 75% ETOH in water-1 min, and at
563 40°C (450 watts): 100% ETOH-1 min, 100% ETOH-1 min, 100% ETOH-1 min. Microwave
564 infiltration and embedment were carried out using the following schedule: 1 part 100% ETOH:2
565 part LR White resin-10 min at 40°C (350 watts), 2 exchanges of 100% LR White resin for 10 min at
566 50°C (350 watts). Samples were transferred to 00 gelatin capsules filled with fresh LR White resin
567 and polymerized overnight at 55°C; the temperature was adjusted to 60°C for 6 hours and allowed
568 to complete polymerization at room temperature for 72 hrs. Blocks were trimmed to the tissue and
569 1.0 μ m sections were cut using Leica Ultracut UCT (Leica Microsystems, Inc.) and a Diatome
570 diamond knife (Electron Microscopy Sciences). Sections were mounted on glass slides, stained
571 with 1% toluidine blue O in 1% sodium borate, and regions with glomeruli were selected and
572 trimmed.⁶⁴ Ultrathin sections (90 nm) were cut and mounted on formvar / carbon-coated 200 mesh
573 nickel grids. Before immunostaining, the sections were hydrated by floating the grids section-side
574 down on drops of deionized water. Sections were blocked with Aurion Goat Blocking Solution for
575 15 min and transferred to 15 μ l drops of the primary antisera diluted at [1: 500] for anti-HA and [1:
576 250] for anti-Podocin in 0.05M TBS+0.2% BSA-Ac, pH 7.6 (Rabbit anti-HA, Cell Signaling, 37245;
577 rabbit anti-Podocin, Invitrogen, PA5-79757). Sections were incubated overnight at 4°C followed by
578 4x10 min washes in TBS/BSA-Ac to remove unbound antibody. The grids were incubated in a
579 12nm Colloidal gold-AffiniPure goat anti-rabbit IgG (H+L) secondary antibody (Jackson Immuno,
580 Lot #148041) diluted at 1:50 in TBS/BSA-Ac for 2 hours at room temperature.⁶⁵ After 3 washes in
581 TBS/BSA-Ac and 3 washes in 0.15M PB, grids were post-fixed for 10 min in 1% glutaraldehyde in
582 0.15M PB followed by 3 washes in deionized water. The grids were stained with 4% aqueous
583 uranyl acetate for 5 min for additional contrast. Samples were observed using a JEOL JEM-1230
584 transmission electron microscope operating at 80kV (JEOL USA INC.), and images were taken
585 using a Gatan Orius SC1000 CCD camera with Gatan Microscopy Suite version 3.10.1002.0
586 software (Gatan, Inc.). Sample prep and imaging was performed at the UNC Microscopy Services
587 Laboratory, Department of Pathology and Laboratory Medicine.
588
589
590

591 *In situ hybridization*

592 Wildtype C57/Bl6J kidneys at postnatal day 2 (P2) were dissected in cold molecular grade
593 PBS (RNase/DNase free) and fixed in 4% PFA for 30 min at room temperature on a rocking
594 platform. Kidneys were washed in molecular grade PBS and placed in 30% sucrose. Kidneys were
595 embedded in OCT and 20µm sections were cut on a cryostat (Leica CM1850). Tissue sections
596 were fixed in 4% PFA and washed with 1x PBS. The tissue was permeabilized with proteinase K at
597 10µg/mL for 15 min and subsequently washed with 1x PBS. Tissue was then washed in an
598 acetylation solution (0.1 % HCl, 0.375 % Acetic Anhydride, and 0.75 % Triethanolamine in H₂O) for
599 10 min with stirring. Tissue sections were then subsequently washed 3x3min with PBS, rinsed
700 1x5min in 0.85 % NaCl, 1x5min in 70 % ethanol, and 1x5min in 95 % ethanol prior to riboprobe /
701 hybridization application. Antisense Digoxigenin (DIG) labeled riboprobes were hybridized to the
702 tissue in a solution containing 50% deionized formamide, 2 sodium citrate pH 4.5, 1% SDS,
703 50µg/mL heparin, 50µg/mL yeast tRNA overnight in a humidity chamber at 68°C. The following
704 day, specimens were treated with successive washes of sodium citrate buffer as described
705 previously,⁶⁶ and blocked in 10% heat inactivated sheep serum (HISS), with 2% Roche blocking
706 reagent (BR) in malic acid buffered solution with 0.1% tween-20 (MABT). Anti-DIG-Alkaline
707 Phosphatase (AP) antibody was applied in 1% HISS, 2% BR in MABT overnight at 4°C. The
708 following day the slides were washed in MABT and 100mM NaCl, 100 mM Tris-HCl pH 9.5, 50mM
709 MgCl₂, and 0.1 % Tween-20 (NTMT) with 2mM Levamisole to inhibit endogenous alkaline
710 phosphatase activity. Digoxigenin-UTP (Roche 53119620) labeled riboprobes were amplified from
711 cDNA libraries collected from mouse kidney tissue with the following primers:

712 Podocin forward primer: TGACGTTCCCTTTTCCATC, Podocin reverse primer with T7
713 underlined: CAGTGAATTGTAATACGACTCACTATAGGGGCTGTGGACAGCGACTGAAGA.
714 Ildr2 forward: GGAGAATCCTTGGGC and Ildr2 reverse:
715 CAGTGAATTGTAATACGACTCACTATAGGGGTACCCGGCCTTGGC were previously
716 published⁶⁶. Fnbp1l forward primer: GCTGAATGACAATTGTGTGAAC and Fnbp1l reverse:
717 CAGTGAATTGTAATACGACTCACTATAGGGGCTGTGCAAGTCCAAGTGTCTTC.

718
719 *Human kidney tissue*

720 Human kidney tissue samples were de-identified (young) or directly donated (91-year-old) and did
721 not necessitate IRB approval. Young, normal kidney tissue was obtained from the UNC Tissue
722 Procurement Facility as a frozen block. A small piece of tissue was removed with a razorblade,
723 fixed for 10 minutes in 4% paraformaldehyde and subsequent processing for cryosectioning and
724 immunofluorescence carried out as for the mouse (described above). For the old kidney tissue, a
725 fresh sample was excised from the kidney cortex and fixed for 10 minutes in 4% paraformaldehyde
726 prior to processing similar to the young tissue for immunofluorescence.

727
728 **Abbreviations**

729 4.1 protein, Ezrin, Radixin and Moesin (FERM), Corrected Total Glomerular Florecence (CTGF), E
730 and F helix-Hand (EF-Hand), End Stage Renal Disease (ESRD), Kidney Interactive
731 Transcriptomics (KIT), Gene Ontogeny (GO), Glomerular Basement Membrane (GBM), Mass
732 Spectrometry (MS), PSD-95, Disc large, and ZO – 1 (PDZ), Src homology (SH),

733
734 **Acknowledgements**

735 We would like to acknowledge the many people and core services at the University of North
736 Carolina at Chapel Hill who aided in this investigation. We specifically would like to thank Wendy
737 Salmon, Director of the Department of Cell Biology and Physiology's Hooker Imaging Core, Laura
738 Herring, Ph.D., Director of the School of Medicine's Michael Hooker Proteomics Center, and
739 Victoria Madden and Kristen White, providers of electron microscopy services in the Department of

740 Pathology and Laboratory Medicine's Microscopy Services Laboratory. Paul Risteff for training in
741 TEM and aid with image acquisition and sample preparation.

742 This research is based in part on work conducted at the Microscopy Services Laboratory
743 (TEM), the UNC Proteomics Core Facility (MS), and the UNC Hooker Imaging Core Facility
744 (confocal microscopy), which are supported in part by P30 CA016086 Cancer Center Core Support
745 Grant to the UNC Lineberger Comprehensive Cancer Center. We would further like to
746 acknowledge the members of the O'Brien lab for critical feedback on these studies. This research
747 was supported in part by a Vanderbilt O'Brien Kidney Center Pilot and Feasibility Award (P30-
748 DK114809), a UNC Junior Faculty Development Award, and Start-Up funds from UNC to LLO as
749 well as F32AR073649 to GFG.

750

751 References

- 752 (1) Quaggin, S. E.; Kreidberg, J. A. Development of the Renal Glomerulus: Good Neighbors and Good
753 Fences. *Development* **2008**, *135* (4), 609–620. <https://doi.org/10.1242/dev.001081>.
- 754 (2) Ichimura, K.; Miyazaki, N.; Sadayama, S.; Murata, K.; Koike, M.; Nakamura, K.; Ohta, K.; Sakai, T.
755 Three-Dimensional Architecture of Podocytes Revealed by Block-Face Scanning Electron Microscopy.
756 *Sci Rep* **2015**, *5* (1), 8993. <https://doi.org/10.1038/srep08993>.
- 757 (3) Reeves, W.; Caulfield, J. P.; Farquhar, M. G. Differentiation of Epithelial Foot Processes and Filtration
758 Slits: Sequential Appearance of Occluding Junctions, Epithelial Polyanion, and Slit Membranes in
759 Developing Glomeruli. *Lab Invest* **1978**, *39* (2), 90–100.
- 760 (4) Fukasawa, H.; Bornheimer, S.; Kudlicka, K.; Farquhar, M. G. Slit Diaphragms Contain Tight Junction
761 Proteins. *J Am Soc Nephrol* **2009**, *20* (7), 1491–1503. <https://doi.org/10.1681/ASN.2008101117>.
- 762 (5) Reiser, J.; Kriz, W.; Kretzler, M.; Mundel, P. The Glomerular Slit Diaphragm Is a Modified Adherens
763 Junction. *J Am Soc Nephrol* **2000**, *11* (1), 1–8. <https://doi.org/10.1681/ASN.V1111>.
- 764 (6) Kestilä, M.; Lenkkeri, U.; Männikkö, M.; Lamerdin, J.; McCready, P.; Putaala, H.; Ruotsalainen, V.;
765 Morita, T.; Nissinen, M.; Herva, R.; Kashtan, C. E.; Peltonen, L.; Holmberg, C.; Olsen, A.;
766 Tryggvason, K. Positionally Cloned Gene for a Novel Glomerular Protein--Nephrin--Is Mutated in
767 Congenital Nephrotic Syndrome. *Mol Cell* **1998**, *1* (4), 575–582. [https://doi.org/10.1016/s1097-](https://doi.org/10.1016/s1097-2765(00)80057-x)
768 [2765\(00\)80057-x](https://doi.org/10.1016/s1097-2765(00)80057-x).
- 769 (7) Boute, N.; Gribouval, O.; Roselli, S.; Benessy, F.; Lee, H.; Fuchshuber, A.; Dahan, K.; Gubler, M. C.;
770 Niaudet, P.; Antignac, C. NPHS2, Encoding the Glomerular Protein Podocin, Is Mutated in Autosomal
771 Recessive Steroid-Resistant Nephrotic Syndrome. *Nat Genet* **2000**, *24* (4), 349–354.
772 <https://doi.org/10.1038/74166>.
- 773 (8) Donoviel, D. B.; Freed, D. D.; Vogel, H.; Potter, D. G.; Hawkins, E.; Barrish, J. P.; Mathur, B. N.;
774 Turner, C. A.; Geske, R.; Montgomery, C. A.; Starbuck, M.; Brandt, M.; Gupta, A.; Ramirez-Solis, R.;
775 Zambrowicz, B. P.; Powell, D. R. Proteinuria and Perinatal Lethality in Mice Lacking NEPH1, a Novel
776 Protein with Homology to NEPHRIN. *Mol Cell Biol* **2001**, *21* (14), 4829–4836.
777 <https://doi.org/10.1128/MCB.21.14.4829-4836.2001>.
- 778 (9) Rodewald, R.; Karnovsky, M. J. POROUS SUBSTRUCTURE OF THE GLOMERULAR SLIT
779 DIAPHRAGM IN THE RAT AND MOUSE. *Journal of Cell Biology* **1974**, *60* (2), 423–433.
780 <https://doi.org/10.1083/jcb.60.2.423>.
- 781 (10) Karnovsky, M.; Ryan, G. Substructure of the Glomerular Slit Diaphragm in Freeze-Fractured Normal
782 Rat Kidney. *Journal of Cell Biology* **1975**, *65* (1), 233–236. <https://doi.org/10.1083/jcb.65.1.233>.
- 783 (11) Miyaki, T.; Kawasaki, Y.; Hosoyamada, Y.; Amari, T.; Kinoshita, M.; Matsuda, H.; Kakuta, S.; Sakai,
784 T.; Ichimura, K. Three-Dimensional Imaging of Podocyte Ultrastructure Using FE-SEM and FIB-SEM
785 Tomography. *Cell Tissue Res* **2020**, *379* (2), 245–254. <https://doi.org/10.1007/s00441-019-03118-3>.
- 786 (12) Pagtalunan, M. E.; Miller, P. L.; Jumping-Eagle, S.; Nelson, R. G.; Myers, B. D.; Rennke, H. G.;
787 Coplson, N. S.; Sun, L.; Meyer, T. W. Podocyte Loss and Progressive Glomerular Injury in Type II
788 Diabetes. *J Clin Invest* **1997**, *99* (2), 342–348. <https://doi.org/10.1172/JCI119163>.
- 789 (13) van den berg, J. G.; van den Bergh Weerman, M. A.; Assmann, K. J. M.; Weening, J. J.; Florquin, S.
790 Podocyte Foot Process Effacement Is Not Correlated with the Level of Proteinuria in Human

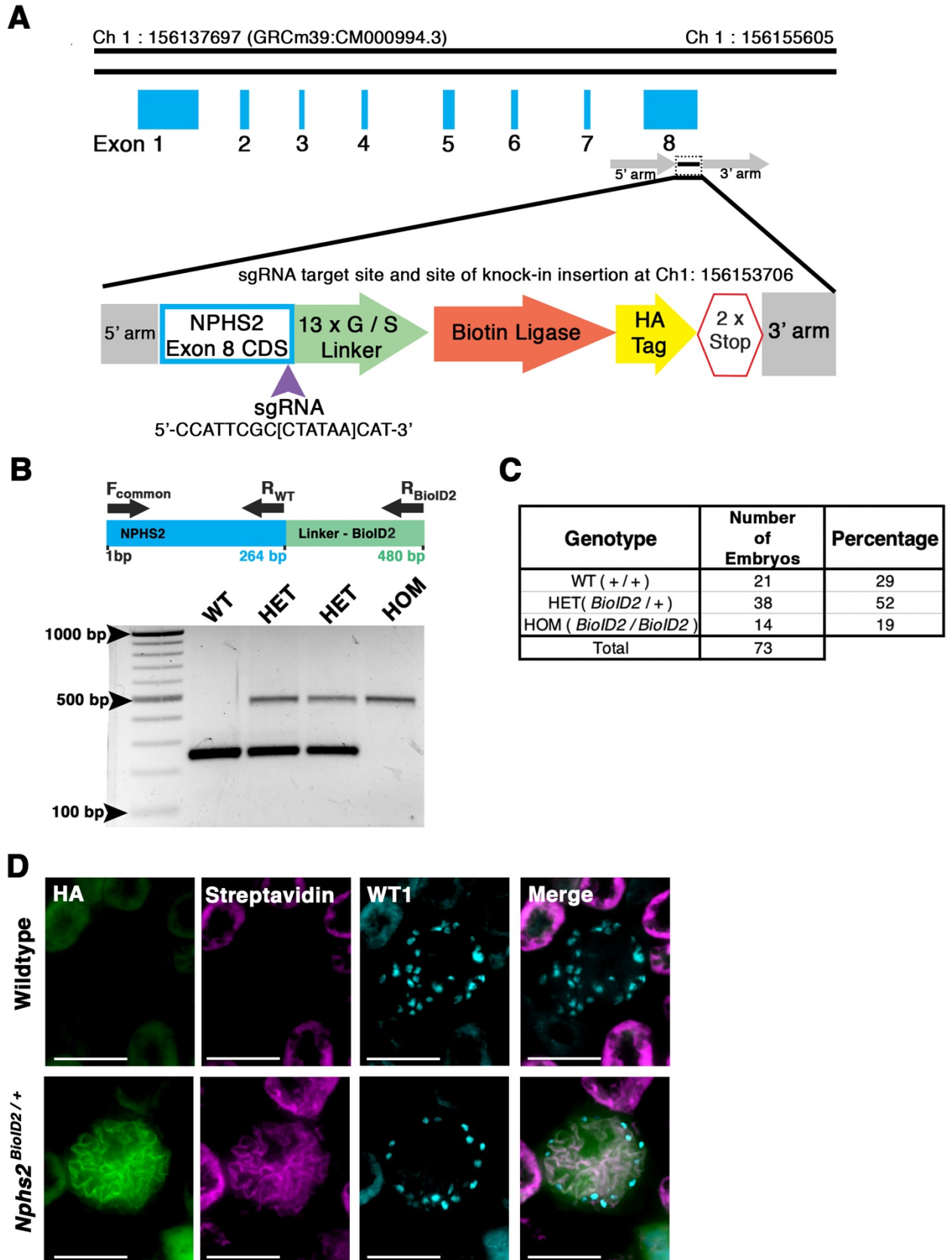
- 791 Glomerulopathies. *Kidney International* **2004**, *66* (5), 1901–1906. <https://doi.org/10.1111/j.1523-1755.2004.00964.x>.
- 792
- 793 (14) D’Agati, V. Pathologic Classification of Focal Segmental Glomerulosclerosis. *Seminars in Nephrology*
794 **2003**, *23* (2), 117–134. <https://doi.org/10.1053/snep.2003.50012>.
- 795 (15) Kopp, J. B.; Anders, H.-J.; Susztak, K.; Podestà, M. A.; Remuzzi, G.; Hildebrandt, F.; Romagnani, P.
796 Podocytopathies. *Nat Rev Dis Primers* **2020**, *6* (1), 68. <https://doi.org/10.1038/s41572-020-0196-7>.
- 797 (16) Bierzynska, A.; Soderquest, K.; Dean, P.; Colby, E.; Rollason, R.; Jones, C.; Inward, C. D.; McCarthy,
798 H. J.; Simpson, M. A.; Lord, G. M.; Williams, M.; Welsh, G. I.; Koziell, A. B.; Saleem, M. A. *MAGI2*
799 Mutations Cause Congenital Nephrotic Syndrome. *JASN* **2017**, *28* (5), 1614–1621.
800 <https://doi.org/10.1681/ASN.2016040387>.
- 801 (17) Gigante, M.; Pontrelli, P.; Montemurno, E.; Roca, L.; Aucella, F.; Penza, R.; Caridi, G.; Ranieri, E.;
802 Ghiggeri, G. M.; Gesualdo, L. CD2AP Mutations Are Associated with Sporadic Nephrotic Syndrome
803 and Focal Segmental Glomerulosclerosis (FSGS). *Nephrology Dialysis Transplantation* **2009**, *24* (6),
804 1858–1864. <https://doi.org/10.1093/ndt/gfn712>.
- 805 (18) Liu, Y.-X.; Zhang, A.-Q.; Luo, F.-M.; Sheng, Y.; Wang, C.-Y.; Dong, Y.; Fan, L.; Liu, L. Case Report:
806 A Novel Heterozygous Mutation of CD2AP in a Chinese Family With Proteinuria Leads to Focal
807 Segmental Glomerulosclerosis. *Front. Pediatr.* **2021**, *9*, 687455.
808 <https://doi.org/10.3389/fped.2021.687455>.
- 809 (19) Beltcheva, O.; Martin, P.; Lenkkeri, U.; Tryggvason, K. Mutation Spectrum in the Nephtrin Gene
810 (NPHS1) in Congenital Nephrotic Syndrome. *Hum Mutat* **2001**, *17* (5), 368–373.
811 <https://doi.org/10.1002/humu.1111>.
- 812 (20) Guaragna, M. S.; Lutaif, A. C. G. B.; Piveta, C. S. C.; Souza, M. L.; de Souza, S. R.; Henriques, T. B.;
813 Maciel-Guerra, A. T.; Belangero, V. M. S.; Guerra-Junior, G.; De Mello, M. P. NPHS2 Mutations
814 Account for Only 15% of Nephrotic Syndrome Cases. *BMC Med Genet* **2015**, *16*, 88.
815 <https://doi.org/10.1186/s12881-015-0231-9>.
- 816 (21) Lu, C.-C.; Wang, G.-H.; Lu, J.; Chen, P.-P.; Zhang, Y.; Hu, Z.-B.; Ma, K.-L. Role of Podocyte Injury in
817 Glomerulosclerosis. In *Renal Fibrosis: Mechanisms and Therapies*; Liu, B.-C., Lan, H.-Y., Lv, L.-L.,
818 Eds.; Advances in Experimental Medicine and Biology; Springer: Singapore, 2019; pp 195–232.
819 https://doi.org/10.1007/978-981-13-8871-2_10.
- 820 (22) Pierchala, B. A.; Muñoz, M. R.; Tsui, C. C. Proteomic Analysis of the Slit Diaphragm Complex: CLIC5
821 Is a Protein Critical for Podocyte Morphology and Function. *Kidney Int* **2010**, *78* (9), 868–882.
822 <https://doi.org/10.1038/ki.2010.212>.
- 823 (23) Kocylowski, M. K.; Aypek, H.; Bildl, W.; Helmstädter, M.; Trachte, P.; Dumoulin, B.; Wittösch, S.;
824 Kühne, L.; Aukschun, U.; Teetzen, C.; Kretz, O.; Gaal, B.; Kulik, A.; Antignac, C.; Mollet, G.;
825 Köttgen, A.; Göcmen, B.; Schwenk, J.; Schulte, U.; Huber, T. B.; Fakler, B.; Grahammer, F. A Slit-
826 Diaphragm-Associated Protein Network for Dynamic Control of Renal Filtration. *Nature*
827 *Communications* **2022**, *13* (1), 6446. <https://doi.org/10.1038/s41467-022-33748-1>.
- 828 (24) Roselli, S.; Gribouval, O.; Boute, N.; Sich, M.; Benessy, F.; Attié, T.; Gubler, M.-C.; Antignac, C.
829 Podocin Localizes in the Kidney to the Slit Diaphragm Area. *The American Journal of Pathology* **2002**,
830 *160* (1), 131–139. [https://doi.org/10.1016/S0002-9440\(10\)64357-X](https://doi.org/10.1016/S0002-9440(10)64357-X).
- 831 (25) Huber, T. B.; Kottgen, M.; Schilling, B.; Walz, G.; Benzing, T. Interaction with Podocin Facilitates
832 Nephtrin Signaling. *J Biol Chem* **2001**, *276* (45), 41543–41546.
833 <https://doi.org/10.1074/jbc.C100452200>.
- 834 (26) Sellin, L.; Huber, T. B.; Gerke, P.; Quack, I.; Pavenstädt, H.; Walz, G. NEPH1 Defines a Novel Family
835 of Podocin Interacting Proteins. *FASEB J* **2003**, *17* (1), 115–117. <https://doi.org/10.1096/fj.02-0242fje>.
- 836 (27) Schwarz, K.; Simons, M.; Reiser, J.; Saleem, M. A.; Faul, C.; Kriz, W.; Shaw, A. S.; Holzman, L. B.;
837 Mundel, P. Podocin, a Raft-Associated Component of the Glomerular Slit Diaphragm, Interacts with
838 CD2AP and Nephtrin. *J. Clin. Invest.* **2001**, *108* (11), 1621–1629.
839 <https://doi.org/10.1172/JCI200112849>.
- 840 (28) Schurek, E.-M.; Völker, L. A.; Tax, J.; Lamkemeyer, T.; Rinschen, M. M.; Ungrue, D.; Kratz, J. E.;
841 Sirianant, L.; Kunzelmann, K.; Chalfie, M.; Schermer, B.; Benzing, T.; Höhne, M. A Disease-Causing
842 Mutation Illuminates the Protein Membrane Topology of the Kidney-Expressed Prohibitin Homology

- 843 (PHB) Domain Protein Podocin. *Journal of Biological Chemistry* **2014**, 289 (16), 11262–11271.
844 <https://doi.org/10.1074/jbc.M113.521773>.
- 845 (29) Roux, K. J.; Kim, D. I.; Raida, M.; Burke, B. A Promiscuous Biotin Ligase Fusion Protein Identifies
846 Proximal and Interacting Proteins in Mammalian Cells. *Journal of Cell Biology* **2012**, 196 (6), 801–
847 810. <https://doi.org/10.1083/jcb.201112098>.
- 848 (30) Kim, D. I.; Jensen, S. C.; Noble, K. A.; Kc, B.; Roux, K. H.; Motamedchaboki, K.; Roux, K. J. An
849 Improved Smaller Biotin Ligase for BioID Proximity Labeling. *Mol Biol Cell* **2016**, 27 (8), 1188–1196.
850 <https://doi.org/10.1091/mbc.E15-12-0844>.
- 851 (31) Mick, D. U.; Rodrigues, R. B.; Leib, R. D.; Adams, C. M.; Chien, A. S.; Gygi, S. P.; Nachury, M. V.
852 Proteomics of Primary Cilia by Proximity Labeling. *Developmental Cell* **2015**, 35 (4), 497–512.
853 <https://doi.org/10.1016/j.devcel.2015.10.015>.
- 854 (32) Firat-Karalar, E. N.; Rauniyar, N.; Yates, J. R.; Stearns, T. Proximity Interactions among Centrosome
855 Components Identify Regulators of Centriole Duplication. *Curr Biol* **2014**, 24 (6), 664–670.
856 <https://doi.org/10.1016/j.cub.2014.01.067>.
- 857 (33) Rudolph, F.; Fink, C.; Hüttemeister, J.; Kirchner, M.; Radke, M. H.; Lopez Carballo, J.; Wagner, E.;
858 Kohl, T.; Lehnart, S. E.; Mertins, P.; Gotthardt, M. Deconstructing Sarcomeric Structure–Function
859 Relations in Titin-BioID Knock-in Mice. *Nat Commun* **2020**, 11 (1), 3133.
860 <https://doi.org/10.1038/s41467-020-16929-8>.
- 861 (34) Uezu, A.; Kanak, D. J.; Bradshaw, T. W. A.; Soderblom, E. J.; Catavero, C. M.; Burette, A. C.;
862 Weinberg, R. J.; Soderling, S. H. Identification of an Elaborate Complex Mediating Postsynaptic
863 Inhibition. *Science* **2016**, 353 (6304), 1123–1129. <https://doi.org/10.1126/science.aag0821>.
- 864 (35) Roselli, S.; Heidet, L.; Sich, M.; Henger, A.; Kretzler, M.; Gubler, M.-C.; Antignac, C. Early
865 Glomerular Filtration Defect and Severe Renal Disease in Podocin-Deficient Mice. *Molecular and*
866 *Cellular Biology* **2004**, 24 (2), 550–560. <https://doi.org/10.1128/MCB.24.2.550-560.2004>.
- 867 (36) Sears, R. M.; May, D. G.; Roux, K. J. BioID as a Tool for Protein-Proximity Labeling in Living Cells.
868 *Methods Mol Biol* **2019**, 2012, 299–313. https://doi.org/10.1007/978-1-4939-9546-2_15.
- 869 (37) Asanuma, K.; Campbell, K. N.; Kim, K.; Faul, C.; Mundel, P. Nuclear Relocation of the Nephron and
870 CD2AP-Binding Protein Dendrin Promotes Apoptosis of Podocytes. *Proc. Natl. Acad. Sci. U.S.A.* **2007**,
871 104 (24), 10134–10139. <https://doi.org/10.1073/pnas.0700917104>.
- 872 (38) Ebnet, K.; Suzuki, A.; Ohno, S.; Vestweber, D. Junctional Adhesion Molecules (JAMs): More
873 Molecules with Dual Functions? *Journal of Cell Science* **2004**, 117 (1), 19–29.
874 <https://doi.org/10.1242/jcs.00930>.
- 875 (39) Gerlach, G. F.; Wingert, R. A. Zebrafish Pronephros Tubulogenesis and Epithelial Identity
876 Maintenance Are Reliant on the Polarity Proteins Prkc Iota and Zeta. *Developmental Biology* **2014**, 396
877 (2), 183–200. <https://doi.org/10.1016/j.ydbio.2014.08.038>.
- 878 (40) Seeger, T. S.; Frank, D.; Rohr, C.; Will, R.; Just, S.; Grund, C.; Lyon, R.; Luedde, M.; Koegl, M.;
879 Sheikh, F.; Rottbauer, W.; Franke, W. W.; Katus, H. A.; Olson, E. N.; Frey, N. Myozap, a Novel
880 Intercalated Disc Protein, Activates Serum Response Factor-Dependent Signaling and Is Required to
881 Maintain Cardiac Function in Vivo. *Circ Res* **2010**, 106 (5), 880–890.
882 <https://doi.org/10.1161/CIRCRESAHA.109.213256>.
- 883 (41) Pieperhoff, S.; Rickelt, S.; Heid, H.; Claycomb, W. C.; Zimbelmann, R.; Kuhn, C.; Winter-
884 Simanowski, S.; Kuhn, C.; Frey, N.; Franke, W. W. The Plaque Protein Myozap Identified as a Novel
885 Major Component of Adhering Junctions in Endothelia of the Blood and the Lymph Vascular Systems.
886 *Journal of Cellular and Molecular Medicine* **2012**, 16 (8), 1709–1719. <https://doi.org/10.1111/j.1582-4934.2011.01463.x>.
- 888 (42) Ho, H.-Y. H.; Rohatgi, R.; Lebensohn, A. M.; Le Ma; Li, J.; Gygi, S. P.; Kirschner, M. W. Toca-1
889 Mediates Cdc42-Dependent Actin Nucleation by Activating the N-WASP-WIP Complex. *Cell* **2004**,
890 118 (2), 203–216. <https://doi.org/10.1016/j.cell.2004.06.027>.
- 891 (43) Van Itallie, C. M.; Tietgens, A. J.; Krystofiak, E.; Kachar, B.; Anderson, J. M. A Complex of ZO-1 and
892 the BAR-Domain Protein TOCA-1 Regulates Actin Assembly at the Tight Junction. *MBoC* **2015**, 26
893 (15), 2769–2787. <https://doi.org/10.1091/mbc.E15-04-0232>.

- 894 (44) Wu, H.; Malone, A. F.; Donnelly, E. L.; Kirita, Y.; Uchimura, K.; Ramakrishnan, S. M.; Gaut, J. P.;
895 Humphreys, B. D. Single-Cell Transcriptomics of a Human Kidney Allograft Biopsy Specimen Defines
896 a Diverse Inflammatory Response. *JASN* **2018**, *29* (8), 2069–2080.
897 <https://doi.org/10.1681/ASN.2018020125>.
- 898 (45) Lu, Y.; Ye, Y.; Bao, W.; Yang, Q.; Wang, J.; Liu, Z.; Shi, S. Genome-Wide Identification of Genes
899 Essential for Podocyte Cytoskeletons Based on Single-Cell RNA Sequencing. *Kidney International*
900 **2017**, *92* (5), 1119–1129. <https://doi.org/10.1016/j.kint.2017.04.022>.
- 901 (46) Higashi, T.; Tokuda, S.; Kitajiri, S.; Masuda, S.; Nakamura, H.; Oda, Y.; Furuse, M. Analysis of the
902 “angulin” Proteins LSR, ILDR1 and ILDR2--Tricellulin Recruitment, Epithelial Barrier Function and
903 Implication in Deafness Pathogenesis. *J Cell Sci* **2013**, *126* (Pt 4), 966–977.
904 <https://doi.org/10.1242/jcs.116442>.
- 905 (47) Rodewald, R.; Karnovsky, M. J. POROUS SUBSTRUCTURE OF THE GLOMERULAR SLIT
906 DIAPHRAGM IN THE RAT AND MOUSE. *Journal of Cell Biology* **1974**, *60* (2), 423–433.
907 <https://doi.org/10.1083/jcb.60.2.423>.
- 908 (48) Karnovsky, M.; Ryan, G. Substructure of the Glomerular Slit Diaphragm in Freeze-Fractured Normal
909 Rat Kidney. *Journal of Cell Biology* **1975**, *65* (1), 233–236. <https://doi.org/10.1083/jcb.65.1.233>.
- 910 (49) Kopp, J. B.; Anders, H.-J.; Susztak, K.; Podestà, M. A.; Remuzzi, G.; Hildebrandt, F.; Romagnani, P.
911 Podocytopathies. *Nat Rev Dis Primers* **2020**, *6* (1), 68. <https://doi.org/10.1038/s41572-020-0196-7>.
- 912 (50) Branon, T. C.; Bosch, J. A.; Sanchez, A. D.; Udeshi, N. D.; Svinkina, T.; Carr, S. A.; Feldman, J. L.;
913 Perrimon, N.; Ting, A. Y. Efficient Proximity Labeling in Living Cells and Organisms with TurboID.
914 *Nat Biotechnol* **2018**, *36* (9), 880–887. <https://doi.org/10.1038/nbt.4201>.
- 915 (51) May, D. G.; Scott, K. L.; Campos, A. R.; Roux, K. J. Comparative Application of BioID and TurboID
916 for Protein-Proximity Biotinylation. *Cells* **2020**, *9* (5), 1070. <https://doi.org/10.3390/cells9051070>.
- 917 (52) Wu, H.; Malone, A. F.; Donnelly, E. L.; Kirita, Y.; Uchimura, K.; Ramakrishnan, S. M.; Gaut, J. P.;
918 Humphreys, B. D. Single-Cell Transcriptomics of a Human Kidney Allograft Biopsy Specimen Defines
919 a Diverse Inflammatory Response. *JASN* **2018**, *29* (8), 2069–2080.
920 <https://doi.org/10.1681/ASN.2018020125>.
- 921 (53) Thisse, B., Thisse, C. (2004) Fast Release Clones: A High Throughput Expression Analysis. ZFIN
922 Direct Data Submission. . (<Http://Zfin.Org>).
- 923 (54) McKee, R.; Gerlach, G. F.; Jou, J.; Cheng, C. N.; Wingert, R. A. Temporal and Spatial Expression of
924 Tight Junction Genes during Zebrafish Pronephros Development. *Gene Expr Patterns* **2014**, *16* (2),
925 104–113. <https://doi.org/10.1016/j.gep.2014.11.001>.
- 926 (55) Podojil, J. R.; Hecht, I.; Chiang, M.-Y.; Vaknin, I.; Barbiro, I.; Novik, A.; Neria, E.; Rotman, G.;
927 Miller, S. D. ILDR2-Fc Is a Novel Regulator of Immune Homeostasis and Inducer of Antigen-Specific
928 Immune Tolerance. *J Immunol* **2018**, *200* (6), 2013–2024. <https://doi.org/10.4049/jimmunol.1700326>.
- 929 (56) Hecht, I.; Toporik, A.; Podojil, J. R.; Vaknin, I.; Cojocaru, G.; Oren, A.; Aizman, E.; Liang, S. C.;
930 Leung, L.; Dicken, Y.; Novik, A.; Marbach-Bar, N.; Elmesmari, A.; Tange, C.; Gilmour, A.; McIntyre,
931 D.; Kurowska-Stolarska, M.; McNamee, K.; Leitner, J.; Greenwald, S.; Dassa, L.; Levine, Z.;
932 Steinberger, P.; Williams, R. O.; Miller, S. D.; McInnes, I. B.; Neria, E.; Rotman, G. ILDR2 Is a Novel
933 B7-like Protein That Negatively Regulates T Cell Responses. *J Immunol* **2018**, *200* (6), 2025–2037.
934 <https://doi.org/10.4049/jimmunol.1700325>.
- 935 (57) Huetter, J.; Gritzan, U.; Gutcher, I.; Doecke, W.-D.; Luetke-Eversloh, M. V.; Golfier, S.; Roider, H. G.;
936 Frisk, A.-L.; Hunter, J.; Pow, A.; Drake, A.; Levine, Z.; Levy, O.; Azulay, M.; Barbiro, I.; Cojocaru,
937 G.; Vaknin, I.; Kreft, B.; Roese, L. Characterization of BAY 1905254, an Immune Checkpoint Inhibitor
938 Targeting the Immunoglobulin-Like Domain Containing Receptor 2 (ILDR2). *Cancer Immunol Res*
939 **2020**, *8* (7), 895–911. <https://doi.org/10.1158/2326-6066.CIR-19-0321>.
- 940 (58) Wu, H.; Kirita, Y.; Donnelly, E. L.; Humphreys, B. D. Advantages of Single-Nucleus over Single-Cell
941 RNA Sequencing of Adult Kidney: Rare Cell Types and Novel Cell States Revealed in Fibrosis. *JASN*
942 **2019**, *30* (1), 23–32. <https://doi.org/10.1681/ASN.2018090912>.
- 943 (59) Ettou, S.; Jung, Y. L.; Miyoshi, T.; Jain, D.; Hiratsuka, K.; Schumacher, V.; Taglienti, M. E.; Morizane,
944 R.; Park, P. J.; Kreidberg, J. A. Epigenetic Transcriptional Reprogramming by WT1 Mediates a Repair

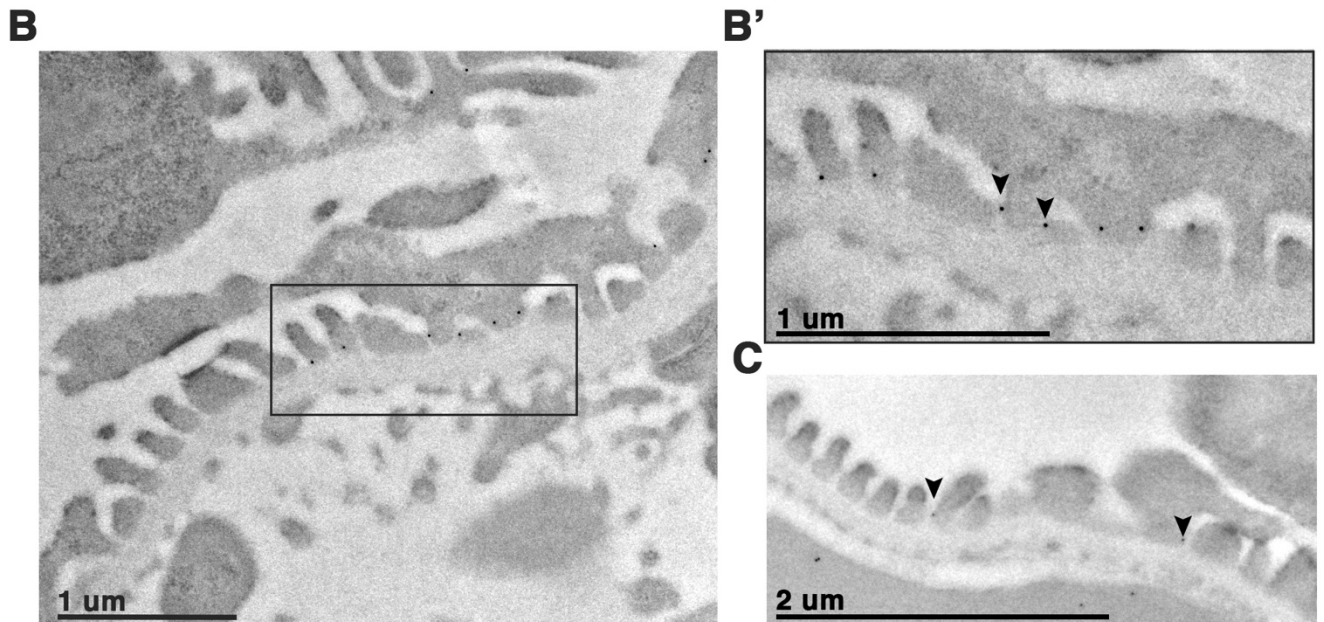
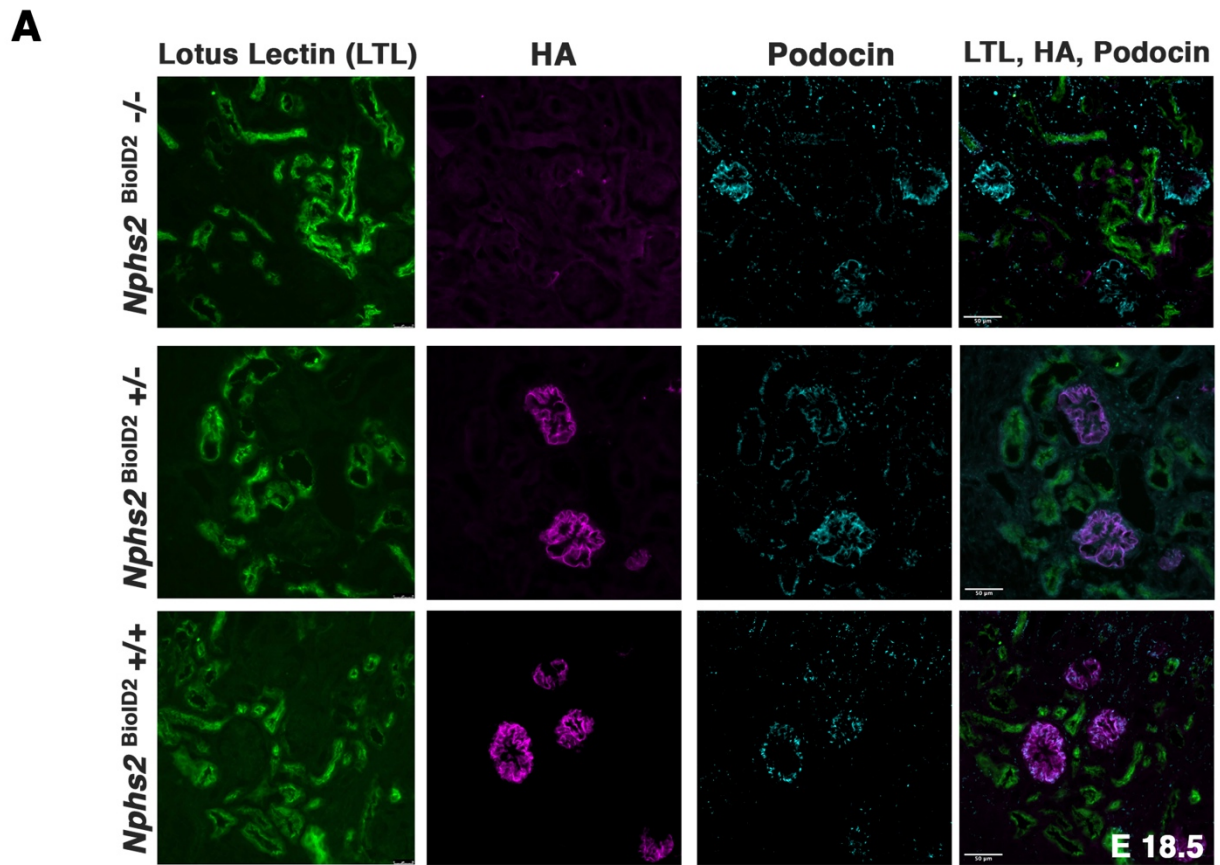
- 945 Response during Podocyte Injury. *Sci. Adv.* **2020**, *6* (30), eabb5460.
946 <https://doi.org/10.1126/sciadv.abb5460>.
- 947 (60) Go, C. D.; Knight, J. D. R.; Rajasekharan, A.; Rathod, B.; Hesketh, G. G.; Abe, K. T.; Youn, J.-Y.;
948 Samavarchi-Tehrani, P.; Zhang, H.; Zhu, L. Y.; Popiel, E.; Lambert, J.-P.; Coyaud, É.; Cheung, S. W.
949 T.; Rajendran, D.; Wong, C. J.; Antonicka, H.; Pelletier, L.; Palazzo, A. F.; Shoubridge, E. A.; Raught,
950 B.; Gingras, A.-C. A Proximity-Dependent Biotinylation Map of a Human Cell. *Nature* **2021**, *595*
951 (7865), 120–124. <https://doi.org/10.1038/s41586-021-03592-2>.
- 952 (61) Yu, H. H.; Zallen, J. A. Abl and Canoe/Afadin Mediate Mechanotransduction at Tricellular Junctions.
953 *Science* **2020**, *370* (6520), eaba5528. <https://doi.org/10.1126/science.aba5528>.
- 954 (62) Cox, J.; Mann, M. MaxQuant Enables High Peptide Identification Rates, Individualized p.p.b.-Range
955 Mass Accuracies and Proteome-Wide Protein Quantification. *Nat Biotechnol* **2008**, *26* (12), 1367–1372.
956 <https://doi.org/10.1038/nbt.1511>.
- 957 (63) Brademan, D. R.; Miller, I. J.; Kwiecien, N. W.; Pagliarini, D. J.; Westphall, M. S.; Coon, J. J.;
958 Shishkova, E. Argonaut: A Web Platform for Collaborative Multi-Omic Data Visualization and
959 Exploration. *Patterns* **2020**, *1* (7), 100122. <https://doi.org/10.1016/j.patter.2020.100122>.
- 960 (64) Reynolds, E. S. THE USE OF LEAD CITRATE AT HIGH PH AS AN ELECTRON-OPAQUE STAIN
961 IN ELECTRON MICROSCOPY. *Journal of Cell Biology* **1963**, *17* (1), 208–212.
962 <https://doi.org/10.1083/jcb.17.1.208>.
- 963 (65) Hobot, J. A.; Newman, G. R. Immunomicroscopy: Resin Techniques and on-Section Labelling with
964 Immunocolloidal Gold or Immunoperoxidase--Planning a Protocol. *Scanning Microsc* **1996**, *10* (1),
965 121–143; discussion 143-145.
- 966 (66) Liu, Y.; Nie, H.; Liu, C.; Zhai, X.; Sang, Q.; Wang, Y.; Shi, D.; Wang, L.; Xu, Z. Angulin Proteins
967 ILDR1 and ILDR2 Regulate Alternative Pre-mRNA Splicing through Binding to Splicing Factors
968 TRA2A, TRA2B, or SRSF1. *Sci Rep* **2017**, *7* (1), 7466. <https://doi.org/10.1038/s41598-017-07530-z>.
969

Figure 1



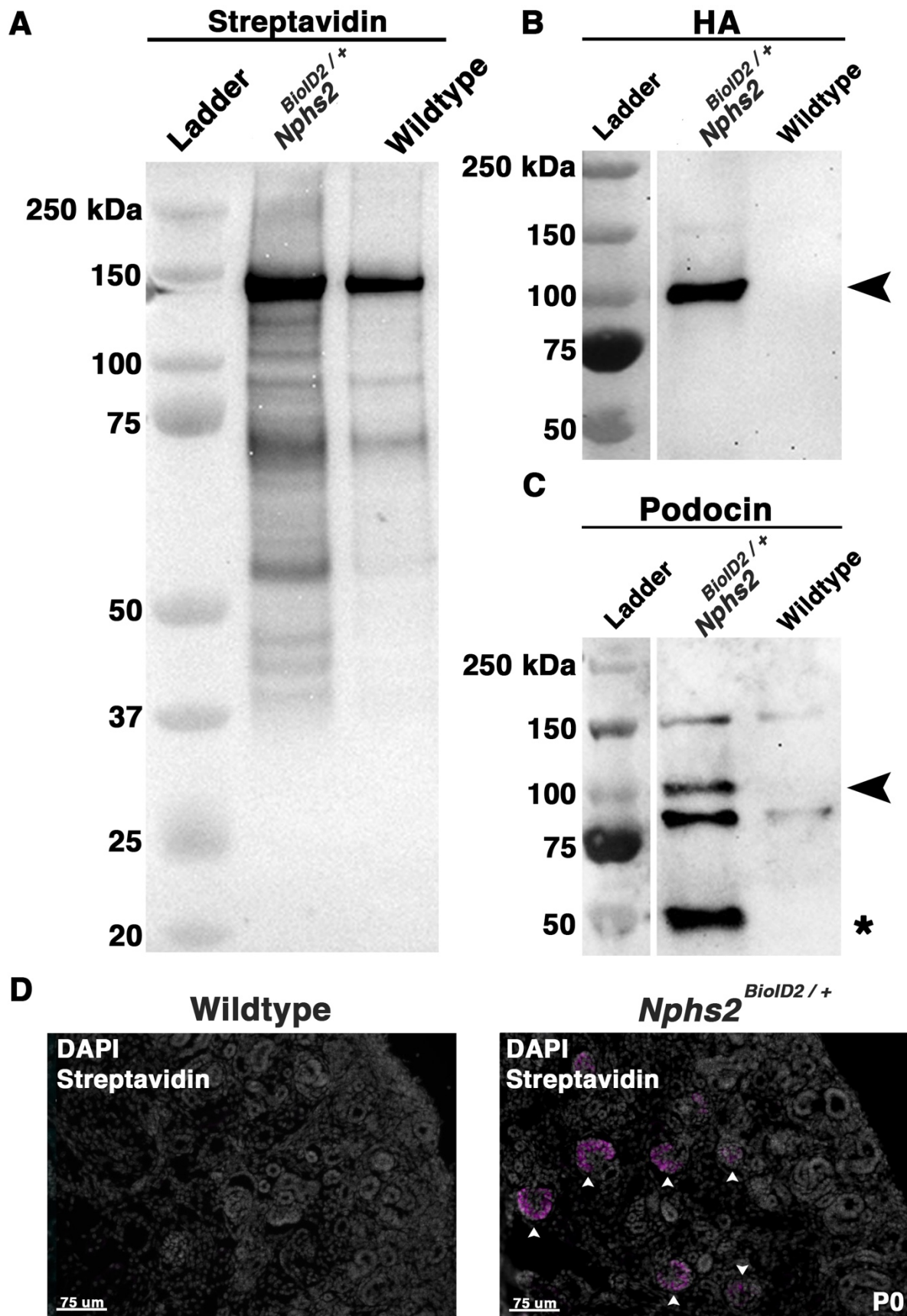
972 **Figure 1. Generation of a knock-in *Nphs2*^{Bioid2} mouse line via CRISPR/Cas9 genome editing**
973 **of the *Nphs2* locus. (A)** Schematic of the CRISPR/Cas9 genome editing strategy utilized to
974 generate the *Nphs2*^{Bioid2} mouse line. A small guide RNA (sgRNA) targeting the stop codon in exon
975 8 of *Nphs2* (purple arrowhead) was combined with a donor vector containing the knock-in cassette
976 (zoom view) to induce homologous recombination and integrate the Bioid2 moiety containing a
977 13x Glycine/Serine (G/S) linker, biotin ligase, and HA tag into the *Nphs2* locus. **(B)** Genotyping
978 strategy (top panel) to identify genotype of mice as wildtype (single band at 264 base pairs (bp)),
979 heterozygous (two bands; one at wildtype size of 264 bp and a second that amplifies the Bioid2
980 linker region giving a band at 480 bp), or homozygous (single band at the 480 bp). **(C)** Genotyping
981 of 73 embryos at E18.5-P0, verify an approximate Mendelian ratio of genotypes being recovered
982 (25:50:25). **(D)** IF analysis of 8–10-week-old adult mice injected with biotin illustrate an enrichment
983 of streptavidin detected within the glomerulus of *Nphs2*^{Bioid2} mice and absence of streptavidin
984 signal in control age matched C57BL/6J littermate mice. The HA signal from the Bioid2 moiety
985 closely overlaps with streptavidin, observed as white overlap in the merged image. Wilms Tumor
986 (WT1) is utilized as a podocyte marker to delineate the glomerular boundaries. Scale bar: 50 μ m
987
988

Figure 2.



990 **Figure 2. *Nphs2*^{BioID2} animals present normal kidney morphology with podocin-BioID**
991 **localized to podocytes and specifically the slit diaphragm. (A)** E18.5 littermates of wildtype,
992 heterozygous (*Nphs2*^{BioID2/+}), and homozygous (*Nphs2*^{BioID2/BioID2}) animals were analyzed for gross
993 kidney morphology and localization of podocin-BioID. The proximal tubule marker lotus lectin (LTL,
994 green) show normal tubule architecture without observation of nephron tubule dilation in
995 heterozygous (*Nphs2*^{BioID2/+}), and homozygous (*Nphs2*^{BioID2/BioID2}) animals. The HA tag (magenta)
996 which is part of the BioID2 moiety was observed to tightly overlap with podocin (cyan) specifically
997 in the glomerulus. The relative size and number of glomeruli was unchanged between control,
998 heterozygous, and homozygous animals. Further, the HA signal was not identified outside of the
999 glomeruli. Scale bar 50 μm **(B)** *Nphs2*^{BioID2/+} localizes to the podocyte slit diaphragm. Utilizing
000 transmission electron microscopy (TEM) and immunogold labeling of 4-week-old murine kidney
001 samples, we detect the anti-HA signal as punctate dots strung just above the GBM adjacent to the
002 podocyte foot process within electron dense regions where the slit diaphragm bridges neighboring
003 foot processes. **(B')** Magnified view of boxed region from panel (B) depicting podocyte foot
004 processes and the electron dense regions between them where the HA signal localizes as dark
005 spherical dots from immunogold labeling, denoted with arrowheads. Scale bar 1 μm **(C)** Wildtype
006 littermates were immunogold labeled for podocin and similarly display localization of podocin at
007 electron dense regions between podocyte foot processes, highlighted with arrowheads. Scale bar
008 2 μm.
009
010
011
012
013
014
015
016
017
018
019
020
021
022
023
024
025
026
027
028
029
030
031
032
033
034
035
036
037
038
039

Figure 3



042 **Figure 3. Biotin administered *Nphs2*^{BioID2/+} mice present an enrichment of biotinylated**
043 **proteins specifically within glomeruli. (A)** A significant enrichment of streptavidin labeled,
044 biotinylated, proteins are observed across the entire molecular weight spectrum in *Nphs2*^{BioID2/+}
045 protein lysates compared to wildtype control littermates, injected with biotin. Streptavidin bead
046 purified lysates were subjected to protein separation and probed for streptavidin. Wildtype age
047 matched, 8–10-week-old, littermate controls present few streptavidin conjugated bands,
048 presumably endogenous metabolic carboxylases. However, *Nphs2*^{BioID2/+} lysates exhibit numerous
049 specific biotinylated protein bands across the entire molecular weight spectrum. **(B)** *Nphs2*^{BioID2/+}
050 lysates blotted with an anti-HA antibody present robust and specific detection of the HA signal only
051 within the *Nphs2*^{BioID2/+} sample, indicative of lysate purity. The HA signal is evident at approximately
052 100 kDa (arrowhead) in *Nphs2*^{BioID2/+} lysates. **(C)** *Nphs2*^{BioID2/+} samples probed for podocin show
053 two specific bands for both BioID2-tagged podocin and endogenous podocin. Adult 8-10-week-old
054 *Nphs2*^{BioID2/+} mice blotted for podocin present a 50kDa band for the endogenous unmodified
055 podocin protein, marked with an asterisk (*) and a second larger band at approximately 100 kDa
056 for the HA tagged podocin-BioID of *Nphs2*^{BioID2/+} mice (arrowhead). **(D)** P0 pups collected from
057 pregnant dams injected with 5 mg/kg of biotin every day from E11.5 to E18.5, and without injection
058 of newborn pups, manifest strong streptavidin detection within glomeruli. Immunofluorescence
059 analysis reveals an enrichment of streptavidin signal (magenta) specifically within the glomeruli
060 (arrowheads) of *Nphs2*^{BioID2/+} kidneys compared to wildtype. Scale bar 75 μ m.

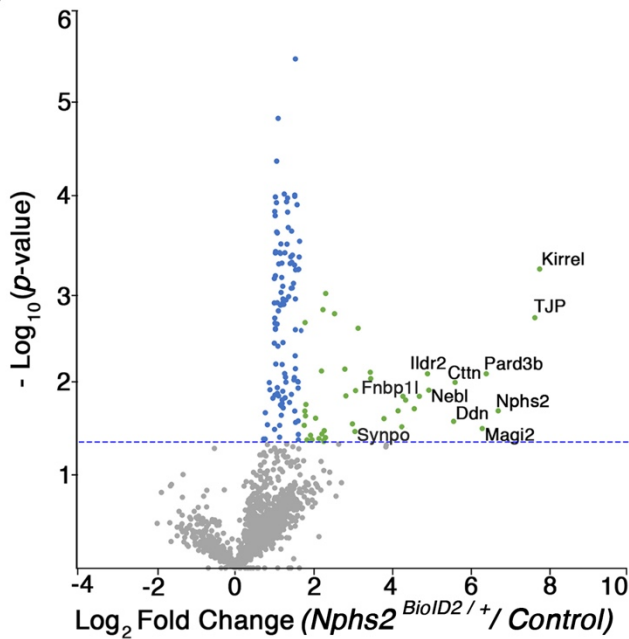
061
062
063
064
065
066
067
068
069
070
071
072
073
074

Figure 4.

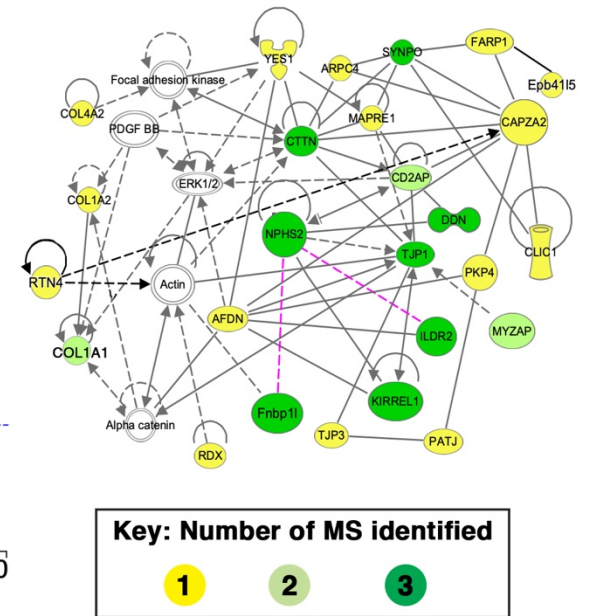
A

Gene Symbol	Protein Names	p-Value	Log ₂ Fold Change
<i>Kirrel</i>	Kin of IRRE-like protein 1	0.0006	7.75
<i>Tjp1</i>	Tight junction protein ZO-1	0.002	7.63
<i>Nphs2</i>	Podocin	0.019	6.70
<i>Pard3b</i>	Partitioning defective 3 homolog B	0.008	6.39
<i>Magi2</i>	Membrane-associated guanylate kinase, WW and PDZ domain-containing protein 2	0.018	6.29
<i>Cttn</i>	Src substrate cactinin	0.001	5.60
<i>Ddn</i>	Dendrin	0.003	5.56
<i>Nebi</i>	LIM zinc-binding domain-containing Nebulette	0.010	4.93
<i>Ildr2</i>	Immunoglobulin-like domain-containing receptor 2	0.007	4.90
<i>Fnbp1l</i>	Formin-binding protein 1-like	0.014	4.27
<i>Synpo</i>	Synaptopodin	0.047	2.90
<i>Tjp2</i>	Tight junction protein ZO-2	0.014	4.71
<i>Myzap</i>	Myocardial zonula adherens protein	0.009	3.45
<i>Cd2ap</i>	CD2-associated protein	0.020	3.18
<i>Col1a1</i>	Collagen alpha-1(I) chain	0.007	2.05
<i>Aif1l</i>	Allograft inflammatory factor 1-like	0.014	1.86
<i>Tns2</i>	Tensin-2	0.022	1.75

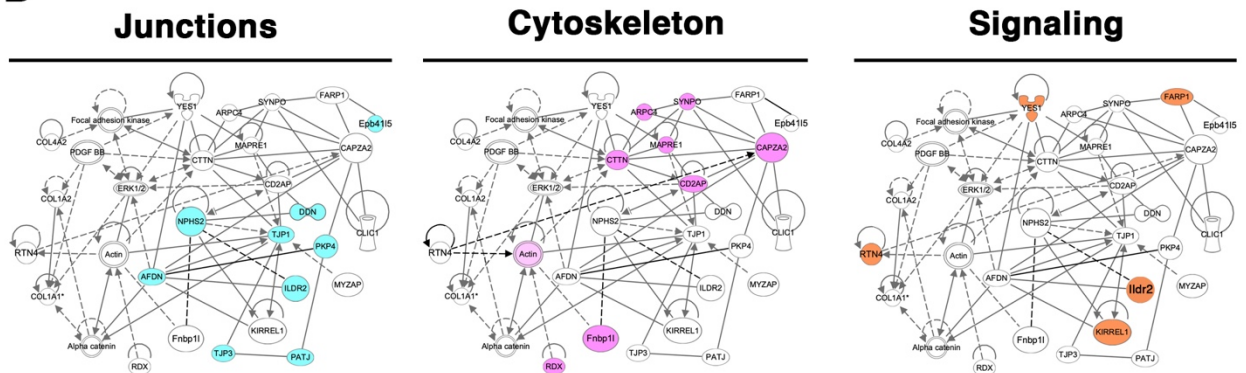
B



C



D



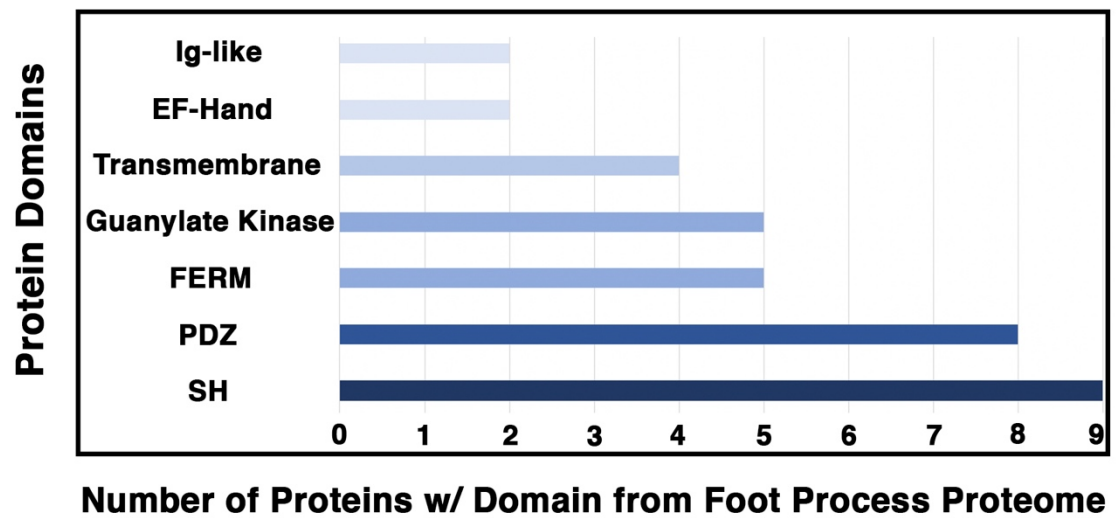
077 **Figure 4. Proteomics profiling of the podocyte foot process identifies documented slit**
078 **diaphragm components and novel candidates with unexplored podocyte function. (A)** Three
079 separate MS analyses were combined, and the average Log₂ fold change and respective *p*-values
080 were averaged to produce a list of the top foot process proteins. The top 11 proteins were
081 identified across all three MS profiles. Six additional proteins were identified across two of the
082 three MS analyses, denoted following the thick black bar. Podocin was a top protein identified and
083 known to oligomerize, indicating our MS proteomic profiling was effective. Additionally, many of the
084 top proteins uncovered, *i.e.*, Kirrel, Dnd, Tjp1/2, Magi2, Pard3, Synpo, and Cd2ap are documented
085 podocyte slit diaphragm components. **(B)** A volcano plot depicting approximately 1400 proteins
086 identified across all three MS analyses. Green dots represent the 40 proteins identified across
087 three separate MS profiles as having a Log₂ fold change ≥ 1.7 , and *p*-value ≤ 0.05 , blue dots
088 denote all proteins identified to have a significant *p*-value ≤ 0.05 , and grey dots are proteins with a
089 *p*-value ≥ 0.05 . The top 11 proteins consistently uncovered across all MS analyses are embedded
090 with gene symbols in the plot. The blue dotted line represents a *p*-value ≤ 0.05 . **(C)** Network
091 topology was generated utilizing *Qiagen Ingenuity Pathway Analysis* (IPA) on the top 54 proteins
092 from our cumulative proteomic profiles. IPA produces a proposed web of relationships from
093 published literature with most of our top proteins represented, (11 of 17), with documented
094 connections to other foot process and slit diaphragm components. The color intensities of each
095 protein (yellow to green) represent the number of MS analyses from which each protein was
096 identified. Darkest green shade=all three MS analyses, lighter green shade=two of three MS
097 analyses, and yellow=a single MS analysis. Dotted lines and unshaded proteins represent
098 predicted interactions / interactors from IPA analysis, respectively. Magenta lines are novel
099 proteins identified in this study to be present within the podocyte foot process. **(D)** Dissecting the
100 IPA network, identifies three central nodes representing junctions, cytoskeleton, and signaling.
101 Each respective node is color coded with junctions in cyan, cytoskeleton in magenta, and signaling
102 in orange. These computational network topologies and nodes tightly align with podocyte structure
103 and function.
104

Figure 5.

A

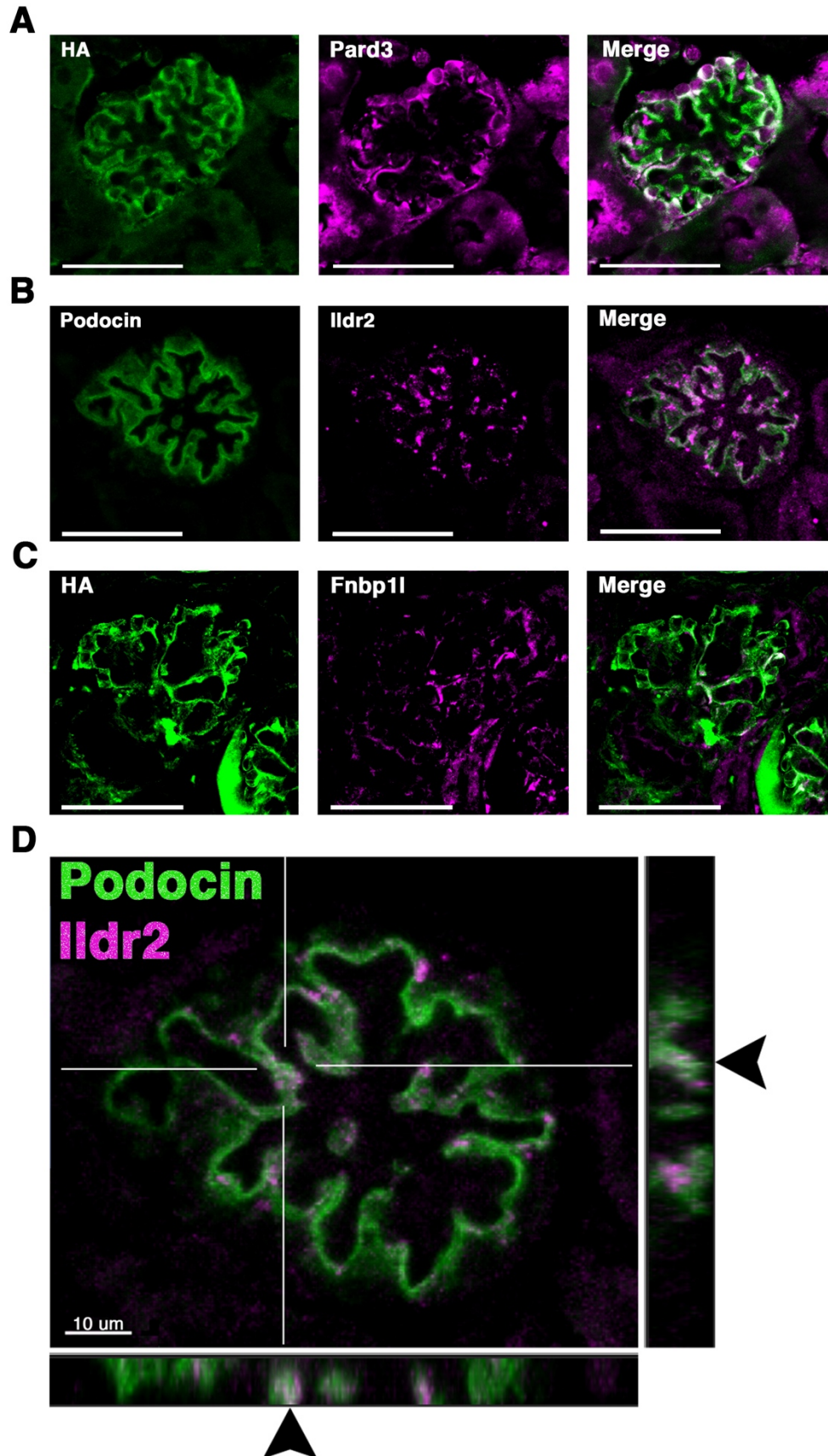
Gene Ontology (GO) Category	Cluster	Enrichment Score	Counts	p-Value
Molecular Function (MF)	Cytoskeletal Protein Binding	4.53	12	2.20×10^{-7}
	Actin Binding		6	7.80×10^{-5}
Cellular Component (CC)	Cell-Cell Junction	4.42	12	7.70×10^{-8}
	Adherens Junction		10	7.90×10^{-6}
Biological Process (BP)	Cytoskeleton Organization	2.61	14	3.20×10^{-7}
	Actin Filament-Based Process		12	8.70×10^{-8}

B



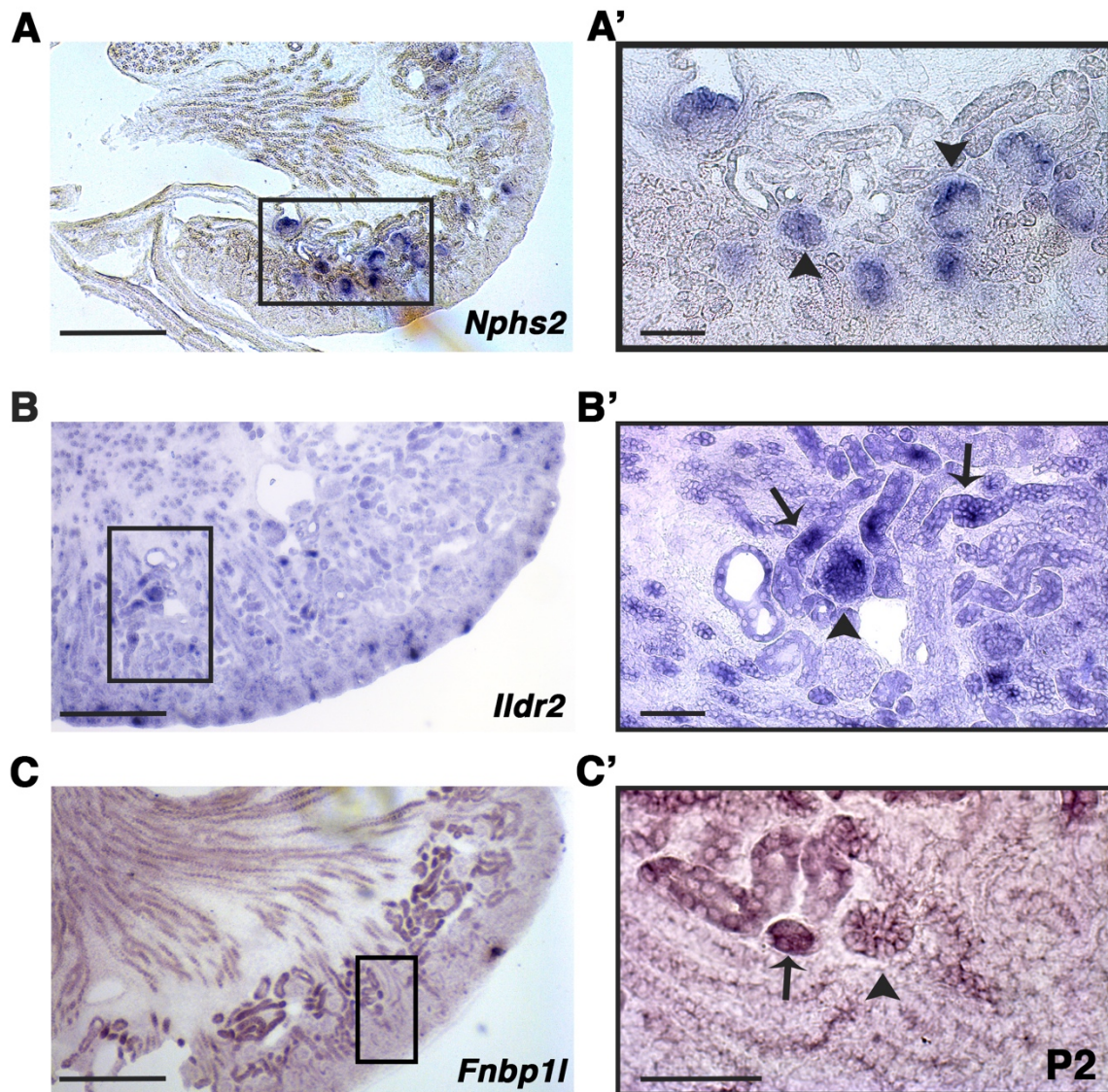
106 **Figure 5. Analysis of the podocyte foot process proteome identifies the cytoskeleton, cell-**
107 **cell junctions, and actin-based processes as the top GO categories with respective protein**
108 **domains that align with these functions.** The Database for Annotation, Visualization, and
109 Integrative Discovery (DAVID) was utilized for GO clustering analysis of the top 54 proteins
110 identified to have a Log_2 fold change ≥ 1.20 , and p -value ≤ 0.05 (Supplemental Table V). **(A)**
111 Overlap in GO readout was observed across the three separate GO categories analyzed,
112 molecular function, cellular component, and biological process, with cytoskeleton, actin, and
113 cellular junctions being the top hits. The respective top clusters within each GO category are listed,
114 alongside the relative enrichment score, number of proteins, and p -values. **(B)** Protein domain
115 analysis of the top 54 podocyte foot process proteins provides evidence for protein-protein
116 interactions and likely scaffold and protein-protein complex formation. Each protein's respective
117 protein domains were binary counted for presence or absence within the proteomics profile. The
118 top seven protein domains identified from the podocyte foot process proteome consist of a Src
119 homology (SH) ($n = 9$ proteins), PSD-95, Disc large, and ZO - 1 (PDZ) ($n = 8$), 4.1 protein, Ezrin,
120 Radixin and Moesin (FERM) ($n = 5$), Guanylate Kinase ($n = 5$), Transmembrane ($n = 4$), E and F
121 helix - Hand (EF - Hand) ($n = 2$), and an Immunoglobulin - like (Ig - like) domain ($n = 2$).
122 Cumulatively, these 7 domains represent $\sim 50\%$ of the top proteins identified from the foot process
123 proteome (26 / 54).

Figure 6.



125 **Figure 6. Two novel foot process candidates, Ildr2 and Fnbp1l, localize to podocytes and**
126 **overlap with podocin in the foot process.** IF analysis of three top candidates identified from the
127 proteomics profiling, Pard3, Ildr2, and Fnbp1l, were detected within glomeruli. **(A)** Pard3
128 (magenta), a known component of the podocyte foot process, co-localizes with HA signal of
129 podocin-BioID (green) producing a white signal in overlap. **(B)** Ildr2 (magenta) displays a punctate
130 localization pattern within the glomerulus and overlaps (white) with podocin (green). **(C)** Fnbp1l
131 (magenta) co-localizes (white) with HA signal of podocin-BioID (green) in podocytes. Scale bars in
132 A-C: 50 μm **(D)** A merged image of podocin and Ildr2 through a confocal z-projection identifies
133 punctate localization and overlap (white, arrowheads) between podocin (green) and Ildr2
134 (magenta) visualized in the z-plane in the left and bottom panels. Scale bar in D 10 μm .
135

Figure 7.



137 **Figure 7. *In situ* hybridization confirms glomerular and some tubule cell expression of *Ildr2***
138 **and *Fnbp1l* in P2 kidneys.** P2 kidney sections were hybridized with antisense riboprobes against
139 *Nphs2* (podocin), *Ildr2*, and *Fnbp1l*. **(A)** *Nphs2* (purple) displays strong expression specifically in
140 glomeruli at P2. The rectangular box in **(A)** is enlarged in **(A')** to highlight expression of *Nphs2* only
141 in glomeruli, arrowheads denote example glomeruli **(B)** *Ildr2* transcripts (purple) are identified
142 within glomeruli and tubules. The rectangular box in **(B)** is enlarged in **(B')** to denote expression of
143 *Ildr2* in glomeruli, arrowhead, and in some tubules, black arrow. **(C)** *Fnbp1l* (purple) is identified in
144 both glomeruli and tubules. The block rectangular box in **(C)** is enlarged in **(C')** to denote
145 expression of *Fnbp1l* in glomeruli, arrowhead, and tubules, arrow. Scale bars in A–C: 500 μ m.
146 Scale bars in A'–C': 100 μ m.

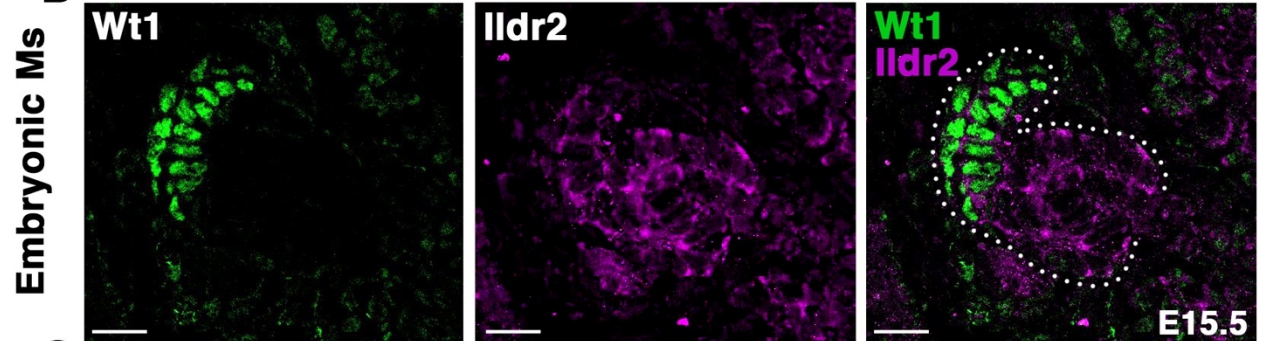
147
148
149
150
151
152

Figure 8.

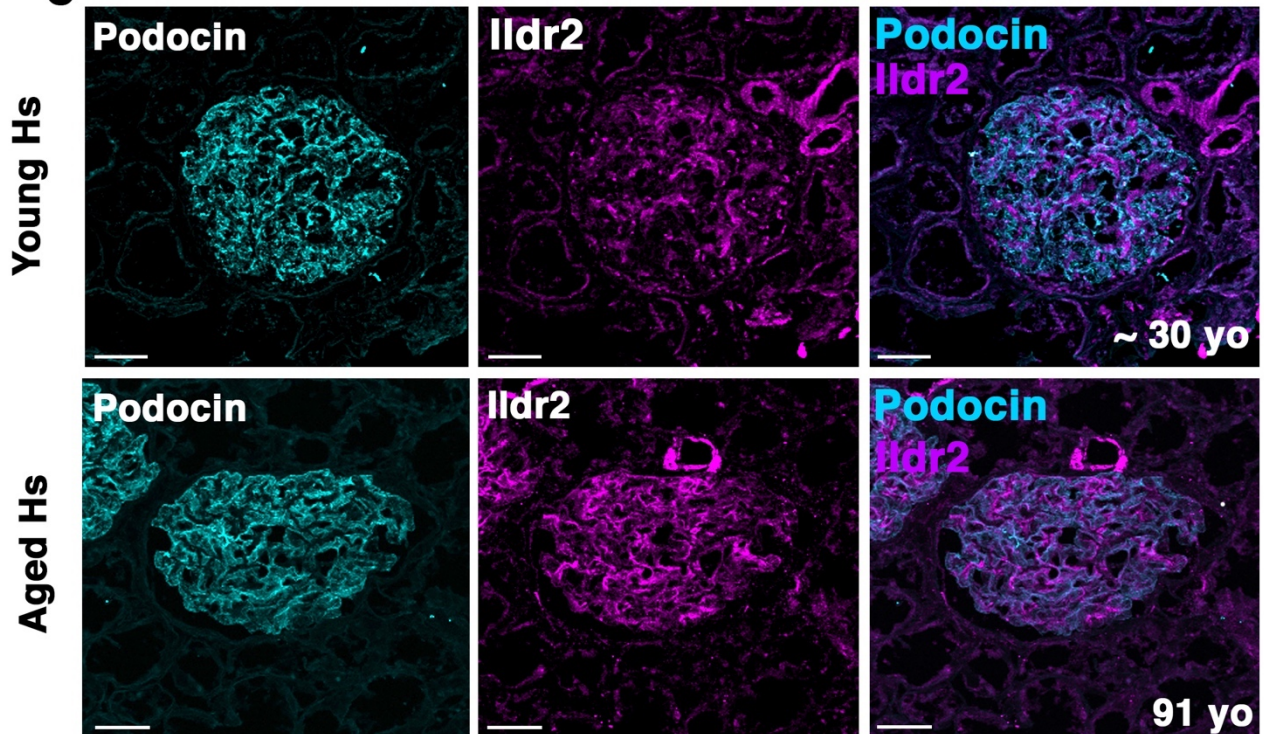
A

Gene Symbol	Protein Names	BioID (Young) vs WT Log ₂ Fold Change	BioID (Aged) vs WT Log ₂ Fold Change	p-Value
<i>Ildr2</i>	Immunoglobulin-like domain-containing receptor 2	2.76	3.53	0.001
<i>Tjp2</i>	Tight junction protein ZO-2	2.71	3.31	0.01
<i>Pkp4</i>	Plakophilin-4	2.27	2.94	0.01
<i>Nphs2</i>	Podocin	2.42	2.36	0.10
<i>Fnbp1l</i>	Formin-binding protein 1-like	3.22	2.12	0.10
<i>Tns2</i>	Tensin-2	1.30	0.36	0.10

B



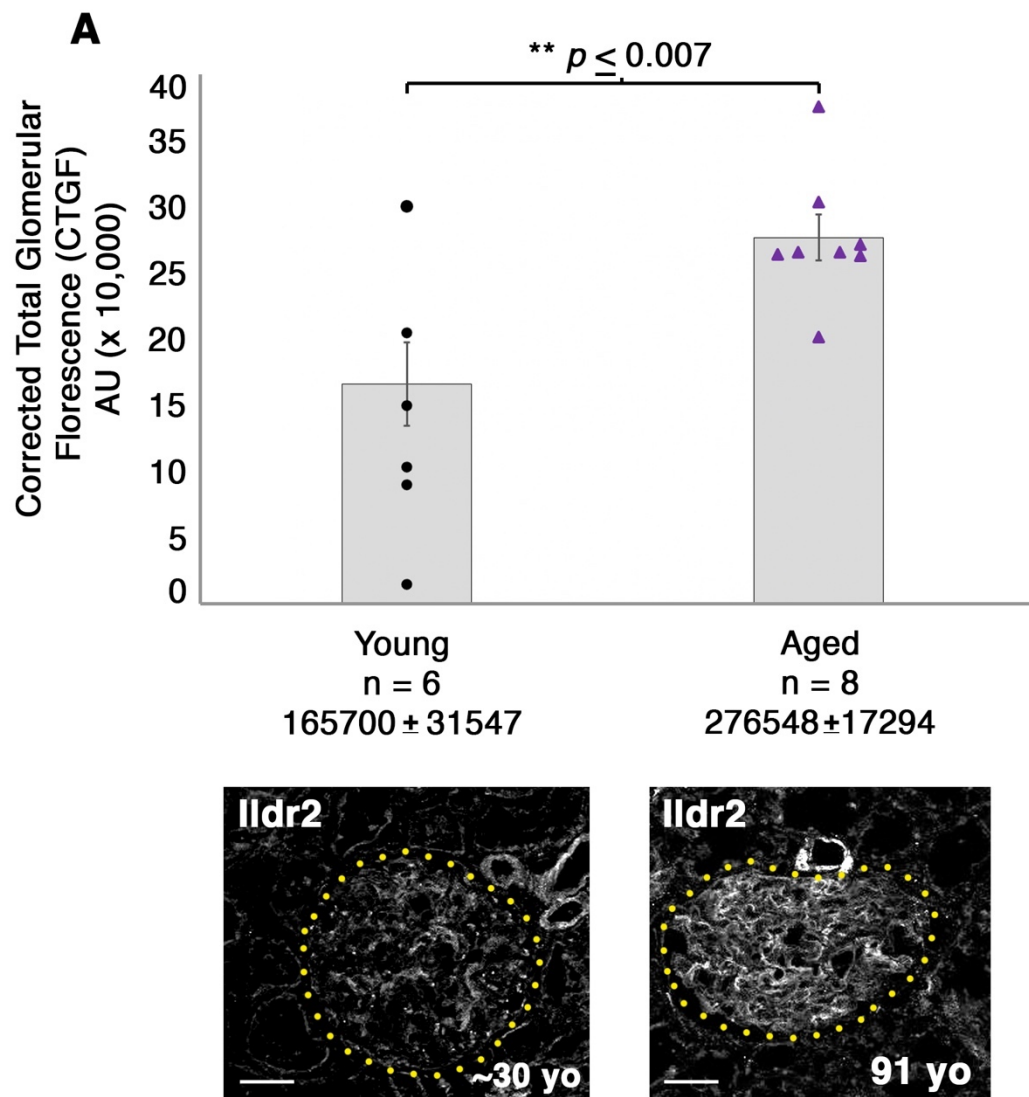
C



154 **Figure 8. Ildr2 is detected in developing nephron structures and presents increased**
155 **detection in aged mouse and human glomeruli compared to young. (A)** Proteomic profiling of
156 two aged (108 week old) male *Nphs2^{BioID2/+}* mice identifies a significant increase in Ildr2, Tjp2, and
157 Pkp4 protein levels compared to 8-10 week old *Nphs2^{BioID2/+}* mice. Table lists 6 proteins with
158 relative detection in “young” 8-10 week old *Nphs2^{BioID2/+}* male mice vs “aged” 108 week old
159 *Nphs2^{BioID2/+}* male mice. All proteins were detected with at least 2 razor unique peptides with their
160 respective *p*-values in far right column. **(B)** Ildr2 is expressed in early developing nephron
161 structures including the renal vesicle, comma, and s-shaped bodies with podocytes denoted by the
162 Wt1-positive nuclei. Ildr2 (magenta) is observed as membranous along the comma / s-shaped
163 body with some punctate foci in E15.5 mouse kidney cortex, outlined with white dots. Scale bar: 20
164 μm . **(C)** Young and aged (91 yo) human kidney tissue was probed for Ildr2 via IF. Young human
165 glomeruli display punctate foci detection of Ildr2 (magenta) similar to 8-10 week old mice.
166 However, aged (91 yo) male glomeruli evince an increase in Ildr2 detection within glomeruli.
167 Furthermore, where Ildr2 looks to be more highly detected in these aged glomeruli podocin
168 appears less detectable. Scale bar: 50 μm .

169
170
171
172
173
174
175
176
177
178
179

Figure 9



181 **Figure 9. Aged 91 yo glomeruli exhibit a significant increase in corrected total glomerular**
182 **florencence (CTGF) compared to young human glomeruli.** We observe a significant ($p \leq 0.007$)
183 increase, of approximatly 67%, in CTFG in aged human lldr2 detection compared to young human
184 tissue. CTGF was calculated by selecting the gomeruli as the ROI then measuring the total
185 florescence within the area and subtracting out the sum of the area by the average background
186 florescence, *i.e.* Total gROI florescence – (Area of glomerulus x mean of background florescence) =
187 CTGF. Two example glomeruli are displayed and outlined in yellow dots to depict the respective
188 ROI utilized to calculate CTGF. Scale bar: 50 μm .

189

190

191

192

193

194

195

196

197

Supplemental Table I.

Antidody	Dilution [IF]	Dilution [WB]	Company
Goat anti - Collagen IV	[1:500]		Sigma-Aldrich, AB769, Lot 2930544
Mouse (IgG1) anti - Myozap	supernatant (straight)		Progen, clone 517.67, 651169
Rabbit anti - F11r (Jam1)	[1:50]		ABclonal, A1241, Lot 0005180101
Rabbit anti - Fnbp1l (Toca-1)	[1:100]		Bethyl Laboratories, A303-469A, Lot 1
Rabbit anti - HA	[1:500]	[1:1000]	Cell Signaling, clone C29F4, 3724S
Rabbit anti - Ildr2	[1:250]		BiCell Scientific Inc, 00303
Rabbit anti - Ildr2	[1:50]		Lifespan BioSciences LS-C205504
Rabbit anti - Ildr2	[1:50]		Invitrogen, PA5-46481, Lot WE327570
Rabbit anti - Pard3	[1:250]		Sigma-Aldrich, 07-330, Lot 2615671
Rabbit anti - podocin	[1:500]	[1:1000]	Invitrogen, PA5-79757, Lot WL3458408
Rabbit anti - WT1	[1:500]		Abcam, ab89901, LotGR3365362-7
Lotus Lectin	[1:1000]		Vector Laboratories, FL-1321, Lot ZC0914
Streptavidin - APC	[1:1000]		BD Pharmingen, 554067 Lot 7040924
Streptavidin - HRP		[1:5000]	Cell Signaling, 3999S, Lot 8

199 **Supplemental Table I. List of antibodies with respective company identifiers and**
200 **concentrations for immunoflorecence (IF) and western blot (WB) analyses utilized in this**
201 **investigation.**

Supplemental Table II.

Gene Symbol	Majority Protein IDs	Protein Names	Razor + Unique Peptides	Log ₂ Fold Change	p - Value
<i>Nphs2</i>	Q91X05	Podocin	12	10.63	0.00003
<i>Tjp1</i>	P39447	Tight junction protein ZO-1	85	7.40	0.001
<i>Magi2</i>	Q9WWQ1	Membrane-associated guanylate kinase, WW and PDZ domain-containing protein 2	33	7.37	0.001
<i>Kirrel</i>	Q80W68	Kin of IRRE-like protein 1	20	7.06	0.001
<i>Pard3b</i>	Q9CSB4	Partitioning defective 3 homolog B	32	5.34	0.00002
<i>Ddn</i>	Q80TS7	Dendrin	12	5.33	0.00003
<i>Ildi2</i>	B5TVM2	Immunoglobulin-like domain-containing receptor 2	11	4.51	0.009
<i>Ctin</i>	Q60598	Src substrate cactin	15	4.01	0.0003
<i>Nebi</i>	Q9DC07	LIM zinc-binding domain-containing Nebulette	11	3.65	0.003
<i>Tjp2</i>	Q9Z0U1	Tight junction protein ZO-2	31	3.63	0.021
<i>S100g</i>	P97816	Protein S100-G	4	3.06	0.034
<i>Fnbp1l</i>	Q8K012	Fornin-binding protein 1-like	7	2.92	0.010
<i>Capza2</i>	P47754	F-actin-capping protein subunit alpha-2	8	2.82	0.014
<i>Alp6v1e1</i>	P50518	V-type proton ATPase subunit E 1	9	2.30	0.039
<i>Canx</i>	P35564	Cainexin	9	2.26	0.042
<i>Myzap</i>	Q3UIJ9	Myocardial zonula adherens protein	7	2.09	0.0001
<i>Kpnb1</i>	P70168	Importin subunit beta-1	2	1.96	0.041
<i>Dars</i>	Q922B2	Aspartate-tRNA ligase, cytoplasmic	7	1.88	0.029
<i>Cndp2</i>	Q9D1A2	Cytosolic non-specific dipeptidase	6	1.83	0.041
<i>Pls3</i>	Q99K51	Plastin-3	5	1.76	0.029
<i>Sult1d1</i>	Q3UZZ6	Sulfotransferase 1 family member D1	5	1.73	0.038
<i>Uqcr10</i>	Q8R111	Cytochrome b-c1 complex subunit 9	3	1.67	0.048
<i>Uba52</i>	P62984; P62983; P0CG49; P0CG50	Ubiquitin-60S ribosomal protein L40	5	1.60	0.041
<i>Sec23a</i>	Q01405	Protein transport protein Sec23A	7	1.59	0.030
<i>Cisd2</i>	Q9CQB5	CDGSH iron-sulfur domain-containing protein 2	2	1.46	0.026
<i>Naca</i>	Q60817; P70670	Nascent polypeptide-associated complex subunit alpha, muscle-specific form	2	1.46	0.049
<i>Ca15</i>	Q99N23	Carbonic anhydrase 15	3	1.44	0.050
<i>Qars</i>	Q8BML9	Glutaminyl-tRNA Synthetase 1	2	1.40	0.039
<i>Rpl35</i>	Q6ZWW7	60S ribosomal protein L35	4	1.37	0.038
<i>Agk</i>	Q9ESW4	Acylglycerol kinase, mitochondrial	5	1.37	0.039
<i>Scp2</i>	P32020	Non-specific lipid-transfer protein	13	1.36	0.026
<i>Aimp1</i>	P31230	Endothelial monocyte-activating polypeptide 2	2	1.26	0.046
<i>Dhrs7b</i>	Q9J4J7	Dehydrogenase/reductase SDR family member 7B	5	1.24	0.024
<i>Fabp4</i>	P04117	Fatty acid-binding protein, adipocyte	2	1.17	0.012
<i>Mpv17</i>	P19258	Protein Mpv17	2	1.15	0.007
<i>Sf3b1</i>	Q99NB9	Splicing factor 3B subunit 1	4	1.10	0.039
<i>Dkc1</i>	Q9ESX5	H/ACA ribonucleoprotein complex subunit 4	4	1.06	0.003
<i>Por</i>	P37040	NADPH-cytochrome P450 reductase	11	1.05	0.031
<i>Sympo</i>	Q8CC35	Synaptopodin	6	1.02	0.054
<i>Acox1</i>	Q9R0H0	Peroxisomal acyl-coenzyme A oxidase 1	24	1.01	0.015
<i>Cisd1</i>	Q91WS0	CDGSH iron-sulfur domain-containing protein 1	6	0.99	0.036

203 **Supplemental Table II. Proteomic profiling of cohort 1, 8-10 week old *Nphs2*^{BioID2} male mice,**
204 **identifies 41 significantly detected podocyte foot process proteins.** MS analysis of biotin
205 administered male *Nphs2*^{BioID2/+} mice identifies Podocin, Tjp, Magi, Kierrel, and Pard3 as top 5
206 proteins respectively. Table list 41 significant proteins ($p \leq 0.05$) at a Log₂ cut off 1.0 with their
207 respective p -values in the far-right column. Podocin was identified as the top hit and is
208 documented to oligomerize with itself adding confidence that the MS analysis was successful. All
209 proteins were identified with at least 2 razor unique peptide sequences *i.e.*, two peptide sequences
210 aligned only to that protein.

211
212
213
214
215
216
217
218
219
220
221
222
223
224
225
226
227

Supplemental Table III.

Gene Symbol	Majority Protein IDs	Protein Names	Razor + Unique Peptides	Log ₂ Fold Change	p - Value
<i>Kirrel</i>	Q80W68	Kin of IRRE-like protein 1+D3:D62	15	10.19	0.001
<i>Tjp1</i>	P39447	Tight junction protein ZO-1	85	9.88	0.003
<i>Part3b</i>	Q9CSB4	Partitioning defective 3 homolog B	26	9.62	0.016
<i>Ddn</i>	Q60TS7	Dendrin	11	8.99	0.005
<i>Magi2</i>	Q9WVQ1	Membrane-associated guanylate kinase, WW and PDZ domain-containing protein 2	24	8.61	0.011
<i>Nebi</i>	Q9DC07	LIM zinc-binding domain-containing Nebulette	7	7.75	0.021
<i>Ildi2</i>	B5TVM2	Immunoglobulin-like domain-containing receptor 2	9	7.42	0.010
<i>Ctin</i>	Q60598	Src substrate cactactin	14	7.08	0.020
<i>Nphs2</i>	Q91X05	Podocin	10	7.05	0.023
<i>Fnbp11</i>	Q8K012	Formin-binding protein 1-like	5	6.65	0.008
<i>Magi1</i>	Q6RHR9	Membrane-associated guanylate kinase, WW and PDZ domain-containing protein 1	6	5.89	0.002
<i>Tjp2</i>	Q9Z0U1	Tight junction protein ZO-2	30	5.78	0.006
<i>Myzap</i>	Q3UJ9	Myocardial zonula adherens protein	4	4.80	0.018
<i>Synpo</i>	Q8CC35	Synaptopodin	4	4.79	0.043
<i>Khsp</i>	Q3U0V1	Far upstream element-binding protein 2	5	4.69	0.014
<i>Mapre1</i>	Q61166	Microtubule-associated protein RP/EB family member 1	4	4.56	0.019
<i>Yes1</i>	Q04736	Tyrosine-protein kinase Yes	8	4.34	0.015
<i>Tmem65</i>	Q4VAE3	Transmembrane protein 65	4	4.25	0.030
<i>Cd2ap</i>	Q9JLQ0	CD2-associated protein	5	4.15	0.019
<i>Ap1g1</i>	P22892	AP-1 complex subunit gamma-1	6	3.85	0.018
<i>Ewsr1</i>	Q61545	RNA-binding protein EWS	2	3.83	0.038
<i>Oxsm</i>	Q9D404	3-oxoacyl-[acyl-carrier-protein] synthase, mitochondrial	4	3.77	0.033
<i>Erlin2</i>	Q6BF29	Erlin-2	6	3.44	0.008
<i>Epb4115</i>	Q8BGS1	Band 4.1-like protein 5	9	3.13	0.003
<i>Hsd3b4</i>	Q61767	3 beta-hydroxysteroid dehydrogenase type 4	9	2.99	0.028
<i>Dhkd1</i>	A2ATU0	Probable 2-oxoglutarate dehydrogenase E1 component DHKTD1, mitochondrial	7	2.93	0.017
<i>Taco1</i>	Q8K0Z7	Translational activator of cytochrome c oxidase 1	2	2.64	0.045
<i>Aif1l</i>	Q9EQX4	Allograft inflammatory factor 1-like	3	2.31	0.001
<i>Gstt2</i>	Q61133	Glutathione S-transferase theta-2	4	2.24	0.002
<i>Sorbs1</i>	Q62417	Sorbin and SH3 domain-containing protein 1	18	2.21	0.036
<i>Tns2</i>	Q8CGB6	Tensin-2	12	2.20	0.007
<i>Farp1</i>	F8VPU2	FERM, RhoGEF and pleckstrin domain-containing protein 1	7	2.13	0.040
<i>Tjp3</i>	Q8QXY1	Tight junction protein ZO-3	7	2.12	0.043
<i>Slc25a42</i>	Q8R0Y8	Mitochondrial coenzyme A transporter SLC25A42	9	1.98	0.021
<i>Mybbp1a</i>	Q7TPV4	Myb-binding protein 1A	13	1.92	0.037
<i>Acnatt1</i>	A2AKK5	Acyl-coenzyme A amino acid N-acyltransferase 1	4	1.81	0.046
<i>Epb4111</i>	Q9Z2H5	Band 4.1-like protein 1	8	1.79	0.023
<i>Col1a1</i>	P11087	Collagen alpha-1(I) chain	8	1.73	0.002
<i>Col4a2</i>	P08122	Collagen alpha-2(IV) chain;Canstatin	5	1.69	0.006
<i>Nomo1</i>	Q6GQT9	Nodal modulator 1	17	1.68	0.014
<i>Col1a2</i>	Q01149	Collagen alpha-2(I) chain	10	1.65	0.001
<i>Dao</i>	P18894	D-amino-acid oxidase	11	1.63	0.002
<i>Apc4</i>	P59999	Actin-related protein 2/3 complex subunit 4	2	1.62	0.007
<i>Uqcrcf</i>	P99028	Cytochrome b-c1 complex subunit 6, mitochondrial	2	1.61	0.019
<i>Atp5l</i>	Q9CPQ8	ATP synthase subunit g, mitochondrial	4	1.59	0.002
<i>Patj</i>	Q63ZW7	Pals1-associated tight junction protein / InaD-like protein	6	1.53	0.003
<i>Dhrs1</i>	Q9L04	Dehydrogenase/reductase SDR family member 1	8	1.53	0.0003
<i>Apmap</i>	Q9D7N9	Adipocyte plasma membrane-associated protein	14	1.52	0.003
<i>Lad1</i>	P57016	Ladnin-1	14	1.49	0.012
<i>Rtn4</i>	Q99P72	Reticulon-4	8	1.49	0.012
<i>F11r</i>	Q88792	Junctional adhesion molecule A	2	0.70	0.050

230 **Supplemental Table III. Proteomic profiling of cohort 2, 8-10 week old *Nphs2*^{BioID2} male mice,**
231 **identifies 50 significantly detected podocyte foot process proteins.** MS analysis of
232 *Nphs2*^{BioID2/+} biotin administered mice identifies Kirrel, Tjp, Pard3, Ddn, and Magi as the top 5
233 proteins detected respectively, with Podocin detected in the top 10. Table list 50 significant
234 proteins ($p \leq 0.05$) at a Log_2 cut off ≥ 1.49 with respective p -values in the far-right column. One
235 additional immunoglobulin domain containing protein, Junction adhesion molecule 1 (Jam1 / F11r)
236 was also identified within this MS analysis with a Log_2 fold change of 0.7, $p \leq 0.05$. All proteins
237 were detected with at least two razor unique peptide sequences to the specific protein identified.
238
239
240
241
242
243
244
245
246
247
248
249
250
251
252
253
254
255

Supplemental Table IV.

Gene Symbol	Majority Protein IDs	Protein Names	Razor + Unique Peptides	Log ₂ Fold Change	p - Value
<i>Kirrel</i>	Q80W68	Kin of IRRE-like protein 1	18	5.99	0.027
<i>Ctn</i>	Q60598	Src substrate cactin	14	5.70	0.034
<i>Tjp1</i>	P39447	Tight junction protein ZO-1	90	5.62	0.050
<i>Pard3b</i>	Q9CSB4	Partitioning defective 3 homolog B	38	4.21	0.050
<i>Nabl</i>	Q9DC07	LIM zinc-binding domain-containing Nebulette	7	3.41	0.051
<i>Fnbp1l</i>	Q8K012	Formin-binding protein 1-like	7	3.22	0.025
<i>Magi2</i>	Q9WVQ1	Membrane-associated guanylate kinase, WW and PDZ domain-containing protein 2	30	2.89	0.044
<i>Sympo</i>	Q6CC35	Synaptopodin	10	2.88	0.044
<i>Ildr2</i>	B5TVN2	Immunoglobulin-like domain-containing receptor 2	11	2.76	0.003
<i>Tjp2</i>	Q9Z0U1	Tight junction protein ZO-2	21	2.71	0.037
<i>Col1a2</i>	Q01149	Collagen alpha-2(I) chain	3	2.68	0.046
<i>Nphs2</i>	Q91X05	Podocin	13	2.42	0.035
<i>Col1a1</i>	P11087	Collagen alpha-1(I) chain	5	2.37	0.011
<i>Ddn</i>	Q80TS7	Dendrin	13	2.35	0.021
<i>Pkp4</i>	Q68FH0	Plakophilin-4	13	2.27	0.033
<i>Cd2ap</i>	Q9JLQ0	CD2-associated protein	3	2.20	0.034
<i>Rdx; Msn</i>	P26043; P26041	Radixin; Moesin	2	1.74	0.015
<i>Afdn</i>	Q9GZQ1	Afadin	2	1.70	0.030
<i>Hspe1</i>	Q64433	10 kDa heat shock protein, mitochondrial	4	1.66	0.036
<i>Aif1l</i>	Q9EQX4	Allograft inflammatory factor 1-like	5	1.42	0.027
<i>Hist1h4a</i>	P62806	Histone H4	9	1.36	0.014
<i>Tns2</i>	Q8CGB6	Tensin-2	3	1.30	0.038
<i>Khk</i>	P97328	Ketohexokinase	2	1.25	0.027
<i>Clic1</i>	Q9Z1Q5	Chloride intracellular channel protein 1	2	1.21	0.027
<i>Hist2h2bb</i>	Q8CGP2;Q8CGP1	Histone H2B type 1	6	1.04	0.049
<i>Acadl</i>	P51174	Long-chain specific acyl-CoA dehydrogenase, mitochondrial	7	1.01	0.025

257 **Supplemental Table IV. Proteomic profiling of cohort 3, 8-10 week old *Nphs2*^{BioID2} female**
258 **mice, identifies 28 significantly detected podocyte foot process proteins.** MS analysis of
259 biotin administered female *Nphs2*^{BioID2/+} mice identifies Kirrel, Ctnn, Tjp, Pard3b, and Nebl as the
260 top 5 proteins detected. Table list 28 significant proteins ($p \leq 0.05$) at a Log₂ cut off 1.0 with
261 respective p -values in the far-right column. Many documented podocytes SD proteins are
262 identified, *i.e.* Podocin, giving indication the podocin-BioID model is successful. All proteins were
263 detected with at least two razor unique peptide sequences to the specific protein identified.

264

265

266

267

268

269

270

271

272

Supplemental Table V.

Gene Symbol	Protein Names	p-Value	Log ₂ Fold Change
<i>Kirrel</i>	Kin of IRRE-like protein 1	0.0006	7.75
<i>Tjp1</i>	Tight junction protein ZO-1	0.002	7.63
<i>Nphs2</i>	Podocin	0.019	6.70
<i>Pard3b</i>	Partitioning defective 3 homolog B	0.008	6.39
<i>Magi2</i>	Membrane Associated Guanylate Kinase, WW And PDZ Domain Containing 2	0.018	6.29
<i>Cttn</i>	Src substrate cortactin	0.001	5.60
<i>Ddn</i>	Dendrin	0.003	5.56
<i>Nebi</i>	LIM zinc-binding domain-containing Nebulette	0.010	4.93
<i>Ildr2</i>	Immunoglobulin-like domain-containing receptor 2	0.007	4.90
<i>Fnbp1l</i>	Formin-binding protein 1-like	0.014	4.27
<i>Synpo</i>	Synaptopodin	0.047	2.90
<i>Tjp2</i>	Tight junction protein ZO-2	0.014	4.71
<i>Myzap</i>	Myocardial zonula adherens protein	0.009	3.45
<i>Cd2ap</i>	CD2-associated protein	0.020	3.18
<i>Col1a1</i>	Collagen alpha-1(I) chain	0.007	2.05
<i>Aif1l</i>	Allograft inflammatory factor 1-like	0.014	1.86
<i>Tns2</i>	Tensin-2	0.022	1.75
<i>Magi1</i>	Membrane Associated Guanylate Kinase, WW And PDZ Domain Containing 2	0.002	5.89
<i>Khsrp</i>	Far upstream element-binding protein 2	0.014	4.69
<i>Mapre1</i>	Microtubule-associated protein RP/EB family member 1	0.019	4.56
<i>Yes1</i>	Tyrosine-protein kinase Yes	0.015	4.34
<i>Tmem65</i>	Transmembrane protein 65	0.030	4.25
<i>Ap1g1</i>	AP-1 complex subunit gamma-1	0.018	3.85
<i>Erlin2</i>	Erlin-2	0.008	3.44
<i>Epb41f5</i>	Band 4.1-like protein 5	0.003	3.13
<i>S100g</i>	Protein S100-G	0.034	3.06
<i>Capza2</i>	F-actin-capping protein subunit alpha-2	0.014	2.82
<i>Atp6v1e1</i>	V-type proton ATPase subunit E 1	0.039	2.30
<i>Pkp4</i>	Plakophilin-4	0.033	2.27
<i>Canx</i>	Calnexin	0.042	2.26
<i>Sorbs1</i>	Sorbin and SH3 domain-containing protein 1	0.036	2.21
<i>Farp1</i>	FERM, RhoGEF and pleckstrin domain-containing protein 1	0.040	2.13
<i>Tjp3</i>	Tight junction protein ZO-3	0.043	2.12
<i>Mybbp1a</i>	Myb-binding protein 1A	0.037	1.92
<i>Cndp2</i>	Cytosolic non-specific dipeptidase	0.041	1.83
<i>Epb41f1</i>	Band 4.1-like protein 1	0.023	1.79
<i>Pls3</i>	Plastin-3	0.029	1.76
<i>Rdx</i>	Radixin	0.015	1.74
<i>Msn</i>	Moesin	0.015	1.74
<i>Afdn</i>	Afadin	0.021	1.70
<i>Col4a2</i>	Collagen alpha-2(IV) chain;Canstatin	0.006	1.69
<i>Nomo1</i>	Nodal modulator 1	0.014	1.68
<i>Col1a2</i>	Collagen alpha-2(I) chain	0.0009	1.65
<i>Arpc4</i>	Actin-related protein 2/3 complex subunit 4	0.007	1.62
<i>Sec23a</i>	Protein transport protein Sec23A	0.030	1.59
<i>Patj</i>	Pals 1-associated tight junction protein / InaD-like protein	0.003	1.53
<i>Lad1</i>	Ladinin-1	0.012	1.49
<i>Rtn4</i>	Reticulon-4	0.012	1.49
<i>Cisd2</i>	CDGSH iron-sulfur domain-containing protein 2	0.026	1.46
<i>Naca</i>	Nascent polypeptide-associated complex subunit alpha	0.049	1.46
<i>Scp2</i>	Non-specific lipid-transfer protein	0.026	1.36
<i>Aimp1</i>	Endothelial monocyte-activating polypeptide 2	0.046	1.26
<i>Dhrs7b</i>	Dehydrogenase/reductase SDR family member 7B	0.024	1.24
<i>Clic1</i>	Chloride intracellular channel protein 1	0.027	1.21

274 **Supplemental Table V. Compiled proteomic profile of three cohorts of, 8-10 week old male**
275 **and female, *Nphs2*^{BioID2} mice.** Table list 54 significant proteins ($p \leq 0.05$) at a Log_2 cut off ≥ 1.20 ,
276 with respective p -value listed in the far-right column. Table compiles the proteomic profiles across
277 all three separate analysis and averages their respective Log_2 fold change and p -values. This table
278 was subsequently utilized for *Qiagen Ingenuity Pathway Analysis* (IPA) and input into
279 the *Database for Annotation, Visualization, and Integrated Discovery* (DAVID) for gene ontogeny
280 characterization. All proteins were detected with at least 2 razor unique peptides specific to the
281 protein denoted.

282

283

284

285

286

287

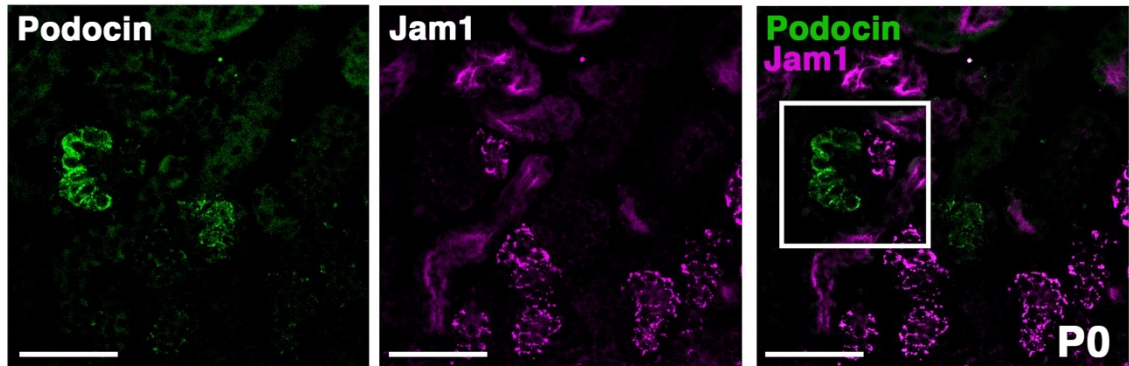
288

289

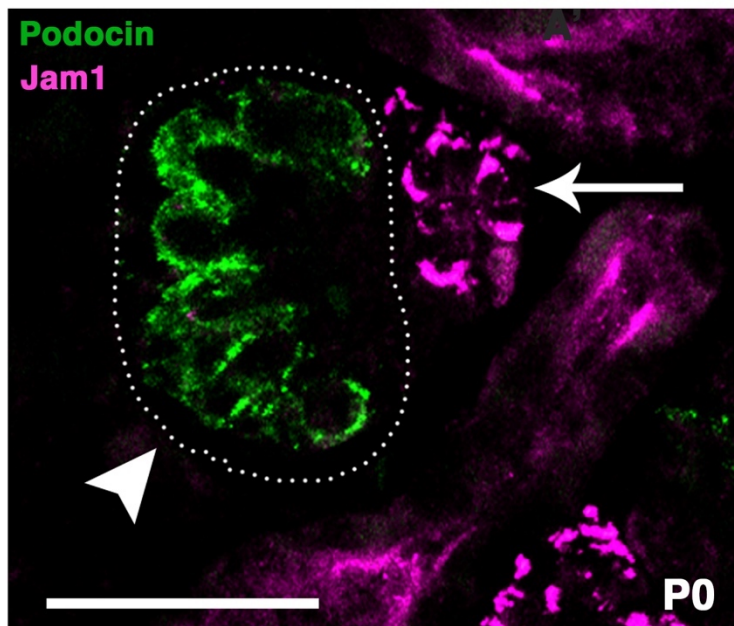
290

Supplemental Figure 1.

A



A'

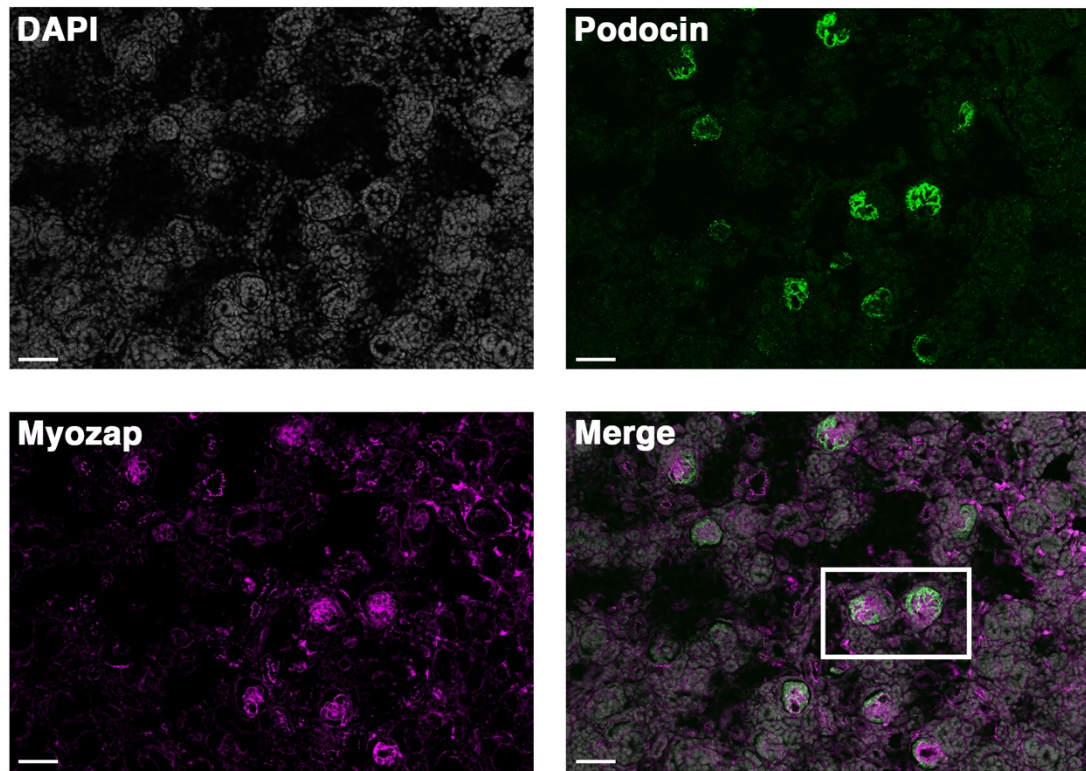


292 **Supplemental Figure 1. Expression of immunoglobulin superfamily member Jam1/F11r in**
293 **tubule cells neighboring podocytes. (A).** Jam1 was identified to have a 0.7 Log₂ fold change in
294 a single mass spec analysis. P0 kidney sections were immunostained for Jam1 (magenta) and
295 podocin (green). Jam1 is localized to tubule cells directly adjacent to podocytes. **(A')** Highlighted
296 white boxed region from **(A)** is enlarged to show podocin localization restricted to the glomerulus,
297 outlined in a dotted white circle, and Jam1 localization in neighboring tubule cells, denoted by white
298 arrow. All scale bars: 50 μm.

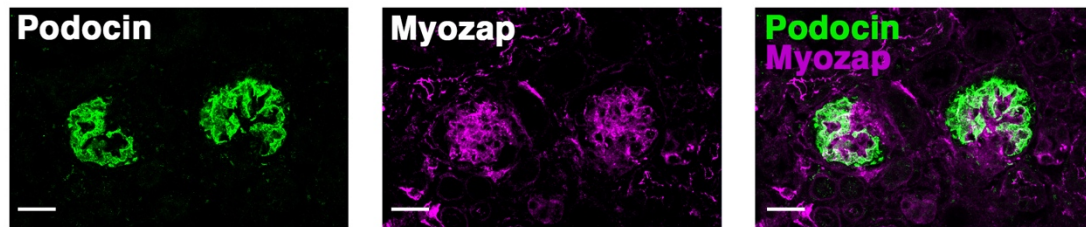
299
300
301
302
303
304
305
306
307
308
309
310
311
312
313
314
315
316
317
318
319
320
321
322

Supplemental Figure 2.

A



A'

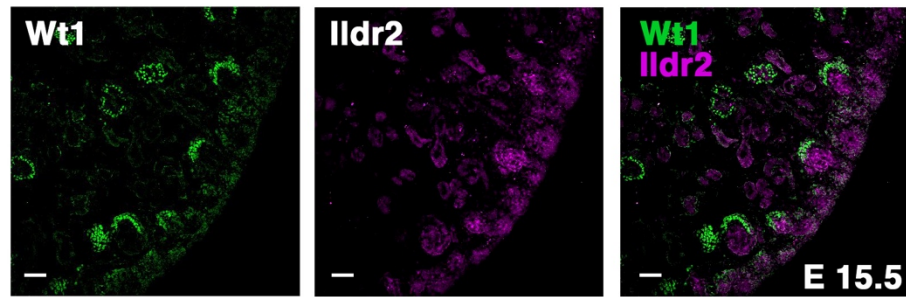


325 **Supplemental Figure 2. Myozap localizes to endothelium of glomeruli. (A)**
326 Immunofluorescence analysis of Myozap (magenta) identifies strong localization to the central
327 region of the glomerulus and endothelium outside the glomerulus. Proteomic profiling detected a
328 significant Myozap signal (3.45 Log₂ FC), in two of three MS analyses. We observe some overlap
329 (white) between Myozap (magenta) and podocin (green), while the majority of Myozap signal does
330 not overlap with podocin and instead localizes to presumptive endothelium cells. Scale bar: 50 μm
331 **(A')** Highlighted white boxed region from **(A)** indicating staining of Myozap within the endothelium
332 of the glomerulus and some overlap with podocin. Scale bar 20 μm.

333
334
335
336
337
338
339
340
341
342
343
344
345
346
347
348
349
350
351

Supplemental Figure 3.

A



353 **Supplemental Figure 3. Ildr2 is detected in early embryonic nephron precursors including**
354 **the renal vesicle, comma, and s-shaped bodies.** IF analysis of E15.5 animals detects Ildr2 in
355 both continuous membranous staining pattern and in punctate spots. In some S-shaped bodies,
356 denoted by Wt1 expression in developing podocytes (green), Ildr2 (magenta) is detected in a
357 continuous membranous pattern that appears to extend into the tubules, arrow. However, Ildr2
358 also appears punctate in other renal vesicles, comma, and s-shaped bodies, arrowheads.
359

360

361

362

363

364

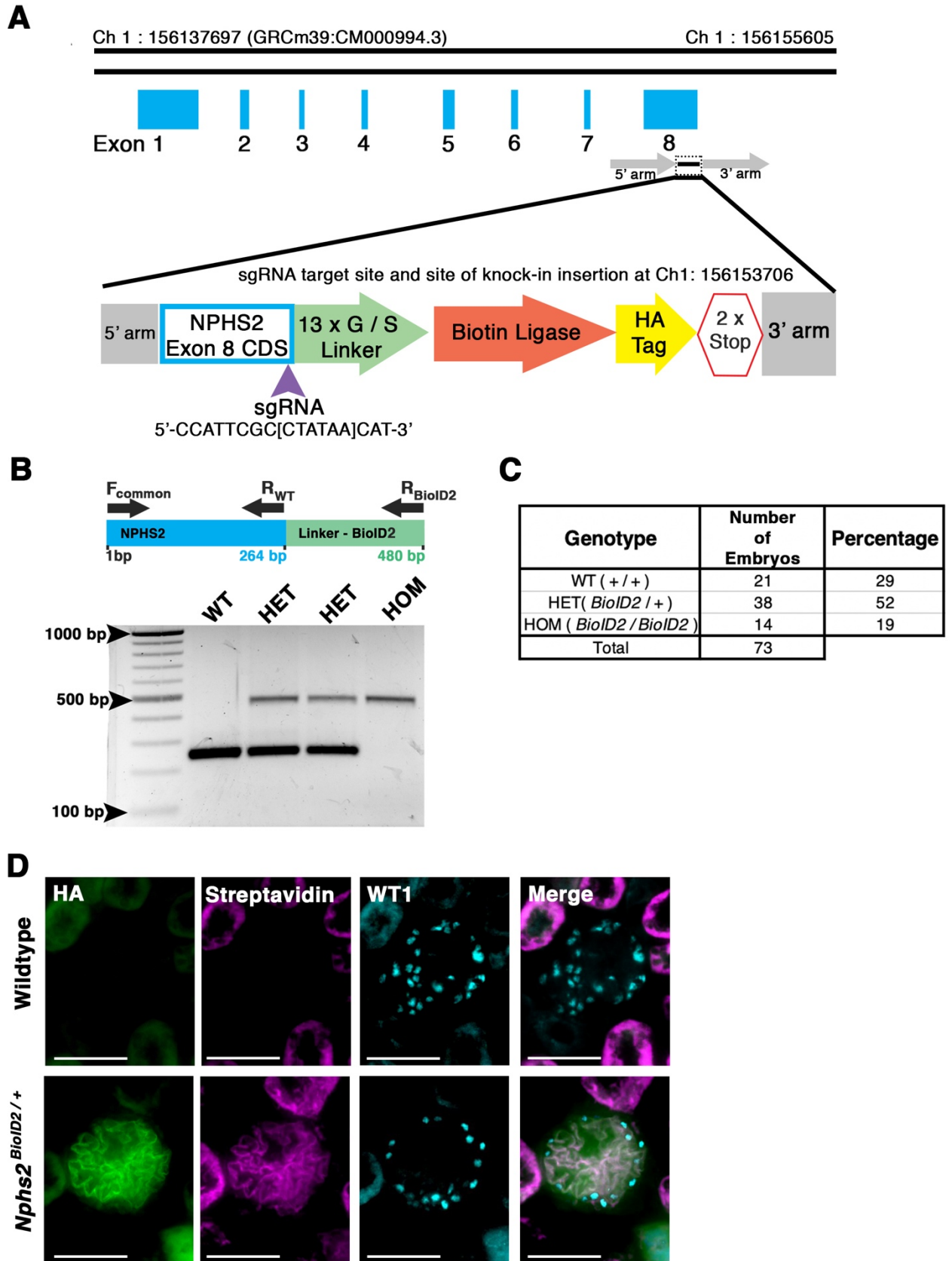
365

366

367

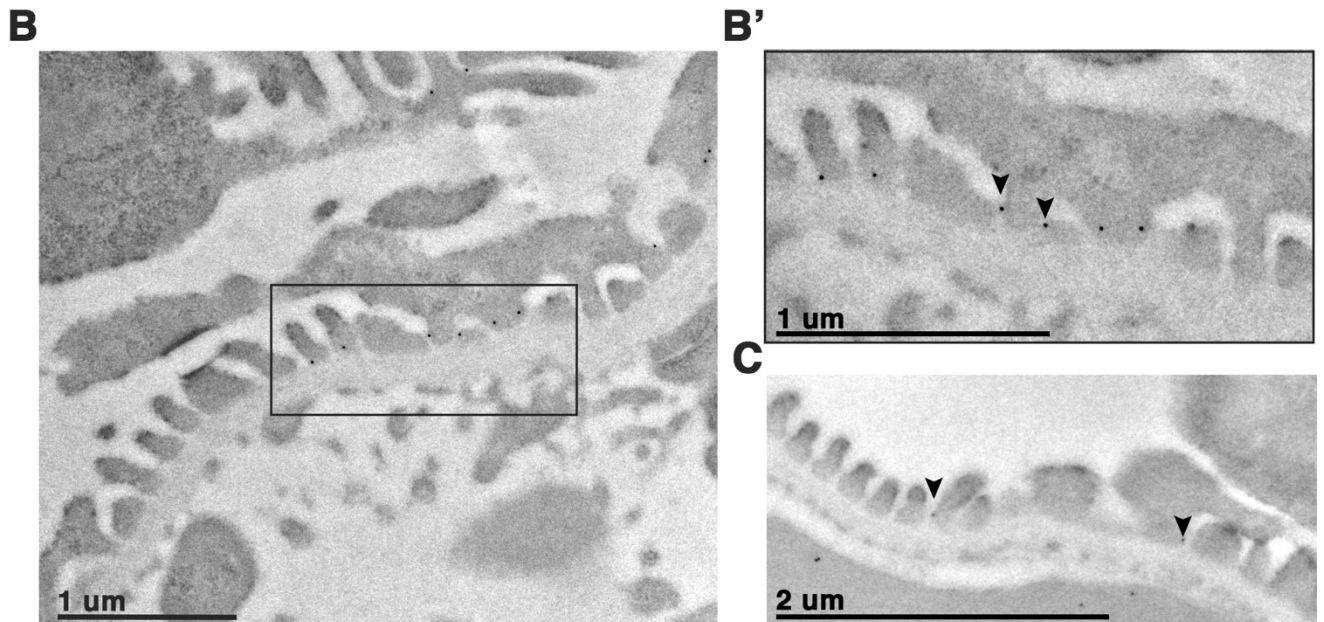
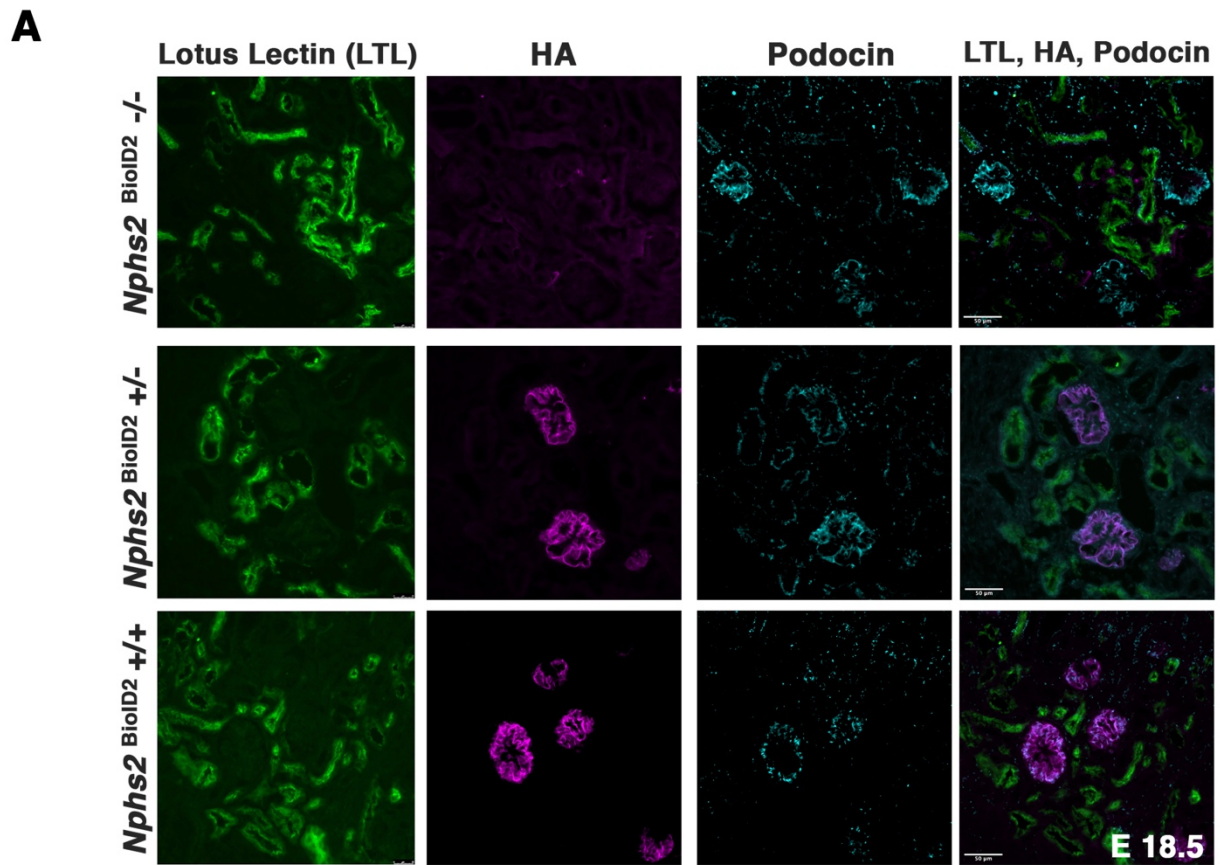
368

Figure 1



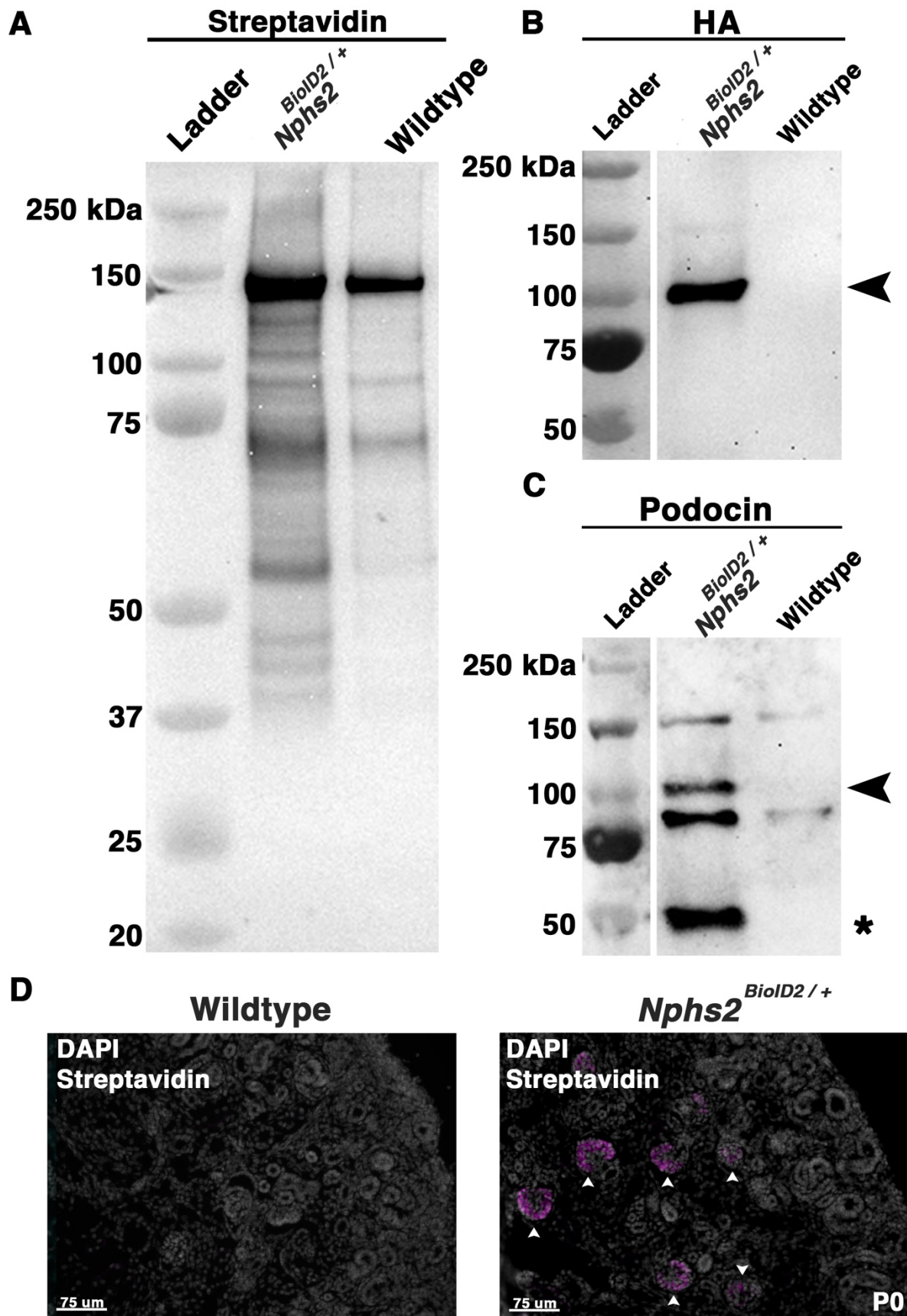
2 **Figure 1. Generation of a knock-in *Nphs2*^{BioID2} mouse line via CRISPR/Cas9 genome editing**
3 **of the *Nphs2* locus. (A)** Schematic of the CRISPR/Cas9 genome editing strategy utilized to
4 generate the *Nphs2*^{BioID2} mouse line. A small guide RNA (sgRNA) targeting the stop codon in exon
5 8 of *Nphs2* (purple arrowhead) was combined with a donor vector containing the knock-in cassette
6 (zoom view) to induce homologous recombination and integrate the BioID2 moiety containing a
7 13x Glycine/Serine (G/S) linker, biotin ligase, and HA tag into the *Nphs2* locus. **(B)** Genotyping
8 strategy (top panel) to identify genotype of mice as wildtype (single band at 264 base pairs (bp)),
9 heterozygous (two bands; one at wildtype size of 264 bp and a second that amplifies the BioID2
10 linker region giving a band at 480 bp), or homozygous (single band at the 480 bp). **(C)** Genotyping
11 of 73 embryos at E18.5-P0, verify an approximate Mendelian ratio of genotypes being recovered
12 (25:50:25). **(D)** IF analysis of 8–10-week-old adult mice injected with biotin illustrate an enrichment
13 of streptavidin detected within the glomerulus of *Nphs2*^{BioID2} mice and absence of streptavidin
14 signal in control age matched C57BL/6J littermate mice. The HA signal from the BioID2 moiety
15 closely overlaps with streptavidin, observed as white overlap in the merged image. Wilms Tumor
16 (WT1) is utilized as a podocyte marker to delineate the glomerular boundaries. Scale bar: 50 μ m
17
18

Figure 2.



20 **Figure 2. *Nphs2*^{BioID2} animals present normal kidney morphology with podocin-BioID**
21 **localized to podocytes and specifically the slit diaphragm. (A)** E18.5 littermates of wildtype,
22 heterozygous (*Nphs2*^{BioID2/+}), and homozygous (*Nphs2*^{BioID2/BioID2}) animals were analyzed for gross
23 kidney morphology and localization of podocin-BioID. The proximal tubule marker lotus lectin (LTL,
24 green) show normal tubule architecture without observation of nephron tubule dilation in
25 heterozygous (*Nphs2*^{BioID2/+}), and homozygous (*Nphs2*^{BioID2/BioID2}) animals. The HA tag (magenta)
26 which is part of the BioID2 moiety was observed to tightly overlap with podocin (cyan) specifically
27 in the glomerulus. The relative size and number of glomeruli was unchanged between control,
28 heterozygous, and homozygous animals. Further, the HA signal was not identified outside of the
29 glomeruli. Scale bar 50 μm **(B)** *Nphs2*^{BioID2/+} localizes to the podocyte slit diaphragm. Utilizing
30 transmission electron microscopy (TEM) and immunogold labeling of 4-week-old murine kidney
31 samples, we detect the anti-HA signal as punctate dots strung just above the GBM adjacent to the
32 podocyte foot process within electron dense regions where the slit diaphragm bridges neighboring
33 foot processes. **(B')** Magnified view of boxed region from panel (B) depicting podocyte foot
34 processes and the electron dense regions between them where the HA signal localizes as dark
35 spherical dots from immunogold labeling, denoted with arrowheads. Scale bar 1 μm **(C)** Wildtype
36 littermates were immunogold labeled for podocin and similarly display localization of podocin at
37 electron dense regions between podocyte foot processes, highlighted with arrowheads. Scale bar
38 2 μm.
39
40
41
42
43
44
45
46
47
48
49
50
51
52
53
54
55
56
57
58
59
60
61
62
63
64
65
66
67
68
69

Figure 3



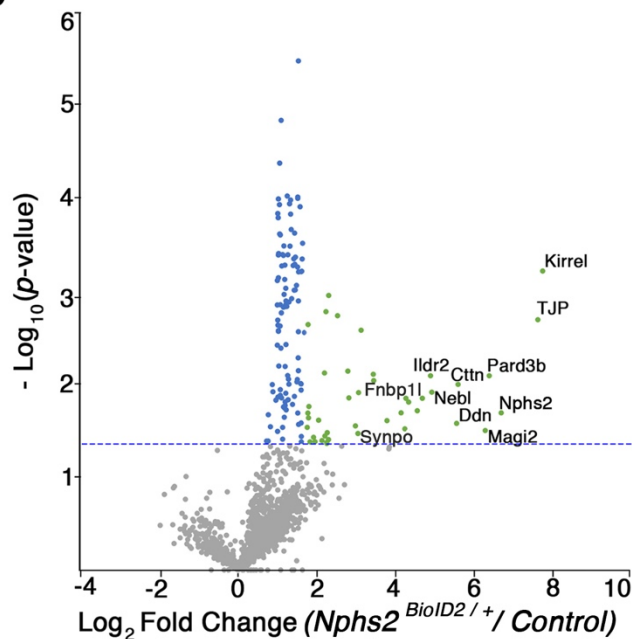
72 **Figure 3. Biotin administered *Nphs2^{BioID2/+}* mice present an enrichment of biotinylated**
73 **proteins specifically within glomeruli. (A)** A significant enrichment of streptavidin labeled,
74 biotinylated, proteins are observed across the entire molecular weight spectrum in *Nphs2^{BioID2/+}*
75 protein lysates compared to wildtype control littermates, injected with biotin. Streptavidin bead
76 purified lysates were subjected to protein separation and probed for streptavidin. Wildtype age
77 matched, 8–10-week-old, littermate controls present few streptavidin conjugated bands,
78 presumably endogenous metabolic carboxylases. However, *Nphs2^{BioID2/+}* lysates exhibit numerous
79 specific biotinylated protein bands across the entire molecular weight spectrum. **(B)** *Nphs2^{BioID2/+}*
80 lysates blotted with an anti-HA antibody present robust and specific detection of the HA signal only
81 within the *Nphs2^{BioID2/+}* sample, indicative of lysate purity. The HA signal is evident at approximately
82 100 kDa (arrowhead) in *Nphs2^{BioID2/+}* lysates. **(C)** *Nphs2^{BioID2/+}* samples probed for podocin show
83 two specific bands for both BioID2-tagged podocin and endogenous podocin. Adult 8-10-week-old
84 *Nphs2^{BioID2/+}* mice blotted for podocin present a 50kDa band for the endogenous unmodified
85 podocin protein, marked with an asterisk (*) and a second larger band at approximately 100 kDa
86 for the HA tagged podocin-BioID of *Nphs2^{BioID2/+}* mice (arrowhead). **(D)** P0 pups collected from
87 pregnant dams injected with 5 mg/kg of biotin every day from E11.5 to E18.5, and without injection
88 of newborn pups, manifest strong streptavidin detection within glomeruli. Immunofluorescence
89 analysis reveals an enrichment of streptavidin signal (magenta) specifically within the glomeruli
90 (arrowheads) of *Nphs2^{BioID2/+}* kidneys compared to wildtype. Scale bar 75 μm .
91
92
93
94
95
96
97
98
99
100
101
102
103
104

Figure 4.

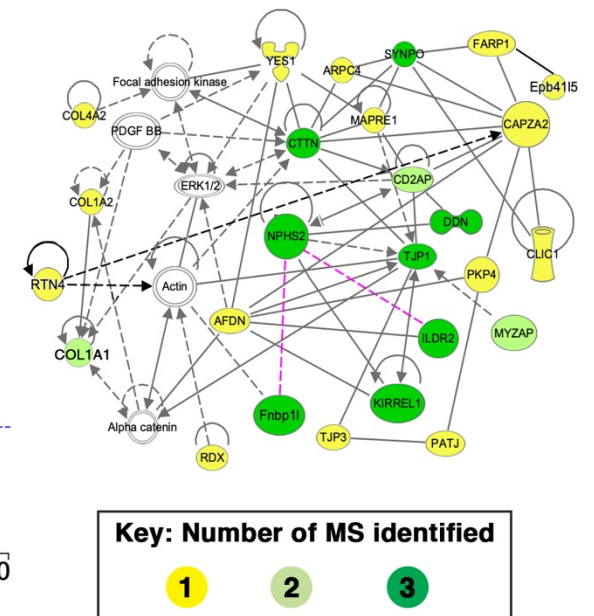
A

Gene Symbol	Protein Names	p-Value	Log ₂ Fold Change
<i>Kirrel</i>	Kin of IRRE-like protein 1	0.0006	7.75
<i>Tjp1</i>	Tight junction protein ZO-1	0.002	7.63
<i>Nphs2</i>	Podocin	0.019	6.70
<i>Pard3b</i>	Partitioning defective 3 homolog B	0.008	6.39
<i>Magi2</i>	Membrane-associated guanylate kinase, WW and PDZ domain-containing protein 2	0.018	6.29
<i>Cttn</i>	Src substrate cactinin	0.001	5.60
<i>Ddn</i>	Dendrin	0.003	5.56
<i>Nebi</i>	LIM zinc-binding domain-containing Nebulette	0.010	4.93
<i>Ildr2</i>	Immunoglobulin-like domain-containing receptor 2	0.007	4.90
<i>Fnbp1l</i>	Formin-binding protein 1-like	0.014	4.27
<i>Synpo</i>	Synaptopodin	0.047	2.90
<i>Tjp2</i>	Tight junction protein ZO-2	0.014	4.71
<i>Myzap</i>	Myocardial zonula adherens protein	0.009	3.45
<i>Cd2ap</i>	CD2-associated protein	0.020	3.18
<i>Col1a1</i>	Collagen alpha-1(I) chain	0.007	2.05
<i>Aif1l</i>	Allograft inflammatory factor 1-like	0.014	1.86
<i>Tns2</i>	Tensin-2	0.022	1.75

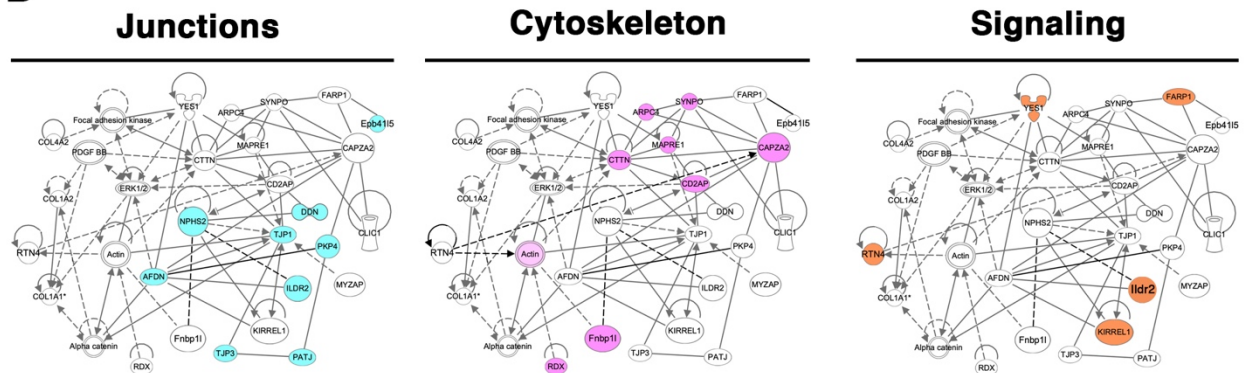
B



C



D



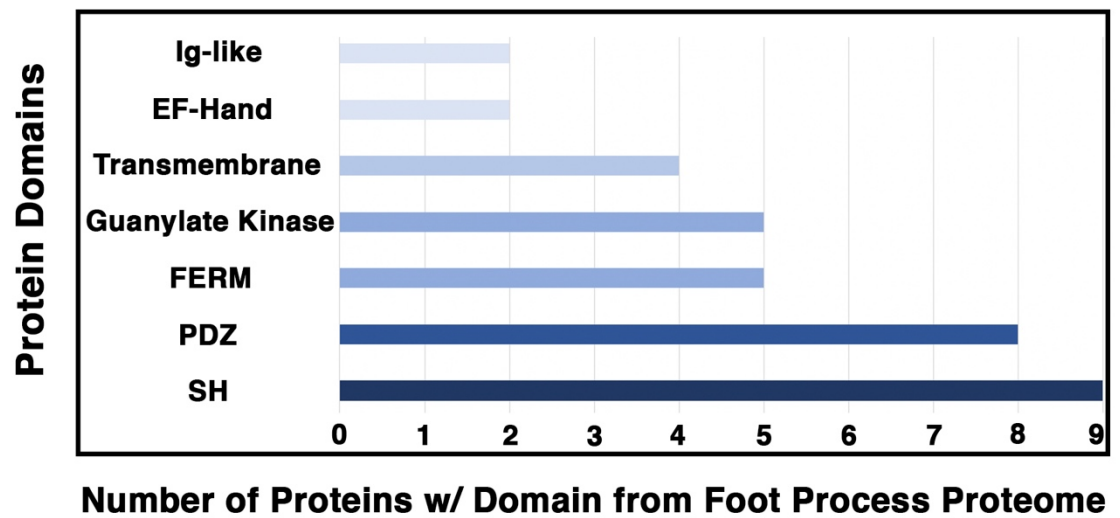
106 **Figure 4. Proteomics profiling of the podocyte foot process identifies documented slit**
107 **diaphragm components and novel candidates with unexplored podocyte function. (A)** Three
108 separate MS analyses were combined, and the average Log₂ fold change and respective *p*-values
109 were averaged to produce a list of the top foot process proteins. The top 11 proteins were
110 identified across all three MS profiles. Six additional proteins were identified across two of the
111 three MS analyses, denoted following the thick black bar. Podocin was a top protein identified and
112 known to oligomerize, indicating our MS proteomic profiling was effective. Additionally, many of the
113 top proteins uncovered, *i.e.*, Kirrel, Dnd, Tjp1/2, Magi2, Pard3, Synpo, and Cd2ap are documented
114 podocyte slit diaphragm components. **(B)** A volcano plot depicting approximately 1400 proteins
115 identified across all three MS analyses. Green dots represent the 40 proteins identified across
116 three separate MS profiles as having a Log₂ fold change ≥ 1.7 , and *p*-value ≤ 0.05 , blue dots
117 denote all proteins identified to have a significant *p*-value ≤ 0.05 , and grey dots are proteins with a
118 *p*-value ≥ 0.05 . The top 11 proteins consistently uncovered across all MS analyses are embedded
119 with gene symbols in the plot. The blue dotted line represents a *p*-value ≤ 0.05 . **(C)** Network
120 topology was generated utilizing *Qiagen Ingenuity Pathway Analysis* (IPA) on the top 54 proteins
121 from our cumulative proteomic profiles. IPA produces a proposed web of relationships from
122 published literature with most of our top proteins represented, (11 of 17), with documented
123 connections to other foot process and slit diaphragm components. The color intensities of each
124 protein (yellow to green) represent the number of MS analyses from which each protein was
125 identified. Darkest green shade=all three MS analyses, lighter green shade=two of three MS
126 analyses, and yellow=a single MS analysis. Dotted lines and unshaded proteins represent
127 predicted interactions / interactors from IPA analysis, respectively. Magenta lines are novel
128 proteins identified in this study to be present within the podocyte foot process. **(D)** Dissecting the
129 IPA network, identifies three central nodes representing junctions, cytoskeleton, and signaling.
130 Each respective node is color coded with junctions in cyan, cytoskeleton in magenta, and signaling
131 in orange. These computational network topologies and nodes tightly align with podocyte structure
132 and function.
133

Figure 5.

A

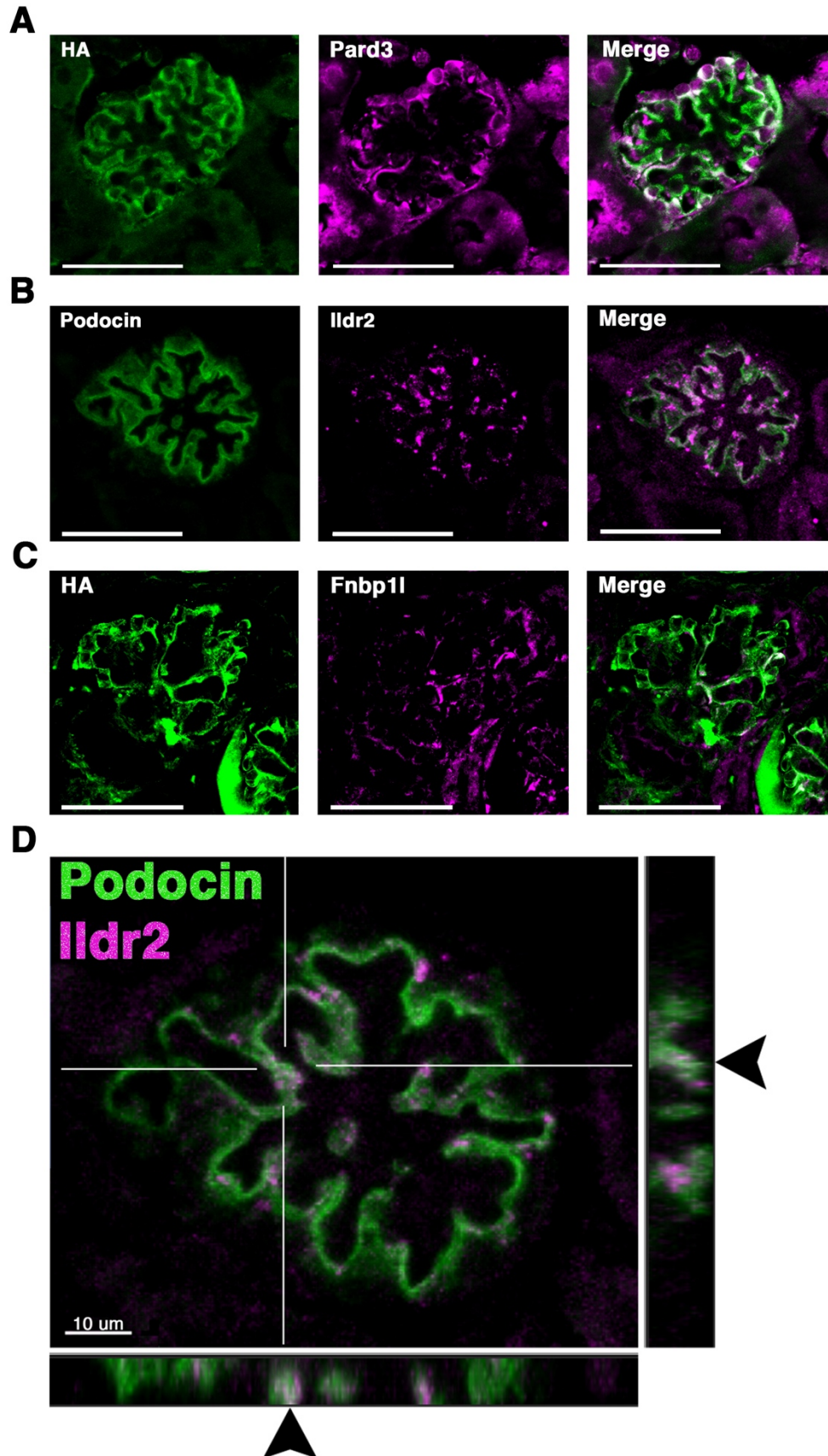
Gene Ontology (GO) Category	Cluster	Enrichment Score	Counts	p-Value
Molecular Function (MF)	Cytoskeletal Protein Binding	4.53	12	2.20×10^{-7}
	Actin Binding		6	7.80×10^{-5}
Cellular Component (CC)	Cell-Cell Junction	4.42	12	7.70×10^{-8}
	Adherens Junction		10	7.90×10^{-6}
Biological Process (BP)	Cytoskeleton Organization	2.61	14	3.20×10^{-7}
	Actin Filament-Based Process		12	8.70×10^{-8}

B



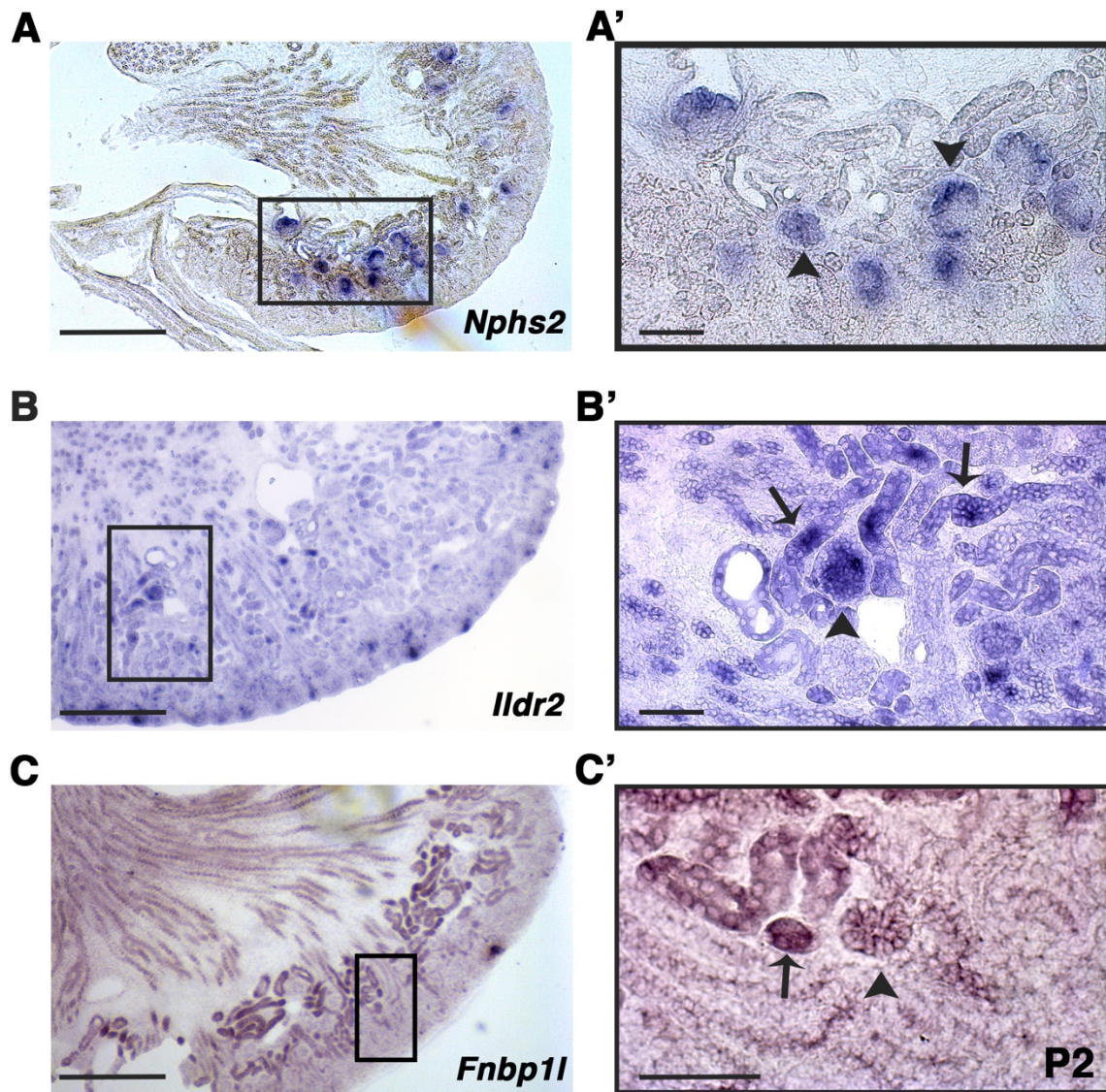
135 **Figure 5. Analysis of the podocyte foot process proteome identifies the cytoskeleton, cell-**
136 **cell junctions, and actin-based processes as the top GO categories with respective protein**
137 **domains that align with these functions.** The Database for Annotation, Visualization, and
138 Integrative Discovery (DAVID) was utilized for GO clustering analysis of the top 54 proteins
139 identified to have a Log_2 fold change ≥ 1.20 , and p -value ≤ 0.05 (Supplemental Table V). **(A)**
140 Overlap in GO readout was observed across the three separate GO categories analyzed,
141 molecular function, cellular component, and biological process, with cytoskeleton, actin, and
142 cellular junctions being the top hits. The respective top clusters within each GO category are listed,
143 alongside the relative enrichment score, number of proteins, and p -values. **(B)** Protein domain
144 analysis of the top 54 podocyte foot process proteins provides evidence for protein-protein
145 interactions and likely scaffold and protein-protein complex formation. Each protein's respective
146 protein domains were binary counted for presence or absence within the proteomics profile. The
147 top seven protein domains identified from the podocyte foot process proteome consist of a Src
148 homology (SH) ($n = 9$ proteins), PSD-95, Disc large, and ZO – 1 (PDZ) ($n = 8$), 4.1 protein, Ezrin,
149 Radixin and Moesin (FERM) ($n = 5$), Guanylate Kinase ($n = 5$), Transmembrane ($n = 4$), E and F
150 helix – Hand (EF – Hand) ($n = 2$), and an Immunoglobulin - like (Ig – like) domain ($n = 2$).
151 Cumulatively, these 7 domains represent $\sim 50\%$ of the top proteins identified from the foot process
152 proteome (26 / 54).

Figure 6.



154 **Figure 6. Two novel foot process candidates, Ildr2 and Fnbp1l, localize to podocytes and**
155 **overlap with podocin in the foot process.** IF analysis of three top candidates identified from the
156 proteomics profiling, Pard3, Ildr2, and Fnbp1l, were detected within glomeruli. **(A)** Pard3
157 (magenta), a known component of the podocyte foot process, co-localizes with HA signal of
158 podocin-BioID (green) producing a white signal in overlap. **(B)** Ildr2 (magenta) displays a punctate
159 localization pattern within the glomerulus and overlaps (white) with podocin (green). **(C)** Fnbp1l
160 (magenta) co-localizes (white) with HA signal of podocin-BioID (green) in podocytes. Scale bars in
161 A-C: 50 μm **(D)** A merged image of podocin and Ildr2 through a confocal z-projection identifies
162 punctate localization and overlap (white, arrowheads) between podocin (green) and Ildr2
163 (magenta) visualized in the z-plane in the left and bottom panels. Scale bar in D 10 μm .
164

Figure 7.



166 **Figure 7. *In situ* hybridization confirms glomerular and some tubule cell expression of *Ildr2***
167 **and *Fnbp1l* in P2 kidneys.** P2 kidney sections were hybridized with antisense riboprobes against
168 *Nphs2* (podocin), *Ildr2*, and *Fnbp1l*. **(A)** *Nphs2* (purple) displays strong expression specifically in
169 glomeruli at P2. The rectangular box in **(A)** is enlarged in **(A')** to highlight expression of *Nphs2* only
170 in glomeruli, arrowheads denote example glomeruli **(B)** *Ildr2* transcripts (purple) are identified
171 within glomeruli and tubules. The rectangular box in **(B)** is enlarged in **(B')** to denote expression of
172 *Ildr2* in glomeruli, arrowhead, and in some tubules, black arrow. **(C)** *Fnbp1l* (purple) is identified in
173 both glomeruli and tubules. The block rectangular box in **(C)** is enlarged in **(C')** to denote
174 expression of *Fnbp1l* in glomeruli, arrowhead, and tubules, arrow. Scale bars in A–C: 500 μ m.
175 Scale bars in A'–C': 100 μ m.

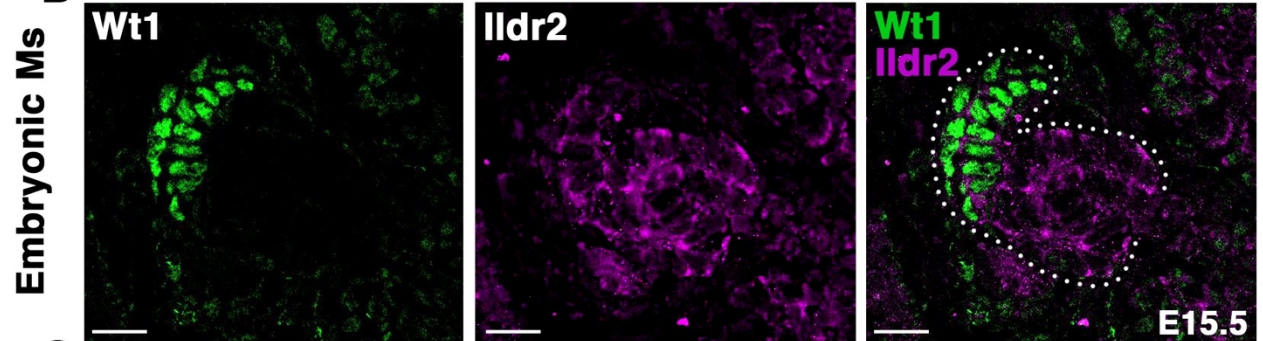
176
177
178
179
180
181

Figure 8.

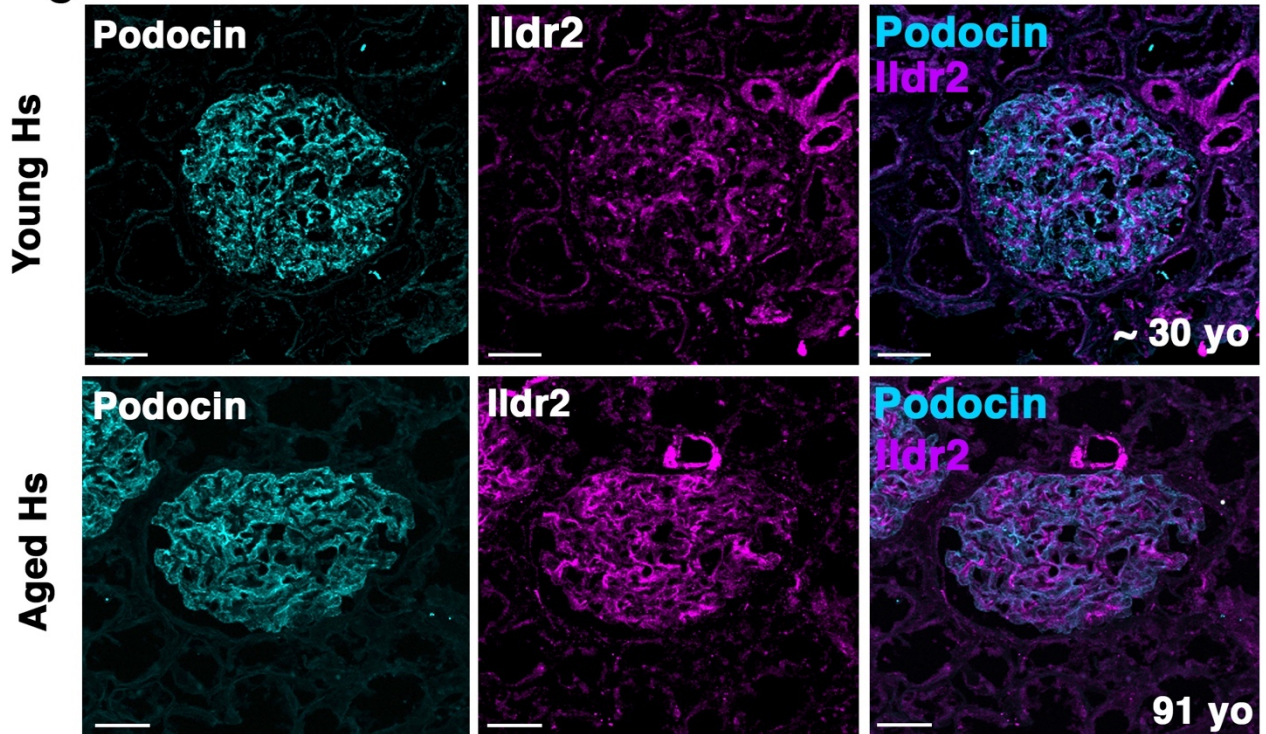
A

Gene Symbol	Protein Names	BioID (Young) vs WT Log ₂ Fold Change	BioID (Aged) vs WT Log ₂ Fold Change	p-Value
<i>Ildr2</i>	Immunoglobulin-like domain-containing receptor 2	2.76	3.53	0.001
<i>Tjp2</i>	Tight junction protein ZO-2	2.71	3.31	0.01
<i>Pkp4</i>	Plakophilin-4	2.27	2.94	0.01
<i>Nphs2</i>	Podocin	2.42	2.36	0.10
<i>Fnbp1l</i>	Formin-binding protein 1-like	3.22	2.12	0.10
<i>Tns2</i>	Tensin-2	1.30	0.36	0.10

B



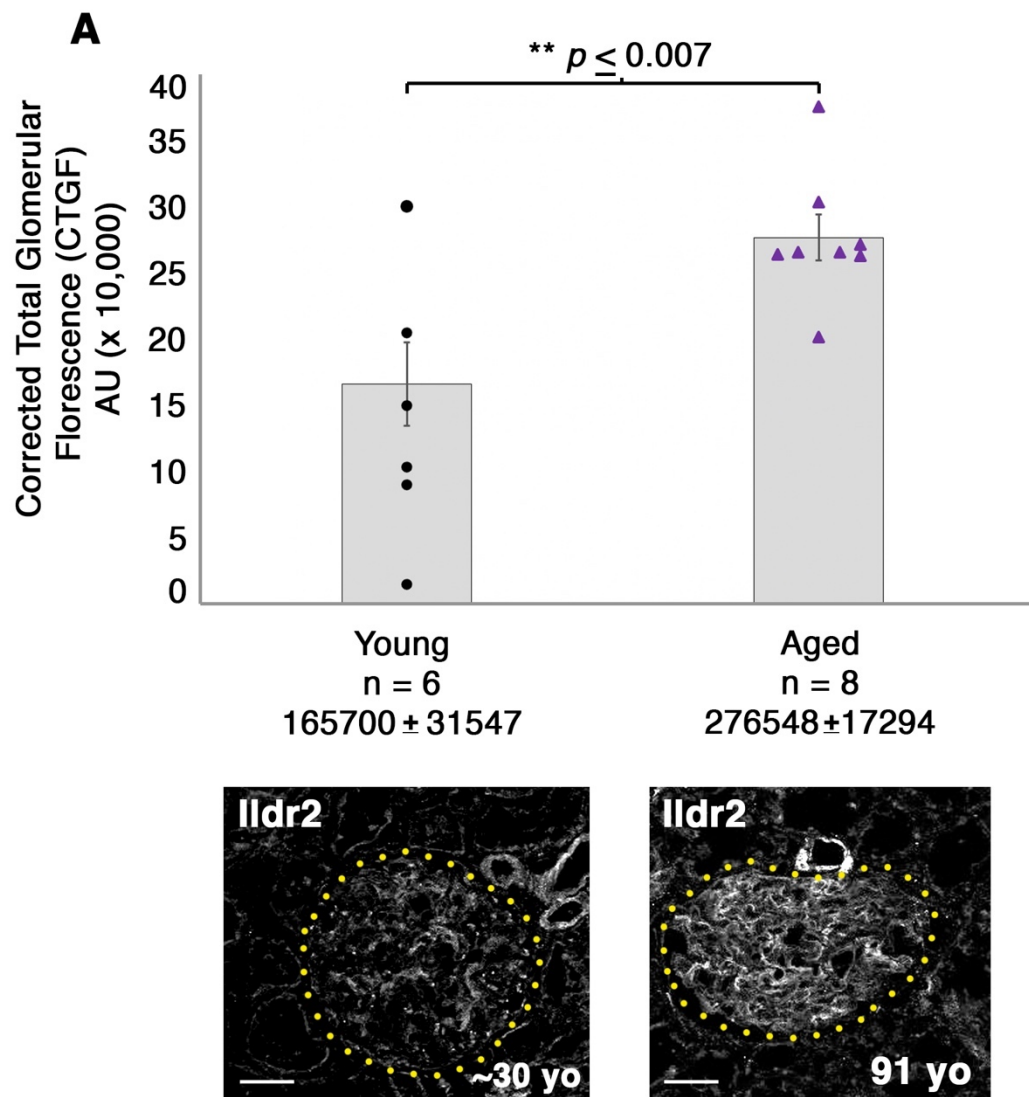
C



183 **Figure 8. Ildr2 is detected in developing nephron structures and presents increased**
184 **detection in aged mouse and human glomeruli compared to young. (A)** Proteomic profiling of
185 two aged (108 week old) male *Nphs2^{BioID2/+}* mice identifies a significant increase in Ildr2, Tjp2, and
186 Pkp4 protein levels compared to 8-10 week old *Nphs2^{BioID2/+}* mice. Table lists 6 proteins with
187 relative detection in “young” 8-10 week old *Nphs2^{BioID2/+}* male mice vs “aged” 108 week old
188 *Nphs2^{BioID2/+}* male mice. All proteins were detected with at least 2 razor unique peptides with their
189 respective *p*-values in far right column. **(B)** Ildr2 is expressed in early developing nephron
190 structures including the renal vesicle, comma, and s-shaped bodies with podocytes denoted by the
191 Wt1-positive nuclei. Ildr2 (magenta) is observed as membranous along the comma / s-shaped
192 body with some punctate foci in E15.5 mouse kidney cortex, outlined with white dots. Scale bar: 20
193 μm . **(C)** Young and aged (91 yo) human kidney tissue was probed of Ildr2 via IF. Young human
194 glomeruli display punctate foci detection of Ildr2 (magenta) similar to 8-10 week old mice.
195 However, aged (91 yo) male glomeruli evince an increase in Ildr2 detection within glomeruli.
196 Furthermore, where Ildr2 looks to be more highly detected in these aged glomeruli podocin
197 appears less detectable. Scale bar: 50 μm .

198
199
200
201
202
203
204
205
206
207
208

Figure 9



210 **Figure 9. Aged 91 yo glomeruli exhibit a significant increase in corrected total glomerular**
211 **florescence (CTGF) compared to young human glomeruli.** We observe a significant ($p \leq 0.007$)
212 increase, of approximately 67%, in CTFG in aged human Ildr2 detection compared to young human
213 tissue. CTGF was calculated by selecting the gomeruli as the ROI then measuring the total
214 florescence within the area and subtracting out the sum of the area by the average background
215 florescence, *i.e.* Total gROI florescence – (Area of glomerulus x mean of background florescence) =
216 CTGF. Two example glomeruli are displayed and outlined in yellow dots to depict the respective
217 ROI utilized to calculate CTGF. Scale bar: 50 μm .